2D SPIN-DEPENDENT ELECTRON SCATTERING BY NANOMAGNETS

By

Teshome Senbeta

SUBMITTED AS A
REQUIREMENT FOR THE DEGREE OF
DOCTOR OF PHILOSOPHY
AT
ADDIS ABABA UNIVERSITY
ADDIS ABABA
FEBRUARY 2012

ADDIS ABABA UNIVERSITY
DEPARTMENT OF
PHYSICS

The undersigned hereby certify that they have read and recommend to the School of Graduate Studies for acceptance a thesis entitled "**2D Spin-Dependent Electron Scattering by Nanomagnets**" by **Teshome Senbeta** as a requirement for the degree of **Doctor of Philosophy**.

Dated: February 2012

External Examiner: _____
Prof. Dr. Michael Farle

Research Supervisor: _____
Prof. V. N. Mal'nev

Internal examiner: _____
Prof. P. Singh

_____

ADDIS ABABA UNIVERSITY

Date: **February 2012**

Author: **Teshome Senbeta**

Title: **2D Spin-Dependent Electron Scattering by Nanomagnets**

Department: **Physics**

Degree: **Ph.D.** Convocation: **June** Year: **2012**

Permission is herewith granted to Addis Ababa University to circulate and to have copied for non-commercial purposes, at its discretion, the above title upon the request of individuals or institutions.

Signature of Author

To My Family.

Table of Contents

List of Tables

List of Figures

Abstract

The 2D scattering problem of an electron by a magnetized nanoparticle is solved in the Born approximation with account of the dipole - dipole interaction of the magnetic moments of electron and nanomagnet. The scattering amplitudes in this problem are the two-component spinors. They are obtained as functions of the electron spin orientation, the electron energy and show anisotropy in scattering angle. The initially polarized beam of electrons scattered by nanomagnet consists of electrons with no spin flipped and spin flipped. The majority of electrons with no spin flipped are scattered by small angles. This can be used as one method of controlling spin currents.

2D spin-dependent scattering of slow unpolarized beams of electrons by charged nanomagnets is analyzed in the Born approximation. The obtained scattering lengths are larger than those from the neutral nanomagnets approximately by one order. It is shown that for particular parameters of the system it is possible to polarize completely the scattered electrons in a narrow range of scattering angles. The most suitable system for realization of these effects is 2D Si electron gas with immersed nanomagnets.

The 2D spin-dependent electron scattering by the linear chain of periodic nanomagnets with account of the diffraction effects was studied. This effect takes place in 2D electron gas with immersed nanomagnets. By tuning a distance between nanomagnets, it is possible to obtain diffraction maximum of the scattered electrons at scattering angle, which corresponds to complete spin polarization of electrons. The total diffraction scattering lengths are proportional to N^2 (N is a number of nanomagnets). The proposed system can be an efficient separator of spin polarized currents.

Acknowledgements

First of all I would like to thank God. Next to this my grateful thanks go to Professor V. N. Mal'nev, my supervisor, for his kindly advise, many suggestions and constant support during this research. I am also thankful to the former department of physics education and department of physics for the sponsorship they provide me. I would also express my appreciation and thanks the office of Vice president for research and graduate program for financial support it provides me during my study as well as allow me to participate international conference.

The supports I got from my friends who are in land and abroad are not easily expressible. I give credit for them. Regarding to this my heart full thanks goes to Mr. Deresse Daba and Fikadu Beyen who are supporting me by buying different books from abroad and Dr. Tilaye Tadesse who sent me about three fourth of the journals I used in this research.

Finally, of course, I am grateful to my parents; my wife Asnakech Getu and my daughters Hawi Teshome and Hanna Teshome, for their patience and *love*. Without them this work would never have come into existence (literally).

Teshome Senbeta
February, 2012

Introduction

0.1 Background of spintronics

In 1936, Mott [1] laid a base to understand spin-polarized current. In his work he provided an explanation for an unusual behavior of resistance in ferromagnetic metals. He realized that at sufficiently low temperatures, where magnon scattering becomes vanishingly small, electrons of majority and minority spin, with magnetic moment parallel and antiparallel to the magnetization of a ferromagnet, respectively, do not mix in the scattering processes.

The first experimental demonstration of two current conduction at low temperatures in a ferromagnetic metal was provided in 1967 by I. A. Campbell and coworkers [2]. The main finding of this work is that detail measurements over a range of relative concentration for alloys containing two impurities simultaneously give actual values of the resistivity ratio $\rho_\uparrow/\rho_\downarrow$, which in turn give information on the electronic structure of the alloys.

In ferromagnetic metals like Fe, Ni, Co and their alloys both $4s$ and $3d$ electron bands contribute to the density of states at the Fermi level E_F. The Fermi level cuts across more than one band. As sketched in Fig. 1(b), the Fermi surface intersects a free-electron 4s band. However, it also intersects a 3d band which is not a simple parabola. In a ferromagnetic metal, the 3d up- and down-spin subbands are shifted

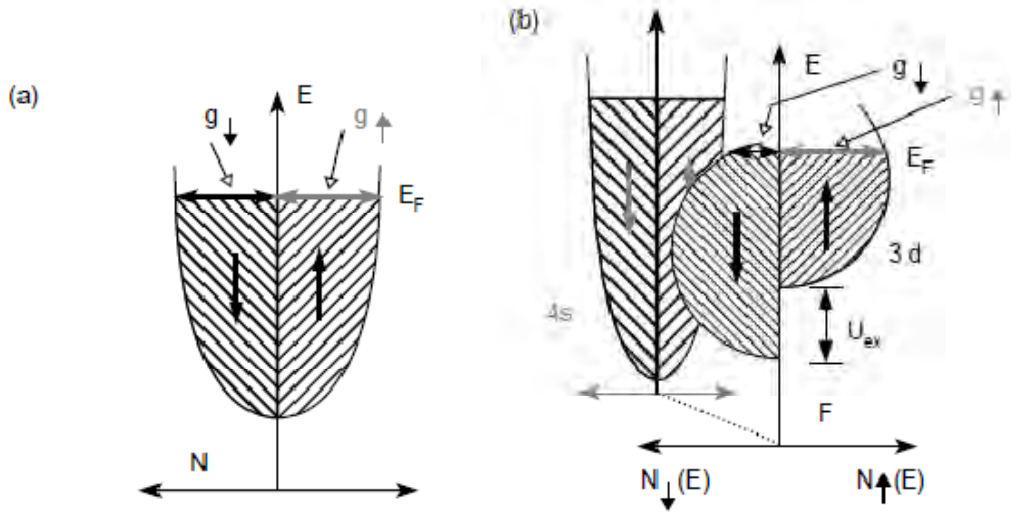

Figure 1: Energy bands of metals, density of states $N(E)$ as a function of energy E. (a) Nonmagnetic metals have a free-electron, parabolic density of states, which is partially filled. (b) In a transition metal ferromagnet, the $4s$ and $3d$ bands are intersected by E_F. The $3d$ band is exchange shifted by energy U_{ex} (Adopted from [3]).

out of symmetry. Figure 1(b) represents a band model of ferromagnetism, and the shift is called an exchange splitting, U_{ex} [3]. In a ferromagnetic material, the ion cores in the lattice have a net, nonzero spin. These magnetic ions can interact with each other when their charge distributions overlap, and this effect is called the exchange interaction. The number of down-spin conduction electrons differs from the number of up-spins, and this difference gives the spontaneous magnetization of the material. These result in shifting of energy band in the spin up and spin down $3d$ bands. This band splitting creates the imbalance between numbers $n_\uparrow$ and $n_\downarrow$ of $3d$ electrons that results in ferromagnetic moment $\mu \approx -(n_\uparrow - n_\downarrow)\mu_B/atom$ (μ_B is the Bohr magneton) [4]. The conduction process for such case is dominated by the $4s$ band as it has much higher mobility. Experiments show that at low temperature spin up and spin down

carry current in parallel [5]. This is a base of Giant magnetoresistance.

In 1971, D'yakonov and Perel [6] showed that possibility of orienting electron spin with current. When currents flow through a conductor, the multiple scattering of the carriers should give rise to a spin flux perpendicular to the current and directed from the interior to the periphery of the conductor. This leads to accumulation of spin orientation at the surface of the sample, limited by the spin relaxation. As a result there should exist at the surface of a current-carrying sample a layer in which the electrons spin are oriented (spin-layer). The spin layer thickness is determined by the length of spin diffusion.

Important length scales can be discussed in diffusive transport model. The spin-dependent scattering probability results in very different mean free path (the length for which the spin of an electron conserved) $l_\uparrow$ and $l_\downarrow$, or equivalently relaxation time (the time needed for an electron of velocity v_F to travel the mean free path l) $\tau_\uparrow$ and $\tau_\downarrow$.

As pointed in [7] and references therein, in ferromagnet/insulator/superconductor (F/I/S) junctions has proved that the tunneling current remains spin polarized even outside of the ferromagnetic region. In 1975 Julliè r [8] formulated a model for a change of conductance between the parallel ($\uparrow\uparrow$) and antiparallel ($\uparrow\downarrow$) magnetization in two different ferromagnetic regions. The corresponding tunneling magnetoresistance (TMR) in ferromagnet/insulator/ferromagnet (F/I/F) magnetic tunneling junction (M/T/J) is defined as

$$TMR = \frac{\triangle R}{R_{\uparrow\uparrow}} = \frac{R_{\uparrow\downarrow} - R_{\uparrow\uparrow}}{R_{\uparrow\uparrow}}, \tag{0.1.1}$$

where resistance R is given by the relative orientations of the magnetization in ferromagnet F_1 and F_2. The first ferromagnetic electrode acts as spin filter and the

second ferromagnetic layer acts as spin detector. The insulator that separated the two ferromagnets used as tunneling barrier (see Fig.2).

Figure 2 depicts the magnetic tunneling junction. The parallel configuration has low resistance than the antiparallel case. The magnetic tunneling junctions are the basis of Magnetic Random Access Memory (MRAM). It combines two concepts: short access time of semiconductor based on RAM and the non-volatile property of magnetic memories [9].

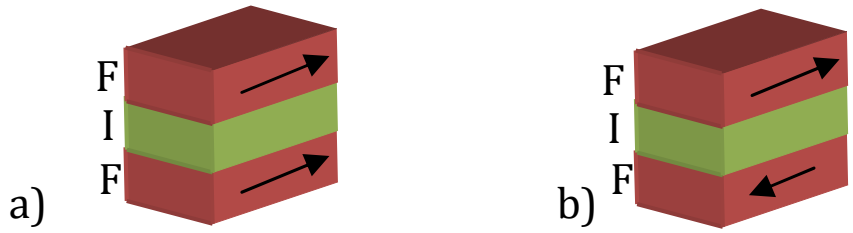

Figure 2: Schematic representation of the magnetic tunneling junction in ferromagnet/insulator/ferromagnet(F/I/F)(a) parallel and (b) antiparallel orientation of magnetizations. The current is perpendicular to the top surface of the ferromagnet.

Magnetoresistive random access memory (MRAM) is potentially an ideal memory because it has the properties of nonvolatility, high speed, unlimited write endurance, and low cost. These memories use the hysteresis of magnetic materials for storing data and some form of magnetoresistance for reading the data out. Because of the difficulty of separately connecting a large array of memory cells with complex integrated support circuits, the memory cells and support circuits are connected together on-chip [3].

The fundamental properties of spintronics are closely related to the length scale L

characteristic of samples and to the motion of electrons in metals. There are several length scales that characterize the properties of electrons in metals.

The z-component of spin s_z takes one of two values $\pm 1/2$ and is not necessarily conserved, that is, it is time dependent due to such effects as the spin-orbit interaction (SOI) and interactions between electrons. Therefore, the length for which the spin of an electron is conserved is finite. This length is called the spin-flip mean free path l and typically takes values in the range 10^2 nm to 10 μm [10].

Due to scattering of electrons, the length an electron travels with a fixed spin direction is much shorter than the spin-flip mean free path. This length is called the spin-diffusion length λ_{spin}. To find the spin-polarized current in non-magnetic metals it is necessary that the system length L be much shorter than λ_{spin}. In ferromagnetic metals, due to the imbalance between the number of electrons with up and down spins, the current may be spin polarized. Because the electrical resistivity is governed by the mean free path l, characterizes the scattering process of electrons, it is necessary that $l \ll \lambda_{spin}$, in order that the spin polarization of the current be meaningful. When this condition is satisfied, the spin polarization of the current is well defined and the up- and down-spin electrons may be treated independently. This is called Mott's two-current model [1]. When the $l \ll \lambda_{spin}$ is satisfied, the two-current model holds even in systems for which $L << \lambda_{spin}$.

Another important length scale is the Fermi wave length λ_F, which characterizes the electronic states. In general, $l >> \lambda_F$. This length scale becomes important when interference occurs between wave functions of electrons. The velocity of electrons on the Fermi surface is given by the Fermi velocity v_F and hence the time scale for an electron with v_F travelling a distance l is given by $\tau = l/v_F$ and called the relaxation

time.

Progress in nanofabrication techniques has made it possible to create artificial structures such as magnetic multilayers and nanocontacts, the characteristic scale length L of which can be shorter than λ_{spin} or l and can even be close to λ_F. In these cases, novel transport phenomena occur; giant magnetoresistance (GMR), tunnel magnetoresistance (TMR) and ballistic magnetoresistance (BMR) are typical examples. GMR occurs when the layer thickness of magnetic multilayers is close to or shorter than l. BMR occurs when the scale of the contact region of two ferromagnets is close to λ_F. TMR is a phenomenon in which the overlap of wave functions of electrons in two separated ferromagnetic metals becomes small.

0.2 Gigantic magnetoresistance

Magnetoresistance (MR) is the change in the electric conductivity of the material in the presence of magnetic field. The MR of metallic, semiconductor and insulator are different. The metallic conductance of ferromagnetic materials depend on the orientation of magnetization (the angle between electric current and the magnetization). This kind of magnetoresistance is known as anisotropic magnetoresistance (AMR). The ratio of MR when the current is perpendicular to magnetization direction to that of parallel is rather small. Researchers continued to increase this ratio and succeeded in the discovery of giant magnetoresistance (GMR)[11-12].

The discovery of GMR is considered as the starting point of the spin based electronics (spintronics). GMR is the change in electrical resistance in response to applied magnetic field. GMR is a quantum mechanical effect observed in layered magnetic

thin-film structures of the order of the nanometer size that are composed of alternating layers of ferromagnetic and nonmagnetic layers. The two main concept observed from GMR experiment are interlayer coupling and spin dependent scattering.

Before the discovery of GMR, it was hard to think a multilayered structure with anti-parallel magnetizations, that is, giant anti-ferromagnet. To observe giant anti-ferromagnetic, one needs very high magnetic fields to change an intrinsic anti-ferromagnetic spin structure into ferromagnetic. But, in the case of multilayers, the anti-parallel structure (giant anti-ferromagnet) generated by interlayer coupling can be turned into parallel structure (ferromagnetically saturated structure). This is the key concept behind the discovery of GMR, which seems to be the first successful experiment to utilize spin structure manipulation [10].

The main difference between GMR and AMR is that the former is due to the change in the internal magnetic structure while the later is due to the directional change in the total magnetization.

The discovery of GMR effect in Fe/Cr multilayers ignited different experimental groups to study the property of interlayer coupling in many other metals aiming to explore the nature of the MR effect in other elements. The results of these experiments show the existence of interlayer coupling in non-magnetic metals. It is interpreted as the iterlayer coupling is not originate from the intrinsic magnetic properties of the spacer layer.

When the magnetic moments of the ferromagnetic layers are parallel, the spin-dependent scattering of the carriers is minimized. This is to mean that the electrons are not scattered by the first layer will not scattered by the second layer and results in a low total resistance (large current). When the ferromagnetic layers are antiparallel, the

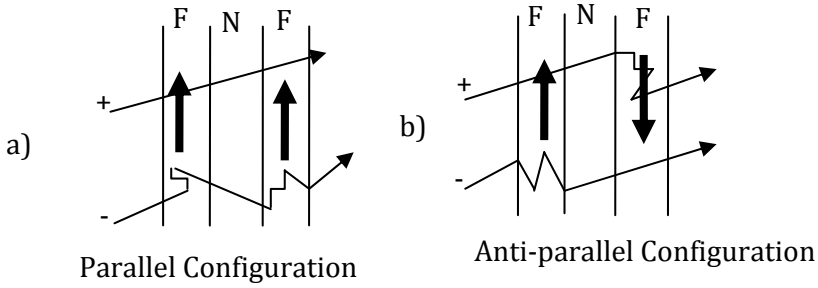

Figure 3: Schematic representation of the GMR mechanism. The electron trajectories are represented by straight lines and the scattering by abrupt changes in direction. The signs + and − are for spins $s_z = 1/2$ and $-1/2$ (majority and minority spin states, identical to ↑ and ↓ of uniform magnetic materials), respectively. The arrow represents majority spin direction in the magnetic layer. F denotes ferromagnetic material and N denotes nonmagnetic material.

spin-dependent scattering of the carriers increased. In this case each spin polarization will scatter by the sam amount and the total resistance of the material has maximum resistance (small current). The directions of the magnetic moments are manipulated by external magnetic fields that are applied to the materials. These materials can now be fabricated to produce significant changes in resistance in response to relatively small magnetic fields and to operate at room temperature. These phenomena are illustrated in Fig. 3.

The equivalent resistances diagram for Fig. 3(a) and (b) are given in Fig. 4(a) and (b), respectively. One can write the equivalent resistances for the two circuit diagram given in Fig. 4 as follow

$$R_P = 2\frac{R_\uparrow R_\downarrow}{R_\uparrow + R_\downarrow}, \tag{0.2.1}$$

$$R_{AP} = \frac{R_\uparrow + R_\downarrow}{2}, \tag{0.2.2}$$

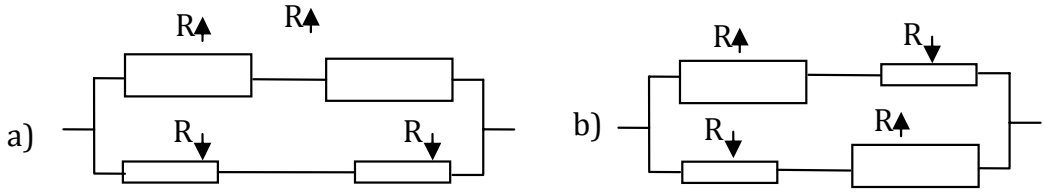

Figure 4: Equivalent circuit diagram for the scattering processes of electrons shown in Fig. 3. (a) Equivalent resistance diagram corresponding to Fig. 3(a). (b) Equivalent resistance diagram corresponding to Fig. 3(b).

where R_P is the total resistance after scattering process for parallel configuration, R_{AP} is the total resistance after scattering process for anti-parallel configuration, $R_\uparrow$ is the resistance of electrons with spin up and $R_\downarrow$ is the resistance of electrons with spin down. The relative magnetoresistance ratio is defined as

$$\Delta R/R = (R_{AP} - R_P)/R_{AP} = \frac{\left(R_\uparrow - R_\downarrow\right)^2}{\left(R_\uparrow + R_\downarrow\right)^2}. \tag{0.2.3}$$

The relative magnetoresistance $\Delta R/R = (R_\parallel - R_\perp)/R_\perp$ can reach 100% or more in multilayers with a high number of ferromagnetic/non-magnetic (F/N). In the original work of [11] this ratio is about 80% for Fe/Cr multilayers (see Fig. 5). For tunneling magnetoresistance, the relative magnetoresiatnace ratio ($\Delta R/R$) is as large as 1056% at room temperature for $CoFeB/MgO/CoFeB/MgO/CoFeB$ double barrier magnetic tunnel junction [13]. The GMR is an outstanding examples of how structuring materials at the nanoscale can bring to light fundamental effects that provide new functionalities.

Figure 6 illustrates two kinds of current flow directions. Figure 6(a) represents the case when the current flows in the plane of the interface (CIP-sensor) and Fig. 6(b) represents when the current flows perpendicular to the plane (CPP-sensor), which

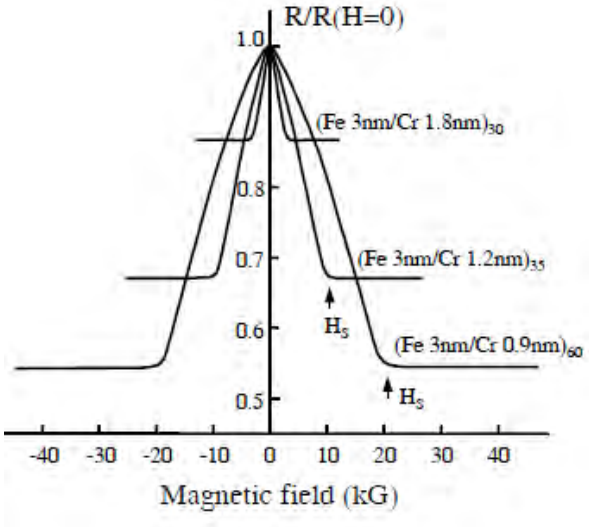

Figure 5: Normalized resistance versus applied magnetic field for several antiferromagnetically coupled Fe/Cr multilayers at 4.2K. Arrows indicate the saturation field H_S, which is required to overcome the antiferromagnetic interlayer coupling between the Fe layers and align their magnetizations parallel. After Baibich et al.[11].

has larger GMR than the CIP case.

Simple geometrical arguments based on the average electron propagation direction lead us to expect higher magnetoresistance values for spin valve in the current perpendicular to plane (CPP) configuration [12]. The fundamental study of CPP GMR was indeed extremely productive in terms of the new concepts of spin injection and spin accumulation [14]. In the ferromagnetic metals, we assume that $\tau_\uparrow \gg \tau_\downarrow$. So, when a current flows from a ferromagnetic layer (F) to a non-magnetic layer (N), away from the interface the current densities $j_\uparrow$ and $j_\downarrow$ must be very different on the ferromagnetic side, and equal on the non-magnetic side. The necessary adjustment requires that, in the area near the interfaces, more electrons from the spin-up channel flip their spins. This occurs through an accumulation of spin-up electrons, that is, a

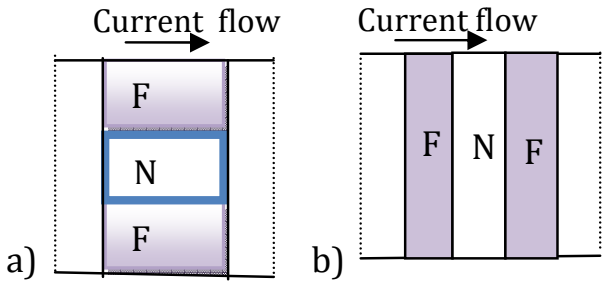

Figure 6: Schematic representation of (a) the current in plane (CIP), (b) the current perpendicular to the plane (CPP) giant magnetoresistance geometry.

splitting of the $E_{F\uparrow}$ and $E_{F\downarrow}$ Fermi energies, which induces spin-flips and adjusts the incoming and outgoing spin fluxes. The spin-accumulation decays exponentially on each side of the interface on the scale of the respective spin diffusion lengths L_{sf}^{F} and L_{sf}^{N} [4]. In this spin accumulation zone, the spin polarization of the current decreases progressively going from the magnetic conductor to the non-magnetic one, so that a spin-polarized current is injected into the non-magnetic metal up to a distance that can reach a few hundreds of nanometres, well beyond the ballistic range.

The highest GMR measured for antifferomagnetically-coupled magnetic layers. These magnetic multilayers require large magnetic fields for saturation. Because of this they are not best for technological application. The sturation field in the Fe/Cr multilayers are the order of $10 - 20\ kG$ which is three orders of magnitude higher than the fields required for applications [15]. The field for application is $\sim 20G$. The ratio $\Delta R/R$ per unit magnetic field of Fe/Cr is of the order of $0.01\%/G$, where as AMR of permalloy ($Ni_{80}Fe_{20}$) $1\%/G$.

The first commercial product using GMR is magnetic sensor. This sensor was produced in 1994 [16]. After 3 years, in 1997 IBM announced the product "read" heads

for magnetic hard disk, which has more economical impact [17] and references therein.

0.3 Spin-dependent transport

Electron has both charge (e) and spin (1/2). The discussion of electronics always related to the charge (e) of electron. But, the discussion of magnetism always attached to the spin of electron, and correspondingly, magnetic moment μ_B (Bohr magneton). In electronics, one can control the motion of electron using applied electric field (voltage, gate control) and by magnetic field. In magnetism we control electron motion using its spin, which can be controlled by magnetic field and also by electric field for relativistic case. This transport system which involves spin degree of freedom can referred as spin-dependent transport.

Spin transport in microstructure became one of the research potential in recent years. The electronic spin degree of freedom is on its way to replace the charge degree of freedom as carrier of information. In addition, the spin-based electronic devices have many advantages over the traditional semiconductor devices such as a long coherent lifetime, faster data processing speed, and lower electric-power consumption. In the above two sections, we have discussed the basic concepts we have to know in spitronics in general and particularly in GMR effects. These concepts are directly or indirectly related to spin-dependent transport. The spin dependent transport in ferromagnetic metals originate from the electronic structures of the materials. In rare earth metals, electrons responsible for transport and magnetism can be distinguished. But, in transition metals, this distinction is not clearly observed and as the result both s-and d-electrons contribute to transport and magnetism. The transition metals are also characterized by high Curie temperature.

In Fig. 1(b), we have shown the electronic structure of transition metals. The figure illustrates how the relative position of Fermi level E_F to the s-and d-states depends on the material. All materials which have imbalance of the spin populations at the Fermi level perform spin-polarized transport. This imbalance commonly occurs in ferromagnetic metals because the density of states available to spin-up and spin-down electrons is often nearly identical, but the states are shifted in energy with respect to each other (see Fig. 1(b)).

The shift in energy results in an unequal filling of the bands, which is the source of the net magnetic moment for the materials, but it can also cause the spin-up and spin-down carriers at the Fermi level to be unequal in number, character, and mobility. This inequality can produce a net spin polarization in a transport measurement, but the sign and magnitude of polarization depends on the specific measurement being made [17]. For example, a ferromagnetic metal may be used as a source of spin-polarized carriers injected into a semiconductor, a superconductor, or a normal metal or can be used to tunnel through an insulating barrier. The nature of the specific spin-polarized carriers and the electronic energy states associated with each material must be identified in each case. The most dramatic effects are generally seen for the most highly polarized currents; therefore, there are continuing efforts to find 100% spin-polarized conducting materials.

100% spin-polarized conducting materials are those materials that have only one occupied spin band at the Fermi level. Materials that are only partially polarized (such as Fe, Co, Ni, and their alloys, which have a polarization P of 40 to 50% [18]) are, however, adequate to develop technologically useful devices. P is defined in terms of the number of carriers n that have spin up (n_1) or spin down (n_2), as

$P = (n_1 n_2)/(n_1 + n_2)$. Because of the spin polarization of an electron current, the effects seen in solid state devices can be most readily visualized if one assumes that the current is 100% polarized. In that case, the only states that are available to the carriers are those for which the spins of the carriers are parallel to the spin direction of those states at the Fermi level. If the magnetization of the materials is reversed, the spin direction of those states also reverses. Thus, depending on the direction of magnetization of a material relative to the spin polarization of the current, a material can function as either a conductor or an insulator for electrons of a specific spin polarization [16].

In section 0.1, we have seen that the two-current model and this holds true for ferromagnetic transition metals. This is to mean that the electrical resistivity of ferromagnetic metals depends on spin. This spin dependence of resistivity is governed by the spin dependence of the electronic states near the Fermi level, and by the spin dependent impurity potentials in ferromagnetic alloys [10, 19].

The simplest expression of electrical conductivity is the Drude formula $\sigma = \frac{e^2 n \tau}{m^*}$ [20], where e, n, τ and m^* are electron charge, carrier density, lifetime and effective mass of electrons, respectively. These quantities are spin dependent and the most important is the spin dependence of the lifetime as it affects highly electron scattering. As explained in section 0.1, the lifetime is related to the mean free path l through the relation $l = v_F \tau$, where v_F is the Fermi velocity. For given ferromagnetic metals, l is much shorter than the spin-diffusion length λ_{spin}, and the spin of the carrier electrons are well conserved in the time scale τ [19].

The spin dependent Drude formula does not clearly show the contribution to the conductance by spin-up and spin-down separately. The first attempt to understand

the contribution of spin-up states and spin-down states in the conductivity of spin dependent transport was the experimental result of Fert, A., and Cambell, I. A. [21, 22]. They measured the residual resistivity and temperature dependence of various binary and ternary alloys and obtained the ratio $\rho_{\downarrow/\rho_{\uparrow}}$ $(= \sigma_{\uparrow}/\sigma_{\downarrow})$ for diluted alloys of Fe, Co and Ni metals. This ratio is called the α-parameter.

The magnetoresistance ratio (MR) given by equation (0.2.3) can be written in terms of the α-parameter as follow

$$MR = \left(\frac{1-\alpha}{1+\alpha}\right)^2. \tag{0.3.1}$$

Mark Johnson [23] reported the theory of spin-dependent transport in ferromagnet-semiconductor hetrostructures. The conductance of device structure of two-dimensional electron-gas (2DEG) channel and ferromagnetic source and/or drain for variety of magnetization configuration calculated using spin-dependent transport. The transport system developed in [23] used to address questions about the nature of spin-flipping scattering in quasi-one-dimensional semiconducting 2DEG. The result shows scattering events in which the spin state conserved are suppressed for a significant fraction of the carriers, but scattering events accompanied by spin-flip are not suppressed.

Today, spin-dependent transport have different applications. Some of these applications exist in magnetic memory, read/write heads, magnetic random access memory (MRAM), spin transistor, spin filter, spin diodes and spin quibits for quantum computing [3, 4]. The advantages of spin-dependent transport over the electron charge transport are multi-functionality, non-volatility, increased integration density, increased data processing speeds and low power consumption.

One important phenomena of spin transport system is spin injection. Silsbee [24] defined spin injection as the transfer of spin-polarized electrons across the first ferromagnetic layer to non-magnetic layer and then to the second ferromagnetic layer. The processes accompanied by diffusion across the non-magnetic metal and enhanced transmission in the second layer.

Semiconductor materials are the candidates of future in the field of spintronics. Successful application of the wide range of possible spin-dependent phenomena in semiconductor systems requires effective and efficient techniques for the electrical injection of strongly spin-polarized currents (spin currents), as well as electrical detection of such spin currents. For the semiconductor case, this detection could possibly occur either within the semiconductor or upon the current exiting the semiconductor system, depending on the device design. For practical applications, it is of course highly desirable that the generation, injection, and detection of such spin currents be accomplished without requiring the use of extremely strong magnetic fields and that these processes be effective at or above room temperature. The use of ferromagnetic metallic electrodes appears to be essential for most practical all-electrical spin-based devices before useful ferromagnet semiconductor are developed [25].

The spin injection system may include ohmic injection, tunnel injection, Ballistic injection, and hot electron injection. Ohmic injection is a method in which we have ohmic contact between a ferromagnetic metal and a semiconductor that produces spin-polarized current in semiconductor. Metal-semiconductor ohmic contacts result from heavily doping the semiconductor surface, leading to spin-flipping scattering and loss of the spin polarization. However, this method is not much successful, which is only about 4.5% [26]. Johnson [23, 27] use the advantage of the spin splitting of

the spin degeneracy of electrons confined in a semiconductor two-dimensional (2D) quantum well structure to over come the spin injection problem.

In 1992 Alvarado and Renaud [28] showed vacuum tunneling process inject spin effectively into semiconductor using scanning tunneling microscope with a ferromagnetic tip. Ballistic electron injection is an alternative technique of tunneling injection in the ballistic region. Experiments performed with point contacts formed between ferromagnetic and non-ferromagnetic metals have demonstrated the ballistic point-contact injection of $> 40\%$ spin-polarized currents into the the NFM. Hot electron injection involves the use of spin-polarized hot electrons having energies that are much greater than E_F by tunnel-injecting electrons into a ferromagnetic layer at energies much greater than E_F [29]. It is also shown that because of the majority-spin and minority-spin electrons have much different inelastic mean free paths, hot electron passage through, for example, a 3 nm Co layer, is sufficient to result in a ballistic electron current that is more than 90% polarized [30].

0.4 Problems of spintronics and perspectives.

Spintronics is a multidisciplinary field. The sources of this field includes the band theory, physics and technology of semiconductor microstructures, transistor electronics, magnetism and magnetic resonance superconductivity in mesoscopic systems, transport mechanism of all kinds (Boltzmann, ballistic, hopping, tunneling, etc.) macroscopically homogeneous and inhomogeneous systems [31]. To incorporate these ideas to the field of spintronics, good communications among scientists of the field around the world is highly expected. Before 1990s this was one of the grate challenge in the

field. Beside of its different advantages, the spin-dependent transport have many challenges. One of this is difficulty to achieve efficient injections of spin into nonmagnetic semiconductors at room temperature [32]. The other challenges addressed by experimental and theoretical groups in the field are optimization of electron spin life times, the detection of spin coherence in nanoscale structures, transport of spin-polarized carriers across relevant length scales and heterointerfaces, and the manipulation of both electron and nuclear spins on sufficiently fast time scales [25].

Spin injection into semiconductors is one of the great challenge of spintronics. Nearly all electronic components rely on semiconductors and the vision of spintronics is also to make interface itself with semiconductor technology. Unfortunately, maintaining spin polarization in semiconductor is very difficult. The reason is hard to form good atomic interface between a ferromagnetic metal and a semiconductor. Lack of good interface result in randomization of spin direction when electron transit through the interface.

The other serious problem is the ability to produce ultra-high-density spin-MRAM. This requires one transistor per cell (1T/1MTJ). However, the crosspoint memory architecture provides a way of reaching very high densities [4, 33], lower fabrication costs and a potential for 3D stacking of several recording layers. Intermediate cell structures such as 1T/4MTJ and multi-level cell operation achieved in thermally assisted switching-random accesses memory (TAS-RAM) [4] and references therein. These attempts to increase density is at the cost of smaller signal amplitude which slow read process. To over come this problem one has to get at least one order of magnitude in the amplitude of the magnetoresistance. The attempt to replace metallic ferromagnetic layers with 100% spin-polarized conductors such as half-metallic oxides

[34] or Heusler alloys [35, 36], or diluted magnetic semiconductors (DMS) [37, 38]. Spin filter [39], the process of tunnelling through a ferromagnetic barrier, and the transmission varies exponentially with the square root of the barrier height, which itself depends on electron spin direction versus barrier magnetization is one of the promising concept. The attempt to build a three-terminal device that can produce both the transistor effect and magnetoresistance in a single magnetic device [40] is also one hope of future spintronics. Here, these ideas show promising results at low temperature, but depend on materials issues such as obtaining Curie temperatures well above room temperature, mastering a complex stoichiometry (oxides, Heussler alloys) at an interface, or maintaining the fabrication thermal budget compatible with the complementary metal oxide semiconductor (CMOS) process, though these new materials usually require specific high-temperature growth. Moreover, three-terminal devices can so far provide only very small currents (microamperes at most), below CMOS compatibility levels, and independent writing of one or two magnetic layers may prove difficult to scale down even using spin transfer [4]. Even though, it is in its infant stage the magnetic mass storage from domain wall is promising [41]. The basic theory is that mixing spin transfer torque (electrons crossing a domain wall transfer spin angular momentum to the non-uniform magnetization in the wall) and mechanical momentum transfer (electrons are reflected from narrow walls), leading to a domain wall propagation controlled with a current density beyond a threshold [42]. Beside to this current density, the achievable domain wall speed is also great problem for fast data rates [43]. There is a hope to achieve higher density which requires replacing domain walls by smaller magnetization vortices [44].

In August 2010 Arthur J. Epstein et al. [45] succeeded in fabricating an hybrid material of semiconductor that is made from organic materials and special magnetic polymer semiconductor. The group of A. J. Epstein not only succeeded in fabrication of the material but also able to utilize spin degree of freedom. They created the first prototype plastic computer memory device that utilizes the spin of electrons to read and write data. The group successfully recorded data on it and retrieved the data by controlling the spins of electrons with a magnetic fields. But attaining higher data density is still the problem.

Chapter 1

Scattering Theory

Scattering theory is one of the fundamental concept needed in understanding the transport phenomena of electrons. As the title of the thesis indicates we have to develop some basic scattering theories for further discussion. In this Chapter, we discuss ways of obtaining spin polarized currents as the result of scattering, theories of Rashba and Dresselhaus spin-orbit interaction, scattering theory in 3D and 2D geometry.

1.1 Ways of obtaining spin polarized currents

Spin polarization is the degree to which the spin of electrons align with magnetic moment of ferromagnetic metals, or with the spin of the conduction electrons. Spin polarization of electrons obtained by applying external magnetic field to ferromagnetic metals. The spin polarized current results from the spin splitting of the energy band in a ferromagnet. The spin polarization of the electrons tunneling from a ferromagnetic metal across an insulator also results from the spin splitting of the energy band but can be quite different from the spin polarization of the conduction inside the ferromagnetic metal [46].

The spin splitting of the energy band in a ferromagnetic conductor gives rise to a spin dependence not only of the conduction but also of the tunneling probability through an insulating layer. This is the origin of the tunneling magnetoresistance (TMR) in a magnetic tunneling junction (MTJ). A MTJ is composed of two ferromagnetic metal layers sandwiching a very thin insulating barrier that electrons can tunnel through. The spin dependence of the tunneling from a ferromagnetic conductor can also be observed when the electrons tunnel to a superconductor.

Spin polarization in superconductor is an interplay between two fundamental features of quantum mechanics. The first feature is the quantum tunneling, which is the probability of the electron pairs in the superconductor to penetrate the energy barrier between the superconductor and the ferromagnet. The second feature is quantum coherence, the unique feature of quantum system to be in a state with two or more possible outcomes at any instant time [47].

Non-equilibrium spin polarization can be obtained locally in the bulk of semiconductor using ferromagnetic-metal scanning tunneling microscopy (STM) tips [48], or by optical pumping techniques [49-51].

Electrical spin transfer method is one of the successful method in inducing spin polarization in semiconductor devices. About 30% efficient electrical spin injection from a magnetic metal/tunnel barrier contact into a semiconductor (Fe/AlGaAs) near room temperature was obtained [52]. Similar works of [53] shows 9% injected spin polarization at $80K$ in $CoFe/AlO_x/(Al,Ga)/GaAs$ surface-emitting spin-light emitting diode (LED). Recent reports of Saroj P. Dash et al. [54] shows room-temperature electrical injection of spin polarization into n-type and p-type silicon from ferromagnetic tunnel contact, spin manipulation using the Hanle effect and the electrical detection

of the induced spin accumulation. They obtained large spin splitting as large as 2.9 meV. Other group [55] reported electrical spin injection into silicon using MgO tunnel barrier (Fe/MgO) which spin injection signal was observed up to 120 K with spin diffusion length of 2.25 μm.

Other methods of spin polarization includes the spin-orbit interaction which uses gate voltage as controlling mechanism and the origin of the spin splitting is the Rashba mechanism [56, 57], where the interface electric field results in splitting, and the interaction of conduction electron with nuclear spin [58] in semiconductors.

1.2 Theories of Rashba and Dresselhaus spin-orbit interaction

The concept of spin-orbit interaction is the central point of spin dynamics in semiconductor spintronics [7]. The spin-orbit interaction originates from the relativistic theory of Dirac's equation [59-61] to assure symmetry in the wave equation with respect to space and time derivatives. The Dirac's equation may be obtained by considering the general form of equation

$$i\hbar\frac{\partial\psi(\mathbf{r},t)}{\partial t} = \hat{H}\psi(\mathbf{r},t). \tag{1.2.1}$$

We require the condition that the left and right hand side of equation (1.2.1) on the same footing. Since the first derivative with respect to time enters on the left, the Hamiltonian must contain a linear space derivative, that is, the Hamiltonian must be linear in the momentum, $\mathbf{p} = -i\hbar\nabla$. Thus we assume that the Hamiltonian has the form

$$\hat{H} = c\alpha.\mathbf{p} + \beta mc^2, \tag{1.2.2}$$

where α and β are arbitrary coefficients. By imposing certain requirements on the solutions of (1.2.2), such as that it gives the correct energy-momentum relation $E^2 = p^2c^2 + m^2c^4$ we obtain conditions on the quantities α and β. These conditions may be satisfied by the 4×4 matrices representations

$$\alpha = \begin{bmatrix} 0 & \hat{\sigma} \\ \hat{\sigma} & 0 \end{bmatrix} \tag{1.2.3}$$

and

$$\beta = \begin{bmatrix} \mathbf{1} & 0 \\ 0 & \mathbf{-1} \end{bmatrix}, \tag{1.2.4}$$

where the σ_i are the Pauli matrices with

$\sigma_x = \begin{bmatrix} 0 & 1 \\ 1 & 0 \end{bmatrix}$, $\sigma_y = \begin{bmatrix} 0 & -i \\ i & 0 \end{bmatrix}$, $\sigma_z = \begin{bmatrix} 1 & 0 \\ 0 & -1 \end{bmatrix}$, and $\mathbf{1} = \begin{bmatrix} 1 & 0 \\ 0 & 1 \end{bmatrix}$.

Since matrices elements are four component matrices, the wave function appeared in equation (1.2.1) also has four components. Two of the components correspond to positive-energy solutions and the other two correspond to negative-energy solutions. From a Lagrangian formulation [62] we find that the effect of an external electromagnetic field described by the vector potential $\mathbf{A}$ and the scalar potential ϕ may be included by making the substitutions $\mathbf{p} \rightarrow \mathbf{p} - (e/c)\mathbf{A}$ and adding $e\phi$ to the Hamiltonian. Thus, the Dirac equation becomes

$$i\hbar\frac{\partial\psi}{\partial t} = \left[c\alpha \cdot (\mathbf{p} - \frac{e}{c}\mathbf{A}) + \beta mc^2 + e\phi\right]\psi. \tag{1.2.5}$$

Since the energies encountered in magnetic phenomena are much smaller than mc^2, it is convenient to decouple the positive- and negative-energy solutions. This is accomplished by a canonical transformation due to Foldy and Wouthuysen [63]. The

resulting Hamiltonian associated with the positive-energy solutions has the form

$$\hat{H} = \left[mc^2 + \frac{1}{2m}\left(\mathbf{p} - \frac{e}{c}\mathbf{A}\right)^2 - \frac{p^4}{8m^3c^2}\right] + e\phi - \frac{e\hbar}{2mc}\hat{\sigma}\cdot\mathbf{H} - \frac{ie\hbar^2}{8m^2c^2}\hat{\sigma}\cdot\vec{\nabla}\times\mathbf{E} - \frac{e\hbar}{4m^2c^2}\hat{\sigma}\cdot\mathbf{E}\times\mathbf{p} - \frac{e\hbar^2}{8m^2c^2}\vec{\nabla}\cdot\mathbf{E}. \tag{1.2.6}$$

We are interested to the last four terms. The term

$$\frac{e\hbar}{2mc}\hat{\sigma}\cdot\mathbf{H}$$

corresponds to the interaction of the intrinsic spin of the electron with the external field **H**. The next two terms are spin-orbit terms. In a stationary vector potential $\vec{\nabla}\times\mathbf{E} = 0$. And, if the scalar potential, V(r), is spherically symmetric,

$$\hat{\sigma}\cdot\vec{E}\times\vec{p} = -\frac{1}{r}\frac{\partial V}{\partial r}\hat{\sigma}\cdot\vec{r}\times\vec{p} = \frac{\hbar}{r}\frac{\partial V}{\partial r}\hat{\sigma}\cdot\vec{L},$$

where $\hbar\vec{L} = \vec{r}\times\vec{p}$. With this the spin-orbit term reduced to

$$\frac{e\hbar^2}{4m^2c^2}\frac{1}{r}\frac{\partial V}{\partial r}\hat{\sigma}\cdot\vec{L}. \tag{1.2.7}$$

This is what would be expected for an electron spin interacting with the field produced by its orbital motion, except that it is reduced by a factor of 1/2 due to relativistic kinematics, also known as the Thomas precession. The last term in (1.2.6), the so-called Darwin term, represents a correction to the Coulomb interaction due to fluctuations in the electron position arising from the presence of the negative-energy component in the wave function. The term $p^4/8m^3c^2$ in (1.2.6) is very small, and along with the Darwin term, it may be neglected for our purposes. If we define the zero of energy as the rest-mass energy, the Hamiltonian which governs the magnetic behavior of an electron is

$$\hat{H} = \frac{1}{2m}\left(\mathbf{p} - \frac{e}{c}\mathbf{A}\right)^2 + e\phi - \frac{e\hbar}{2mc}\hat{\sigma}\cdot\mathbf{H} + \frac{e\hbar^2}{4m^2c^2}\frac{1}{r}\frac{\partial V}{\partial r}\hat{\sigma}\cdot\vec{L}. \tag{1.2.8}$$

In $III-V$ semiconductor heterostructures, there are two effects contributing to the spin-orbit interaction: (i) the structure inversion asymmetry (SIA) of electrostatic confinement potential at hetero-interface, that is, $\nabla V = \hat{z}(dV/dz)$, known as Rashba effect, and (ii) the bulk inversion asymmetry (BIA) of the lattice structure in which the coupling between s-wave of atom A and p-wave of atom B is not equal and that between p-wave of atom A and s-wave of atom B, and this is called Dresselhaus effect. The Rashba Hamiltonian for SIA term can be written as

$$\hat{H} = \frac{\hat{\vec{p}}^2}{2m} + \frac{\alpha}{\hbar}\left(\hat{\vec{\sigma}} \times \hat{\vec{p}}\right)_z$$

$$\hat{H} = \begin{pmatrix} E_0 - \frac{\hbar^2}{2m}\left(\frac{\partial^2}{\partial x^2} + \frac{\partial^2}{\partial y^2}\right) & \langle \alpha E_z \rangle \left(\frac{\partial}{\partial x} - i\frac{\partial}{\partial y}\right) \\ \langle \alpha E_z \rangle \left(\frac{\partial}{\partial x} + i\frac{\partial}{\partial y}\right) & E_0 - \frac{\hbar^2}{2m}\left(\frac{\partial^2}{\partial x^2} + \frac{\partial^2}{\partial y^2}\right) \end{pmatrix}, \tag{1.2.9}$$

where $\langle \alpha E_z \rangle$ is the expectation value over the lowest subband with energy E_0. The Rashba coefficient α is proportional to the electric field built at hetero-interface; $\alpha = \alpha_0 e\mathbf{E}$ [64, 65].

The Rashba Hamiltonian of infinite two-dimensional electron gases (2DEG) with kinetic energy plus the spin-orbit coupling term is

$$\hat{H}_{2D} = \frac{\hat{p}_x^2 + \hat{p}_y^2}{2m} + \frac{\alpha}{\hbar}(\hat{p}_y\hat{\sigma}_x - \hat{p}_x\hat{\sigma}_y). \tag{1.2.10}$$

Since Hamiltonian commutes with the 2D momentum operator, we can classify its eigenvectors and eigenvalues with wave numbers k_x, k_y [66]:

$$\hat{H}\psi_\pm = \begin{pmatrix} \frac{\hbar^2}{2m}\left(k_x^2 + k_y^2\right) & i\alpha k_x + \alpha k_y \\ -i\alpha k_x + \alpha k_y & \frac{\hbar^2}{2m}\left(k_x^2 + k_y^2\right) \end{pmatrix} \psi_\pm = E_\pm \psi_\pm,$$

where

$$\psi_+ = \exp i(k_x x + k_y y) \begin{pmatrix} \cos\phi/2 \\ -\sin\phi/2 \end{pmatrix}, \quad \psi_- = \exp i(k_x x + k_y y) \begin{pmatrix} \sin\phi/2 \\ \cos\phi/2 \end{pmatrix}$$

with $\phi = \arctan \frac{k_y}{k_x}$, and

$$E_{\pm} = \frac{\hbar^2 k^2}{2m} \pm \alpha k, \qquad k = |\vec{k}|.$$

From the expression of the eigenstates we see that the Rashba term is not able to produce a spontaneous spin polarization of electron quantum states but spin degeneracy on the Fermi surface is lifted. Experiments show that the Rashba coupling strength can be tuned via proper gating of the structure, which makes the Rashba interaction very appealing for potential technological applications involving spin control [56, 67]. The Dresselhaus interaction, with coupling strength β, originates in bulk inversion asymmetry (BIA) which is inherent to zinc-blende structures [68] is given by

$$\hat{H}_D = \frac{\beta}{\hbar}(\hat{\sigma}_x \hat{p}_x - \hat{\sigma}_y \hat{p}_y). \tag{1.2.11}$$

The Rashba interaction widely used in the past in 2DEG semiconductors. The two Hamiltonians were observed and used for studying different features of the materials. Features like the cause of spin splitting in two-dimensional electron and hole [69], calculation of the ballistic spin transport properties of quasi-one-dimensional nanowires [70], spin-split resonant tunneling [71], spin current generation and detection [72], dissipationless spin currents at thermodynamic equilibrium [73], evaluation of the quantum and transport lifetimes of two-dimensional electron gas [74], dissipationless spin currents in paramagnetic materials [75], experimental separation of spin-orbit coupling strengths in semiconductor quantum wells [76], shifting of spin-split subbands in the energy wave vector plane [77], spin transport of heavy holes in $III - V$ semiconductor quantum wells [78], the Zitterbewegung motion of the waves packets in $III - V$ Zinc-blende semiconductor quantum wells [79], enhancement of the electron-phonon interaction and polaron mass correction [80], spin accumulations

in quantum wires phonon [81], spin splitting of a metallic surface-state band on a semiconductor surface [82], have been predicted and observed for spin-orbit coupled systems of Rashba type.

On the other hand, features like controlling in-plane transport of spin-polarized electrons in $III-V$ heterostructures [83], spin Hall conductivity in disordered two-dimensional electron gas [84], magnetoresistance of subband structure of semiconductor wires [85], measurements of spin dynamics in two-dimensional electron gas $GaAs/GaAlAs$ quantum wells [86], controlling the spin and orbital resonance [87], and relations between convectional and torque spin Hall conductivities [88] have been predicted and employed both Rashba and Dresselhaus interactions.

From equation (1.2.7) the spin-orbit interaction term is proportional to $(v/c)^2$. As the result, the Rashba spin-orbit coupling constant α and the Dresselhaus coupling constant β are also proportional to $(v/c)^2$. Experimental values of α for different materials ranges from $6\times10^{-12}eVm$ to $0.4\times10^{-11}eVm$. For example, the experimental value of α is $0.9\times10^{-11}eVm$ for $GaSb/InAs/GaSb$ quantum well at electron density of $1\times10^{12}cm^{-2}$ [89], $1.5\times10^{-11}eVm$ for In_xGa_{1-x}/InP quantum wells when the magnetic field $\vec{B}$ goes to zero at electron density of $0.7\times10^{12}cm^{-2}$ [67], $10^{-11}eVm$ for $In_{0.53}Ga_{0.47}As/In_{0.52}Al_{0.48}As$ heterostructure at electron density of $1.6\times10^{12}cm{-}2$ [56], $0.6\times10^{-11}eVm$ for $InAs/AlAs$ quantum well independent of electron density [90], $3\times10^{-11}eVm$ for $p-$ type bulk of $InAs$ at electron density of $2.2\times10^{12}cm^{-2}$ [91], $3\times10^{-11}eVm$ for $In_{0.75}Ga_{0.25}As/In_{0.75}Al_{0.25}As$ heterojunctions at electron density $\sim1.0\times10^{12}cm^{-2}$ [92] and $4\times10^{-11}eVm$ for $InAs$ quantum wells at electron density of $0.9\pm0.02\times10^{12}cm^{-2}$ [93]. The value of α_0 ($\alpha=\alpha_0e\mathbf{E}$) for bulk $InAs$ is $110\mathring{A}^2$ [93].

1.3 3D scattering theory

In this section we consider the general theory of scattering for non-relativistic and elastic collision. In classical mechanics, collisions of two particles are entirely determined by their velocities and impact parameter (the distance at which they would pass if they did not interact). In quantum mechanics the situation is completely different as the motion is with definite velocities the concept of the path is meaningless, and therefore so is the impact parameter. The problem of an elastic collision, like any problem of two bodies, amounts to a problem of the scattering of a single particle, with the reduced mass, in the field $V(r)$ of a fixed center of force. In this section we shall always use a system of coordinates in which the center of mass is at rest, and m will denote the reduced mass of the colliding particles.

The motion of a particle (wave) is governed by the time-dependent Schrödinger equation

$$[-\frac{\hbar^2}{2m}\nabla^2 + V(\vec{r})]\Psi(\vec{r},t) = i\hbar\frac{\partial}{\partial t}\Psi(\vec{r},t). \tag{1.3.1}$$

We are interested in the stationary solution of this equation of the form

$$\Psi(\vec{r},t) = \psi_{\vec{k}_0}(\vec{r})\exp(-iEt), \tag{1.3.2}$$

where $E = k_0^2\hbar^2/2m$ is the incident electron energy and $\vec{k}_0$ is the wave vector of the incident particle. Substitution of this expression into (1.3.1) yield the time independent Schrödinger equation

$$[-\frac{\hbar^2}{2m}\nabla^2 + V(\vec{r})]\psi_{\vec{k}_0} = E\psi_{\vec{k}_0}(\vec{r}) \tag{1.3.3}$$

A free particle moving in the positive direction of the z-axis is described by a plane

wave, which we take in the form $\psi = e^{ik_0 z}$, i.e. we normalize so that the current density in the wave is equal to the particle velocity v. The scattered particles are described, at a great distance from the scattering center (for potentials that vanish faster than r^{-1} as $r \to \infty$), by an outgoing spherical wave of the form $f(\theta)e^{i\vec{k}\cdot\vec{r}}/r$ [60, 94], where $f(\theta)$ is some function of the scattering angle θ (the angle between the z-axis and the direction of the scattered particle). This function is called the scattering amplitude, a quantity of central importance in scattering theory. Thus the exact wave function, which is a solution of Schrödinger's equation with potential energy $V(r)$, must have at large distances the asymptotic form

$$\psi \approx e^{ik_0 z} + f(\theta)\frac{e^{i\vec{k}\cdot\vec{r}}}{r}. \tag{1.3.4}$$

The probability per unit time that the scattered particle will pass through a surface element $dS = r^2 d\Omega$ (where $d\Omega = 2\pi \sin\theta d\theta$ is an element of solid angle) is $(v/r^2)|f(\theta)|^2 dS = v|f(\theta)|^2 d\Omega$. Its ratio to the current density in the incident wave is

$$d\sigma = |f(\theta)|^2 d\Omega = 2\pi \sin\theta |f(\theta)|^2 d\theta \tag{1.3.5}$$

Here, $d\sigma$ is called the cross-section and have a unit of area.

A solution of Schrödinger equation (1.3.3) is simplified for spherically symmetric potential $V(r)$ about the z-axis, the direction of the incident particles. Any such solution can be represented as a superposition of wave functions of the continuous spectrum, corresponding to motion of particles with given energy $E = k_0^2\hbar^2/2m$ and orbital angular momenta having various magnitudes l and magnetic zero z-components; these functions are independent of the azimuthal angle ϕ round the z-axis, i.e. they are axially symmetric. Thus, the required wave function can be obtained through utilization

of Hamiltonian operator in spherical polar coordinates, that is

$$-\frac{\hbar^2}{2m}\left[\frac{1}{r^2}\frac{\partial}{\partial r}\left(r^2\frac{\partial}{\partial r}\right)+\frac{1}{r^2\sin\theta}\frac{\partial}{\partial\theta}\left(\sin\theta\frac{\partial}{\partial\theta}\right)+\frac{1}{r^2\sin^2\theta}\frac{\partial^2}{\partial\phi^2}-\frac{2m}{\hbar^2}V(\vec{r})\right]\psi_{\vec{k}_0}=E\psi_{\vec{k}_0}(\vec{r}). \tag{1.3.6}$$

To solve this problem we employe the relation $\hat{\vec{L}}=(\vec{r}\times\hat{\vec{p}})/\hbar$ with its projection, $\hat{L}_z$, along the z-axis. The square of the angular momentum $\hat{\vec{L}}$ and its projection $\hat{L}_z$ are constants of motion (this satisfies the commutation $[\hat{H},\hat{\vec{L}}^2]=[\hat{H},\hat{L}_z]=0$). Here, $\hat{\vec{p}}=-i\hbar\vec{\nabla}$. Using this relation together with the expression of the Cartesian coordinates, (x,y,z), in terms of polar coordinates, (r,θ,ϕ), one can show that

$$\hat{\vec{L}}^2=-\hbar^2\left[\frac{1}{\sin\theta}\frac{\partial}{\partial\theta}\left(\sin\theta\frac{\partial}{\partial\theta}\right)+\frac{1}{\sin^2\theta}\frac{\partial^2}{\partial\phi^2}\right] \tag{1.3.7}$$

Since $\hat{\vec{L}}^2$ commutes with its components, $[\hat{\vec{L}}^2,\hat{L}_i]=0$, $i=x,y,z$, it can be diagonalized simultaneously with any one of these components by the same set of eigenfunctions. Choosing the component that lie along the z-axis, the corresponding eigenfunctions are the spherical harmonics [60, 94, 95], $Y_{lm}(\theta,\phi)$, such that

$$\hat{\vec{L}}^2Y_{lm}(\theta,\phi)=\hbar^2l(l+1)Y_{lm}(\theta,\phi), \tag{1.3.8}$$

and

$$\hat{L}_zY_{lm}(\theta,\phi)=\hbar mY_{lm}(\theta,\phi). \tag{1.3.9}$$

The subscript l and m in (1.3.8) and (1.3.9) are orbital angular momentum quantum number and the magnetic or azimuthal quantum number, respectively.

Inserting (1.3.7) into (1.3.6) we get

$$-\frac{\hbar^2}{2m}\left[\frac{1}{r^2}\frac{\partial}{\partial r}\left(r^2\frac{\partial}{\partial r}\right)-\frac{\hat{\vec{L}}^2}{\hbar^2r^2}-\frac{2m}{\hbar^2}V(\vec{r})\right]\psi_{\vec{k}_0}(\vec{r})=E\psi_{\vec{k}_0}(\vec{r}). \tag{1.3.10}$$

Because the commutation relations presented above, we need eigenfunctions that are common to $\hat{H}, \hat{\vec{L}}^2$ and $\hat{L}_z$. This property allow us to expand the scattering wave function $\psi_{\vec{k}_0}$ in partial waves corresponding to given values of the quantum numbers l and m [94, 96], in the form,

$$\psi(k_0, \vec{r}) = \sum_{l=0}^{\infty} \sum_{m=-l}^{m=l} c_{lm}(k) R_{lm}(k,r) Y_{lm}(\theta, \phi)$$

$$= \sum_{L} R_L(k,r) Y_L(\hat{r}), \tag{1.3.11}$$

where $k = \sqrt{2mE}/\hbar$, and $L = (l, m)$. Because of the azimuthal symmetry, the radial wave functions, $R_{lm}(k,r)$, are independent of the magnetic quantum number, m, and that each satisfies the radial Schrödinger equation,

$$-\frac{\hbar^2}{2m}\left[\frac{1}{r^2}\frac{d}{dr}\left(r^2\frac{d}{dr}\right) - \frac{l(l+1)}{r^2}\right] R_l(k,r) + V(r) R_l(k,r) = E R_l(k,r). \tag{1.3.12}$$

Here, we note that the required wave function must be regular at the origin and satisfy equation (1.3.4). Letting $R_l(k,r) = u_l(k,r)/r$ allows us to write (1.3.12) as

$$\left[\frac{d^2}{dr^2} + k^2 - \frac{l(l+1)}{r^2} - \frac{2mV(r)}{\hbar^2}\right] u_l(k.r) = 0. \tag{1.3.13}$$

These two equations, Eqs. (1.3.12) and (1.3.13), they are both ordinary differential equations and the functions R_l and u_l can be chosen to be real. This is from the fact that both real and imaginary parts of the complex functions would separately satisfy the differential equations.

For the case in which the potential $V(r)$ identically vanishes, the differential equation (1.3.13) reduced to the free particle equation.

$$\left[\frac{d^2}{dr^2} + k^2 - \frac{l(l+1)}{r^2}\right] y_l(k.r) = 0. \tag{1.3.14}$$

Once more we make a change of variables to $\rho = kr$ and defining the function $f_l(\rho) = y_l/\rho$, we can rewrite Eq. (1.3.14) in the form,

$$\left[\frac{d^2}{d\rho^2} + \frac{2}{\rho}\frac{d}{d\rho} + \left(1 - \frac{l(l+1)}{\rho^2}\right)\right] f_l(\rho) = 0. \tag{1.3.15}$$

This is the well-known spherical Bessel differential equation. The independent solutions of this equation that are often used in the scattering theory are the spherical Bessel functions, $J_l(\rho)$, the spherical Neumann functions, $Y_l(\rho)$, and the spherical Hankel functions, $H_l^{(+)}(\rho)$ of the first kind and $H_l^{(-)}(\rho)$ the second kind. The Hankel function are given in terms of the Bessel and Neumann functions by the relations [95],

$$H_l^{\pm}(\rho) = J_l(\rho) \pm iY_l(\rho), \tag{1.3.16}$$

The general solution of Eq. (1.3.14) can be written as

$$y_l(kr) = kr\left[C_l^1(k)J_{(l)}(kr) + C^{(2)}(k)Y_l(kr)\right] \tag{1.3.17}$$

or

$$y_l(kr) = kr\left[D_l^1(k)H_{(l)}^{(+)}(kr) + D^{(2)}(k)H_l^{(-)}(kr)\right], \tag{1.3.18}$$

where the integration constants $\left(C_l^{(1)}(k), C_l^{(2)}(k)\right)$ and $\left(D_l^{(1)}(k), D_l^{(2)}(k)\right)$ may still depends on the energy, k^2.

The Schrödinger equation for free motion.

$$-\frac{\hbar^2}{2m}\nabla^2\psi(\vec{r}) = E\psi(\vec{r}), \tag{1.3.19}$$

has the plane wave solutions, $\exp(i\vec{k}_0 \cdot \vec{r})$, which are also the eigenfunctions of the linear operator. Because of the eigenfunctions $J_l(kr)Y_{lm}(\hat{r})$ form a complete set, we may expand in terms of them to obtain

$$\exp(i\vec{k}_0 \cdot \vec{r}) = 4\pi\sum_{l=0}^{\infty}\sum_{m=-l}^{l} i^l J_l(kr)Y_{lm}^*(\hat{k}_0)Y_{lm}(\hat{r}). \tag{1.3.20}$$

Here, for free motion, the radial wave functions R_l are the spherical Bessel functions, J_l. Comparing Eqs. (1.3.11) and (1.3.20) allows us to identify the coefficients c_{lm} for the case on which the wave vector k_0 points in the direction of $\hat{z}$ axis. Denoting the coefficients for this special case by c^0_{lm},

$$c^0_{lm} = i^l[4\pi(2l+1)]^{1/2}\delta_{0,\phi}. \tag{1.3.21}$$

In (1.3.21) we have used the relation $Y_{lm}(0,\phi) = 0$ if $m \neq 0$ and $Y_{lm}(0,\phi) = \sqrt{\frac{2l+1}{4\pi}}$ if $m = 0$. Hence, Eq. (1.3.20) together with (1.3.21) gives the solution of free particle motion.

Now, once we get the free motion solution, it is may be easier to discuss the solution of the radial equations for the case of central potentials.

To obtain the solution of the radial equation (1.3.13), we examine the behavior of the wave function in regions far from the range of the force. Out side the range of the potential, the particle (or wave) executes essentially free motion and, according to our discussion above, we may write

$$u_l(kr) = kr\Big[C^{(1)}_l(k)J_l(kr) + C^{(2)}_l(k)Y_l(kr)\Big], \tag{1.3.22}$$

for $r >> a$, where a provides a measure of the extent of the potential region. As we are interested for large values of r, we can employe the following asymptotic results for $x \ll 1$ [95]

$$J_l(x) \to \frac{1}{x}\sin\big(x - \frac{l\pi}{2}\big), \tag{1.3.23}$$

$$Y_l(x) \to -\frac{1}{x}\cos\big(x - \frac{l\pi}{2}\big), \tag{1.3.24}$$

$$H^{(+)}_l(x) \to -i\frac{\exp\{i(x - \frac{l\pi}{2})\}}{x}, \tag{1.3.25}$$

and

$$H_l^{(-)}(x) \to i\frac{\exp\{-i(x-\frac{l\pi}{2})\}}{x}. \tag{1.3.26}$$

We can substitute Eqs. (1.3.23) and (1.3.24) into (1.3.22) to get

$$u_l(kr) \to kr\left[C_l^{(1)}(k)\frac{1}{kr}\sin\big(kr-\frac{l\pi}{2}\big) - C_l^{(2)}(k)\frac{1}{kr}\cos\big(kr-\frac{l\pi}{2}\big)\right]$$

$$\to A_l(k)\left[\frac{C_l^{(1)}(k)}{A_l(k)}\sin\big(kr-\frac{l\pi}{2}\big) - \frac{C_l^{(2)}(k)}{A_l(k)}\cos\big(kr-\frac{l\pi}{2}\big)\right]$$

with

$$A_l(k) = \sqrt{\big[C_l^{(1)}(k)\big]^2 + \big[C_l^{(2)}(k)\big]^2}. \tag{1.3.27}$$

We can define

$$\cos\delta_l(k) = \frac{C_l^{(1)}(k)}{A_l(k)}, \qquad \sin\delta_l(k) = \frac{C_l^{(2)}(k)}{A_l(k)}$$

or

$$\tan\delta_l(k) = -\frac{C_l^{(2)}(k)}{C_l^{(1)}(k)}. \tag{1.3.28}$$

Inserting (1.3.27) and (1.3.28) into (1.3.22) we can get

$$u_l(k,r) \to A_l(k)\sin\big[kr - \frac{l\pi}{2} + \delta_l(k)\big]. \tag{1.3.29}$$

Similarly from the relation $u_l(k,r) = rR_l(k,r)$ we can obtain similar expression as $r \to \infty$, that is

$$R_l(k,r) \to A_l'(k)[J_l(kr) - Y_l(kr)\tan\delta_l(k)], \tag{1.3.30}$$

where the constant $A_l'(k)$ is independent of r.

The quantity $\delta_l(k)$ introduced in Eq. (1.3.28) is called the phase shift for the lth

partial wave and contains the effect of the interaction on the scattered wave. Note that in the absence of the interaction, the phase shifts vanish and the radial functions reduced to the spherical Bessel functions.

Before leaving this section, we would like to present the scattering amplitude that we have introduced early in (1.3.4). The derivation of the scattering amplitude can be done by comparing the partial wave expansion (1.3.11) and (1.3.4). In driving an expression for the scattering amplitude, first we have to expand (1.3.4) using the identity given by (1.3.20) and we use the asymptotic result of $J_l(k,r)$ (as $r \to \infty$) given by (1.3.23). That is

$$\psi_{\vec{k}_0}(k,r) \to A(k)\Big[\sum_{l=0}^{\infty}(2l+1)i^l\frac{\sin(kr-\frac{l\pi}{2})}{kr}P_l(\cos\theta)+f(k,\theta,\phi)\frac{e^{ikr}}{r}\Big] \tag{1.3.31}$$

Here, we use the relation between Legendre polynomials and spherical harmonics $\big(P_l(\cos\theta)=\sqrt{\frac{4\pi}{2l+1}}\big)$ to obtain

$$\psi_{\vec{k}_0}(k,r) \to A(k)\Big[\sum_{l=0}^{\infty}\sum_{m=-l}^{l}\sqrt{4\pi(2l+1)}i^l\frac{\exp\{i(kr-\frac{l\phi}{2})\}-\exp\{-i(kr-\frac{l\pi}{2})\}}{2ikr}Y_{lm}(\hat{r})\delta_{m,0} + f(k,\theta,\phi)\frac{e^{ikr}}{r}\Big] \tag{1.3.32}$$

Similarly, we can consider the asymptotic behavior of the partial wave expansion of (1.3.11). Using the relation $u_l(k,r)=rR_l(k,r)$ together with (1.3.29) the result says

$$\psi_{\vec{k}_0}(k,r) \to \sum_{l=0}^{\infty}\sum_{m=-l}^{l}c_{lm}(k)A_l(k)\frac{1}{2ir}\big[\exp\big\{i(kr-\frac{l\pi}{2})+\delta_l\big\} - \exp\big\{-i(kr-\frac{l\pi}{2}+\delta_l)\big\}\big]Y_{lm}(\hat{r}). \tag{1.3.33}$$

Now we can compare the coefficients of the incoming spherical waves of (1.3.32) and (1.3.33). Hence,

$$c_{lm}=\frac{A(k)}{kA_l(k)}\sqrt{4\pi(2l+1)}i^l\exp\{i\delta_l\}\delta_{m,0}. \tag{1.3.34}$$

At this point we can rewrite the partial wave expansion (1.3.11) in the form of

$$\psi_{\vec{k}_0}(k,r) = A(k)\sum_{l=0}^{\infty}\frac{2l+1}{kA_l(k)}i^l\exp\{i\delta_l\}R_l(k,r)P_l(\cos\theta), \tag{1.3.35}$$

or

$$\psi_{\vec{k}_0}(k,r) = A(k)\sum_{l=0}^{\infty}\frac{\sqrt{4\pi(2l+1)}}{kA_l(k)}i^l\exp\{i\delta_l\}R_l(k,r)Y_{l,0}(\theta). \tag{1.3.36}$$

To get the scattering amplitude, we compare the coefficients of the out going spherical waves of (1.3.32) and (1.3.33).

$$f(k,\theta) = \frac{1}{2ki}\sum_{l=0}^{\infty}(2l+1)[\exp(2i\delta_k)-1]P_l(\cos\theta). \tag{1.3.37}$$

Equation (1.3.37) is the required form of the scattering amplitude. This can be also written in the form

$$f(k,\theta) = \sum_{l=0}^{\infty}(2l+1)a_l(k)P_l(\cos\theta), \tag{1.3.38}$$

where the partial wave amplitudes $a_l(k)$ are given by the expression,

$$\begin{aligned} a_l(k) &= \frac{1}{2ik}[\exp(2i\delta_l(k))-1] = \frac{1}{2ik}[S_l(k)-1] \\ &= \frac{1}{k}\exp(i\delta_l(k))\sin\delta_l(k), \end{aligned} \tag{1.3.39}$$

where $S_l(k) = \exp(2i\delta_l(k))$ called S-matrix element. From (1.3.39) one can deduce that for spherically symmetric potentials the scattering amplitudes are independent of the angle θ and ϕ and are determined completely from the concept of phase shifts. In this section, we have seen indetails of the general features of the 3D scattering theory for spherically symmetric potentials and the case of free particle motion. In next section we discuss the 2D scattering theory which has many different features than 3D scattering theory.

1.4 2D scattering theory

In the above section we have discussed the 3D scattering theory for general case and particularly for central potential. We have seen that the stationary solution of the Schrödinger equation is the superposition of the incoming plane wave and the out going spherical wave. In this section we also follow the same approach to find the stationary solution of the Schrödinger equation in 2D scattering system.

We consider a domain in which the stationary solution of the Schrödinger equation is known, and we lable these by $\psi(\vec{k}_0, \vec{\rho})$. That is

$$\psi(\vec{k}_0, \vec{\rho}) = e^{i\vec{k}_0 \cdot \vec{\rho}}. \tag{1.4.1}$$

In the presence of a potential there will be new stationary solutions, labeled by $\psi(\vec{k}, \vec{\rho})$ [60] and is given by

$$\psi(\vec{k}, \vec{\rho}) \ \overset{\rho \to \infty}{\sim} \ \psi(\vec{k}_0, \vec{\rho}) + f(\vec{k}, \vec{k}_0) \frac{e^{i\vec{k} \cdot \vec{\rho}}}{\sqrt{-i\rho}}, \tag{1.4.2}$$

where $\rho = \sqrt{x^2 + z^2}$ is the radius vector from the scattering center and φ is the angle between the vector $\vec{k}_0$ and the direction of scattering, $\vec{k}$. Here, $f(\vec{k}, \vec{k}_0)$ is the scattering amplitude, which in the two-dimensional case has the dimensions of square root of length. To simplify the problem we may chose the direction of the incident wave (particle) along z-axis so that in Eq. (1.4.1) $\vec{k}_0 \cdot \vec{\rho} = k_0 z$.

We assume the plane wave, $\psi(\vec{k}, \vec{\rho})$ is wide but finite so we may always go far enough away that the scattering at any angle but $\varphi = 0$ involves only the scattered part of the wave. The flux of the scattered wave is

$$\mathbf{j} = Im\{\psi^* \nabla \psi\} = \hat{y} \frac{\left| f(\vec{k}, \vec{k}_0) \right|^2}{\rho}. \tag{1.4.3}$$

For 2D elastic scattering we can write the Hamiltonian as

$$\begin{aligned}\hat{H}\psi(\vec{k},\vec{\rho}) &= E\psi(\vec{k},\vec{\rho}) \\ \Big[-\frac{\hbar^2}{2m}\nabla^2 + V(\vec{\rho})\Big]\psi(\vec{k},\vec{\rho}) &= \frac{\hbar^2 k^2}{2m}\psi(\vec{k},\vec{\rho}) \\ \big(\nabla^2 + k^2\big)\psi(\vec{k},\vec{\rho}) &= \frac{2m}{\hbar^2}V(\vec{\rho})\psi(\vec{k},\vec{\rho}) \qquad (1.4.4)\end{aligned}$$

Now we can introduce the Green's function $G(k,\vec{\rho}-\vec{\rho'})$ that obeys the equation

$$\big(\nabla^2 + k^2\big)G(k,\vec{\rho}-\vec{\rho'}) = \frac{2m}{\hbar^2}\delta^2(\vec{\rho}-\vec{\rho'}) \qquad (1.4.5)$$

The Green function's provides a solutions for (1.4.5)

$$\psi(\vec{k},\vec{\rho}) = e^{i\vec{k}\cdot\vec{\rho}} + \int d^2\rho' G(k,\vec{\rho}-\vec{\rho'})V(\vec{\rho'})\psi_0(\vec{k},\vec{\rho'}). \qquad (1.4.6)$$

At this point what important is determining the Green's function for 2D. This can be done as follow.

At $\rho = 0$ the Green's function obeys the wave eqution for a free particle. The solutions are Bessel functions $J_n(k\rho)$, and $Y_n(k\rho)$. Both are needed since the solutions are away from the origin. The combinations of these two functions that forms an out going wave is called a Hankel function:

$$H_n^{(1)}(z) = J_n(z) + iY_n(z), \qquad (1.4.7)$$

$$H_n^{(2)}(z) = J_n(z) - iY_n(z). \qquad (1.4.8)$$

$H_n^{(1)}(z)$ is an outgoing wave, while $H_n^{(2)}(z)$ is an incoming wave. We need the circularly symmetric solution $n = 0$. We assume the Green's function may have the form [97]

$$G(k,\rho) = \lambda H_0^{(1)}(k\rho), \qquad (1.4.9)$$

where λ is constant to be determined. The two-dimensional delta function located at the origin can be written as $\delta^2(\vec{\rho}-\vec{\rho'}) = \frac{\delta(\rho)}{2\pi\rho}$. Inserting this expression of delta function and (1.4.9) into (1.4.5) and integrating over the angle ϕ we obtain,

$$2\pi\left(\frac{1}{\rho}\frac{d}{d\rho}\big(\rho\frac{d}{d\rho}\big)+k^2\right)\lambda H_0^{(1)}(k\rho) = \frac{2m}{\hbar^2}\frac{\delta(\rho)}{\rho}. \tag{1.4.10}$$

Here, we can multiply both sides by $\rho/2\pi$ and then integrate each term by

$$\lim_{\varepsilon\to 0}\int_0^{\varepsilon} d\rho.$$

That is

$$\lim_{\varepsilon\to 0}\int_0^{\varepsilon} d\rho\left(\frac{d}{d\rho}\rho\frac{d}{d\rho}+\rho k^2\right)\lambda H_0^{(1)}(k\rho) = \frac{m}{\pi\hbar^2}\lim_{\varepsilon\to 0}\int_0^{\varepsilon}\delta(\rho)d\rho,$$

which gives

$$\lim_{\varepsilon\to 0}\varepsilon\frac{d}{d\varepsilon}\lambda H_0^{(1)}(k\varepsilon) = \frac{m}{\pi\hbar^2}. \tag{1.4.11}$$

Now we consider the right hand side of equation (1.4.7). The Bessel function $J_0(Z)$ and the Neumann function $Y_0(z)$ for small arguments are given by [95]

$$J_0(z) = \sum_{k=0}^{\infty}(-1)^k\frac{z^{2k}}{2^k(k!)^2} \simeq 1+O(z^2), \tag{1.4.12}$$

$$Y_0(z) = \frac{2J_0(z)}{\pi}\big(\ln\frac{z}{2}+C\big) - \frac{2}{\pi}\sum_{k=0}^{\infty}(-1)^k\frac{z^{2k}}{(k!)^2}\sum_{m=1}^{k}\frac{1}{m} \simeq \frac{2}{\pi}\ln z, \tag{1.4.13}$$

respectively.

$$\lim_{\varepsilon\to 0}\varepsilon\frac{d}{d\varepsilon}\lambda H_0^{(1)}(k\varepsilon) = \lim_{\varepsilon\to 0}\varepsilon\frac{d}{d\varepsilon}\lambda J_0(k\varepsilon) + i\lim_{\varepsilon\to 0}\varepsilon\frac{d}{d\varepsilon}\lambda Y_0(k\varepsilon).$$

Substituting Equations (1.4.12) and (1.4.13) in to the last expression and recalling small arguments of the function we obtain

$$\lim_{\varepsilon\to 0}\varepsilon\frac{d}{d\varepsilon}\lambda J_0(k\varepsilon) = 0,$$

and

$$i\lim_{\varepsilon\to 0}\varepsilon\frac{d}{d\varepsilon}\lambda Y_0(k\varepsilon)=i\frac{2\lambda}{\pi}.$$

Therefore, inserting this last result into (1.4.11)

$$\lambda=-i\frac{m}{2\hbar^2}\ , \tag{1.4.14}$$

and

$$G(k,\rho)=-i\frac{m}{2\hbar^2}H_0^{(1)}(k\rho). \tag{1.4.15}$$

The scattering wave at far distance can be obtained from the asymptotic behavior of $H_0^{(1)}(z)$ ($z=k|\vec{\rho}-\vec{\rho'}|\sim k(\rho-\vec{\rho'}\cdot\vec{n})$, where $\vec{n}=\vec{\rho}/\rho$ at far distance), which is

$$\lim_{z>>1}H_0^{(1)}(z)=\sqrt{\frac{2}{i\pi z}}e^{iz}. \tag{1.4.16}$$

Substituting (1.4.16) into (1.4.15) and the obtained result in to (1.4.6) we get

$$\psi(\vec{k},\vec{\rho})=e^{i\vec{k}_0\cdot\vec{\rho}}-\frac{m}{\hbar^2}\sqrt{\frac{i}{2\pi k\rho}}\int d^2\rho' e^{ik(\rho-\vec{\rho'}\cdot\vec{n})}V(\rho')\psi(\vec{k}_0,\vec{\rho'}). \tag{1.4.17}$$

Recalling that $\psi(\vec{k}_0,\vec{\rho'})=e^{i\vec{k}_0\cdot\vec{\rho'}}$ and inserting this into (1.4.17)

$$\psi(\vec{k},\vec{\rho})=e^{i\vec{k}_0\cdot\vec{\rho}}-\frac{m}{\hbar^2\sqrt{2\pi k}}\frac{e^{ik\rho}}{\sqrt{-i\rho}}\int d^2\rho' e^{-i\vec{q}\cdot\vec{\rho'}}V(\rho'), \tag{1.4.18}$$

where $\vec{q}=\vec{k}-\vec{k}_0$, $q=2k\sin(\varphi/2)$, $k^2=k_0^2=\frac{2mE}{\hbar^2}$ (here we consider the elastic collision).

The comparison between (1.4.2) and (1.4.18) shows the scattering amplitude is

$$f(k,\varphi)=-\frac{m}{\hbar^2}\frac{1}{\sqrt{2\pi k}}\int e^{-i\vec{q}\cdot\vec{\rho'}}V(\rho')d^2\rho'. \tag{1.4.19}$$

Equation (1.4.18) shows that the scattering amplitude has units of square root of length and the differential length

$$\frac{dL}{d\varphi}=|f(k,\varphi)|^2, \tag{1.4.20}$$

has a units of length.

Before ending this section, we note some features of 2D scattering theory as compared to 3D. One of the feature is that in 3D, as $E \to 0$, $\sigma \sim \lambda$ (wavelength) is finite. But, in 2D as $E \to 0$, $\tilde{L} \sim \lambda \to \infty$. The other feature is the logarithmic singularity of Green's function in 2D that prevents to single out simple idea of the scattering length in 2D. This singularity comes from the form of the free scattering solution of 2D (the equivalent of the 3D spherical harmonics).

As our main goal is scattering of elctrons in 2D system, we discuss the properties of two-dimension electron gas (2DEG) and its applications in next section.

1.5 Properties and applications of two-dimensional electron gas

A two-dimensional electron gas (2DEG) is a gas of electrons free to move in two dimensions (x, y), but tightly confined in the third dimension (z). The 2DEG trapped at a doped heterojunction is the most important low-dimensional system for electronic transport. It forms the core of a field-effect transistor, includes modulation-doped field effect transistor (MODFET) and high electron mobility transistor (HEMT) [98].

The 2DEG has many features that differs from three-dimension electrons in the bulk. One of the difference is the dispersion relation. In the effective mass approximation, the dispersion relation for a 2DEG is parabolic and the eigenenergies of the electrons with the momentum $\vec{k}$ are [99-100]

$$E = \varepsilon_n + \frac{\hbar^2}{2m^*}\big(k_x^2 + k_y^2\big), \tag{1.5.1}$$

where the index n numbers successive subbands, ε_n is the lowest energy of electrons in the n-th subband, and m^* is the effective mass of an electron. At low concentrations

(low Fermi level) and low temperatures, electrons populate only the lowest subband. In this case the electrons do not participate in the dynamics of orthogonal to the plane and the dynamics is that of a real 2DEG (two-dimensional electron gas in the quantum limit).

In such a system, electron states can be described as freely propagating plane waves and their in-plane wavefunctions are [99]

$$\Psi(x,y) = \frac{1}{\sqrt{S}} \exp(ik_x x) \exp(ik_y y), \tag{1.5.2}$$

where the factor $\frac{1}{\sqrt{S}}$ is a normalization constant.

The spin degenerate density of states D(E) for 2DEG is constant and determined by the effective mass [99-100].

$$D(E) = \frac{m^*}{\pi\hbar^2} = constant. \tag{1.5.3}$$

At equilibrium, the electron distribution in each subband in the transverse direction is given by the Fermi-Dirac distribution with the two-dimensional density of sates in (1.5.3):

$$N_n \sim \int_{\varepsilon_n}^{\infty} D(E) \left(\frac{1}{e^{(E-\mu)/(K_B T)} + 1} \right) dE, \tag{1.5.4}$$

where μ is the electrochemical potential. The evaluation of this integral gives

$$N_n = \frac{m^*}{\pi\hbar^2} K_B T ln \left(1 + e^{(\mu-\varepsilon_n)/(K_B T)} \right). \tag{1.5.5}$$

In 2DEG the electron dynamics orthogonal to the interfaces, where the confinement occurs, gives rise to localized states (the wave function of the trapped electron in quantum wells is different from 2DEG at heterojection). As the result, electron transport

in 2DEG is described by Boltzmann equation.

There is relevant difference between 2DEG and 3D electron transport. One of this difference is that the position of electrons in 2DEGs are described only by two continuous coordinates and two momentums define its velocity. A further quantum number indicates the orthogonal state, or the subband of the electron. The other difference is that the 2D density of states alters the scattering mechanism with respect to 3D case. Within a given band, the density of states is reduced by the reduced dimensionality, but the third dimension is recovered by inter-subband transitions.

In addition to what mentioned above properties, the 2DEGs exhibit some properties like reduced ionized-impurity scattering and high electron mobilities at low temperatures as large as $2.3 \times 10^6 cm^2/Vs$ for electrons [101]. This can be achieved with the help of modulation-doping technique, which keep charge carriers far away from the impurity which generate them. Further more, lattice vibrations contain confined modes, such as interface and slab modes, besides extended modes. The scattering result from surface-roughness is also one of the properties observed in 2DEGs.

Nowadays two-dimensional electron gases are used for different purposes. Some of these applications are high mobility electrons in modulated electron field effect transistor, observation of quantum Hall effect which could be useful in quantum information technology, magnetic recording sensors, organic filed effect transistor which is a key device for low cost and flexible plastic electronics used for optical measurements, charge-coupled device-in 2DEG-FET structures for digital circuity and microwaves (high mobility field effect transistor). It is also used in spintronic devices such as in spin transistor [102].

Chapter 2

Nanomagnetism, Properties of Nanomagnets, and Gigantic Nanomagnets

2.1 Nanomagnetism

The physics of nanomagnetism is concerned with the studies of magnetic phenomena specific to nanostructured materials, i.e., materials with the size of typical structural elements from 1 to 100 nm [103]. A porous specimen built of small particles is the simplest example of a nanostructured material. Due to dramatically enhanced surface-to-volume ratio, the magnetic properties of nanoparticles may be markedly different from those of the bulk material with the same chemical composition. Numerous experiments show that the magnetic properties of bulk ferromagnetic and antiferromagnetic materials are modified in the corresponding nanomaterials. Most surprisingly, nanostructured materials or thin films may show ferromagnetism at room temperatures even when the starting material is magnetically inactive.

When one enters the nanometer regime, a large fraction of the magnetic moment bearing species resides in the surface or interface, if we have an ultrathin magnetic

film five layers in thickness, 40% of the magnetic ions reside in such sites [46]. The key aspects of magnetism are very sensitive to local site local symmetry, and thus the magnetism in such a film will differ qualitatively from a bulk crystal made with the same constituents.

Bulk magnetic material is characterized by fundamental length scales. The lattice constant is the smallest such length, but there are two other important lengths that play a central role. These are the wavelength λ_T ($k_T = 2\pi/\lambda_T$, k_T is wave vector) of thermally exited spin waves and the exchange length L_{ex}. For any linear dimension L of the sample, when $k_T L \leq 1$, we are in the region where the fundamental properties of the material differ from those in bulk and are affected by sample size. The exchange length is the thickness of a domain wall of Bloch character in a bulk ferromagnet. The exchange length lies in the range of $5 - 10\ nm$ [46]. In ferromagnetic films whose thickness is small compared to this length, the magnetization is uniform in the direction normal to the surfaces. Such a film's domain structure and hysteresis loop differ qualitatively from a bulk ferromagnet.

As it was explained in Chapter 0.1, progress in nanofabrication techniques has made it possible to create artificial structures such as magnetic multilayers and nanocontacts, that the characteristic length L of which can be shorter than the spin diffusion length λ_{spin} or mean free path length l and even can be close to the Fermi wavelength λ_F. This property is the cornerstone of spintronics and the novel transport phenomena occurs for this case. Some examples of these are giant magnetoresistance (GMR), tunnel magnetoresistance (TMR), and ballistic magnetoresistance (BMR) [10].

Applications such as spin filtering, sensing, and ultra-high density magnetic and magneto-optic recording are few of the items in the field of nanomagnetism. The

magnetism of ultra-small entities is not stable due to super-paramagnetism. Thermal fluctuations, the major obstacle for further size reduction of magnetic devices [104], have become an urgent issue, and ways to enhance anisotropy and the pinning of magnetic moments need attention.

Anisotropy due to the long-ranged magnetic dipolar coupling between the atomic magnetic moments, and spin-orbit interactions of the moment bearing electrons which allow the moment to sense the local crystalline axes are observed in the ultrathin film. If dipolar interactions are the only sources of anisotropy in a ferromagnetic film, the shape anisotropy forces the magnetization to always lie parallel to the film surfaces. The spin-orbit anisotropy activated by the low-symmetry sites at surfaces can be two orders of magnitude larger that found in bulk materials synthesized from the same atomic species. Here, surface anisotropy remains small compared to the very strong inter spin exchange coupling that derive the ferromagnetic order. This indicates that the surface or interface anisotropy strength varies inversely with thickness of the film [104].

Other type of anisotropy is anisotropy in energy. This anisotropy controls the orientation of the magnetization in the ground state of the ultrathin film and the response of the film to applied direct current or very low-frequency external magnetic fields.

As the lateral size of the nanomagnetic material approaches 1 nm, the change in electronic structure significantly influences all key parameters such as the exchange constant, magnetic anisotropy field (e.g. magnetocrystalline, strain, surface, atomic step, or edge induced) and spin polarization (and hence effective magnetization) [46].

The existence of magnetic properties of a material can be checked through its structural and geometrical properties, such as the interatomic distances, coordination number (the number of nearest neighbors), and symmetry. When the structure of the materials are modified in the nanoscale, it resulted in different properties. In reduced size (nanoscale size) the coordination number decreases and as the result there is a decrease in the overlap of the nearby atomic orbital. This in turn gives leads to the sharper density of states. Hence, the magnetic moment per atom increase.

Further more, with decrease of coordination number, the effect of vacancies on the nearest-neighbor magnetic atoms tends to enhance its magnetic moment. On the contrary, surface relaxation decreases the interlayer separation, overlap increases, and magnetic moment decreases. Comparison of the effect of interatomic distances with coordination numbers show that the interatomic distances result in more effects. Thus, the monolayers of magnetic elements are likely to provide a very strong moment [103] and references therein. Basically, the reduced coordination number and symmetry changes are expected to narrow the electronic bands. This enhances magnetism in ferromagnetic materials and may cause magnetization in nonmagnetic materials. Some metals lik Au, Pd, and Rh are called nonmagnetic materials in the normal situation, but these materials can exhibit magnetic properties in nanoscale with semiconductor nanoparticles and quantum dot GaN, CdS, $CdSe$ [103]. This un expected property, called emergent behavior, is due to the nanometer-scale changes of the structure.

The magnetic properties of the ferromagnetic nanostructures are highly sensitive to the conditions of synthesis or subsequent annealing rather than the content of metallic

impurities as it is too low to account for the observed value of magnetization. Analysis of the synthesis and annealing conditions provides the basis for the models for ferromagnetism in these systems. In several cases, the firm evidence for magnetism in nonmagnetic materials has been obtained from elementally sensitive magnetic measurements like X-ray magnetic circular dichroism. This is the case of Au, Ag, Cu nanoparticles, some oxides, and graphite [103].

In 1999 Hori et al. [105] obseved magnetism in $\sim 3\ nm$ gold nanoparticles with an unexpected large magnetic moment about 20 spins per particle which later showed by Vager et al. the magnetism originates from orbital momentum [106]. The observed intrinsic magnetism of $Au-$ atoms in thiol-capped gold nanoparticles, which possess a permanent magnetization at room temperature, and the same result for Ag and Cu using X-ray magnetic circular dichroism method answered the question of the origin of magnetism [107]. Other elements like Ru, Rh, and Pd exhibit nanoscale magnetism. A Pd nanoparticle containing only single Co atom exhibits a single-domain nanomagnet behavior [108]. It was also shown that Pb and Pt nanowires are ferromagnetic at room temperature, in contrast to their bulk [109].

The results on metal films and nanoparticles point out that the possibility to observe magnetism at nanoscale in materials without transition metals and rare earths atom, and are fundamental to understand the magnetic properties of surfaces.

Nanoscale magnetism also observed in semiconductor materials like GaN and CdS [110], and $GaAs/GaMnAs$ [111]. Diluted magnetic oxides (DMO) are other groups that exhibit nanoscale magnetism. DMO were initially considered as a variety of diluted magnetic semiconductors (DMS), doped $III-V$ compounds like $(Ga, Mn)As$ or $II-VI$ materials such as $(Zn, Mn)Te$ alloys [103].

Carbon nanoparticles are other candidates of nanomagnetic materials. Experiments show that the magnetization value of carbon nanoparticles are one order larger than the expected saturated magnetization due to any possible transition metal impurity. In present section we have discussed nanomagnetism and some properties of the nanomagnetic materials based on its origin. One of the basic issue in fabrication and application of nanomagnetic materials is the Curie temperature. Below we discuss this temperature for nanomagnetic materials.

2.2 Curie temperature of nanomagnets

In this section we present general features of Curie temperature of nanomagnetic materials. It is known that the Curie temperature is one of the cental issue in magnetic materials. Experiments show that ultrathin films display ferromagnetism at finite temperature, many right down to the monolayer level. The Curie temperature may be depressed relative to that appropriate to the bulk material, but such materials are perfectly good ferromagnets so far as experiment is concerned [46].

In the $3d$ ferromagnets, Curie temperatures range from 500 to 1000K or more. In [112], it was shown that the Curie temperature $T_C^{(2)}$ in two-dimensional film subject to weak uniaxial anisotropy is related to the Curie temperature $T_C^{(3)}$ of its three-dimensional counterpart through the relation $T_C^{(2)} = 2T^{(3)}/ln(\pi^2 J/K)$, where J is the strength of the interspin exchange coupling, and K that of the uniaxial anisotropy. Even if $K/J \sim 0.01$; we find $T_C^{(2)} \sim 0.3T_C^{(3)}$. Thus, very tiny anisotropies can drive the Curie temperature of the ultrathin films to substantial values. The two-dimensional Heisenberg ferromagnet is the most intriguing system. While thermal fluctuations break up its long-ranged order at any finite temperature, it really wants to order and even

very weak symmetry breaking interactions such as the anisotropies discussed above can drive the Curie temperature of a monolayer film of $3d$ magnetic ions up to the vicinity of room temperature. Thus, anisotropy again enters as a central feature of ultrathin films, not only because of its role in devices, but because it is the key to the commonly observed ferromagnetic order in these systems.

Optimization of the magnetism in $GaAs/MnAs/GaAlAs$ layers has been performed by adjusting the position of the $MnAs$ layers for maximum overlap with the two-dimensional hole gas ($2DHG$). However, postgrowth annealing of the samples leads to the largest increase in Curie temperature (up to 172 K) [113]. The Curie temperature has been further increased in these structures by inverting the $2DHG$, such that the p-doped $AlGaAs$ layer is grown after the magnetic layer at low temperature. After postgrowth annealing, a hysteresis in the Hall resistance was observed up to 250 K, the highest Curie temperature in the $GaMnAs$ system reported so far [114]. The low Curie temperature is one of the difficulty observed in spintronics or nanomagnetism. Developing different methods to enhance Curie temperature is a cental issue for the development of the field.

2.3 Domain structure of nanomagnets

Ferromagnetic materials get their magnetic properties not only because their atoms carry a magnetic moment but also because the material is made up of small regions known as magnetic domains. In each domain, all of the atomic dipoles are coupled together in a preferential direction. Ferromagnetic materials become magnetized when the magnetic domains within the material are aligned. This can be done by placing the material in a strong external magnetic field or by passing electrical current

through the material. The more domains that are aligned, the stronger the magnetic field in the material. When all of the domains are aligned, the material is said to be magnetically saturated. When a material is magnetically saturated, no additional amount of external magnetization force will cause an increase in its internal level of magnetization. The boundary between neighbored domains are domain walls. Magnetic domains are formed in the process of minimizing the magnetic energy of a ferromagnetic crystal. Magnetic nanoparticles with diameters smaller than 50 nm are single domains. The definition of a single domain is that every spin in the particle has the same direction, meaning that the total magnetic moment of the particle is the sum of all spins.

Magnetic domain structure can be studied by various methods, involving different physical principles of magnetic contrast formation. These methods include Bitter pattern technique (the specimen surface under study is decorated by fine magnetic particles and the resulting domain pattern is usually observed by optical microscopy or scanning electron microscopy), magnetic force microscopy (MFM) (based on the magnetostatic interaction between the magnetic specimen and magnetic tip placed over the specimen surface), the type-I magnetic contrast of scanning electron microscopy (SEM) (due to the Lorentz deflection of secondary electrons by the stray fields above the specimen surface), the colloid-SEM method and the Fresnel mode of transmission electron microscopy (TEM) (allows to study magnetic structures of thin films thinner than about 100 nm).

Understanding the nature of magnetism at the nanometer length scale is of interest from fundamental perspective and for the development of next generation spin-based devices [115]. For structures below a critical dimension, the competition between the

magnetostatic energy and exchange energy is predicted to suppress magnetic domain formation, leading to single domain structures. In [115], using X-ray photoemission electron microscopy and magnetic force microscopy, they probed the micromagnetism in high polarized Lanthanum Strontium Manganese Oxide. The result is that the magnetic domain structure exists in a delicate balance between shape, magnetocrystalline, magnetostatic, and magnetostatic energies, which can be tuned by changing the substrate orintation, the film thickness, the island size, and the island shape.

The earlier works of [116] show that the local magnetic structure of submicron colossal magnetoresistance islands and their evolution as a function of applied field. The group observed a characteristic multidomain structure with perpendicular orientation at room temperature. The magnetization reversal of the islands in magnetic fields perpendicular and parallel to the substrate is dominated by strong domain wall pinning. The strong domain wall pinning together with geometrical confinement in the submicron colossal magnetoresistance structure gives rise to reproducible multidomain structure.

L. Kong et al. [117] succeded in fabricating and characterizing spin-valve structures consisting of $NiFe(10\ nm)/Cu(13\ nm)/Co(10\ nm)/NiFe(2\ nm)$ with size down to $70\ nm \times 1\ \mu m$. In this experiment, when the multilayer bar width was less than $200\ nm$, the formation of single domain was found. As the pattern width decreased, the switching fields for both the hard layer and soft layer increased. This shows that the magnetization property of nanoscale magnets highly depends on the size of domain structure.

In condensed matter, domains can be circular, square, irregular, elongated, and striped, all of which have varied sizes and dimensions. The understanding of a specific

domain pattern depends on the magnetic history and anisotropic effects. Domain patterns are not identical when demagnetization was carried out before using alternating magnetic fields. Smaller magnetic particles possess simpler domain formations. Less domain walls are needed in order to minimize the stray energy [118]. Large particles exhibit a lot of domain walls.

Magnetic domain formation dependence on size with an in-plane anisotropy [118], the spacing between each nanomagnet is always at least equal to the diameter of the nanomagnet. For the smallest structure it is as large as three times the diameter. This ensures that there is negligible magnetic interaction between the nanomagnets. The hysteresis loop as a function of the diameter and thickness of nanomagnets [119] when the magnetic field applied in the plane of nanomagnets in the direction of the uniaxial anisotropy easy axis shows two properties.

The first property was appeared for a nanomagnet of 300 nm in diameter and 10 nm thickness. For this case, as the applied field is reduced from minus saturation the nanomagnets retain full moment until a critical field slightly below zero. At this point nearly all magnetization is lost. The magnetization then progressively reappears as the field is increased from zero until positive saturation is achieved. The sudden loss of magnetization close to zero field is very characteristic of the formation of a flux closing configuration; the simplest one is a magnetic vortex which the magnetization vector remains parallel to nearest edge in at all points in the circular nanomagnet.

The second property observed from the hysteresis of the loop is for nanomagnets of 100 nm and thickness of 10 nm. These loops retains a high remanence of about 80% and switch at a very low field about 5 Oersted (5 Oe), which is the characteristic

behavior of single domain. All nanomagnets within the array retain all of their magnetization to form an array of giant spins and magnetization reversal occurs by each giant spin rotating coherently [118]. Recent works of [120] present novel magnetic domain structure in iron meteorite induced by the presence of $L1_0$-$FeNi$. According to technical magnetization, magnetic domain structure is determined so as to minimize the total energy.

As discused above, ferromagnetic materials contain differently magnetized domains separated by domain walls, they closely resemble magnetic trilayers. Hence, one can predict similar spin dependent conduction electron scattering at the domain walls as in magnetic trilayers. Viret et al. [121] measured the magnetoresistance of Co and Ni films as a function of external field. By combining longitudinal and transverse magnetoresistance they were able to isolate the magnetoresistance due to the domain walls from anisotropic magnetoresistance.

Finally, before ending this chapter we discuss few aspects of nanomagnets with giant magnetic moments.

2.4 Nanomagnets with giant magnetic moment

In the Introductory Chapter, we have been presented the details of magnetoresistance and some properties of giant magnetoresistance. In this section we try to discus nanomagnets with giant magnetic moment.

The early works of G. J. Nieuwenhuys [122] show that some diluted impurities of Mn, Fe, and Co on Pd have giant magnetic moment of, $8\mu_B$, $12.6\mu_B$ and $10.8\mu_B$, respectively. There are also many theoretical and experimental works showed that the magnetization of the nanoparticles enormously increased over the bulk while the

size of the particles reduced. For example, the theoretical calculation made by Lie Liu et al. [123] for nanotorus (carbon nanotubes bent into rings) gives giant magnetic moment thousands of times larger than other tori with similar structures. As the main reason of the source of this giant magnetic moment the group argued that the radius of the torus and therefore the area it enclosed affected its magnetic moment. In 2003, S. B. Ogale et al. [124] reported a giant magnetic moment of $7.5 \pm 0.5 \mu_B/Co$ atom in thin film of Co-doped $SnO_{2-\delta}$. This material exhibit ferromagnetism with a Curie temperature close to 650 K. Thin films of $Sn_{0.95}Cr_{0.05}O_2$ grown on $LaAlO_3$ substrates have shown a giant magnetic moment of $6\mu_B/Cr$, which is 20-30 times larger than that of thin films grown under the same conditions on $SrTiO_3$ substrates [125]. The temperature at which this giant ferromagnetic moment obtained is above room temperature, 400K. The theoretical study carried out by Mukul Kabir et al. [126] on the electronic and magnetic properties of pure and arsenic-doped manganese clusters from the density functional theory using spin-polarized gradient approximation for exchange-correlation energy shows a giant magnetic moment of $9\mu_B$ and $17\mu_B$ for $Mn - Mn$ coupling for Mn_2As and Mn_4As clusters, respectively.

Recently, Jung et al. [127] reported the giant magnetic moment of Oxygen-free $CuNi$ nanoparticles. In their work they investigated giant magnetic moment, which is inversely linear in temperature, and shows weak ferromagnetic behavior that support the Langevin-type superparamagnetic nature of $CuNi$ nanoparticles. The source of this giant magnetic moment is associated with the uncompensated spins on the surface of the particles.

Large magnetic moment also has been investigated in cluster of Co_{13} at transition metal $(TM)_{20}$ [128]. Here, the transition metals used are Mn, Fe, Co, and Ni. The

maximum magnetic moment obtained is 113 μ_B for Co_{13} at Mn_{20}. This large magnetic moments mainly resulted from the special core-shell structure and the weak interaction between the transition metal and other atoms.

The magnetic dipole-dipole interaction between nanomagnets having huge magnetic moments can have a strength comparable to that of the Van der Walls interaction between them, and it can be manipulated by applying an external magnetic field of conventional strength. In [129], a magnetic sponge capable of absorbing and desorbing guest molecules with changes in the applied magnetic fields where developed. The group obtained the magnetization of the sponge with long-alkyl-chain bridges (30 C atoms) exhibited 400% increase after cooling in the presence of an applied field of 7 T relative to that in the absence of magnetic field.

Giant magnetic moment enhancement of nanoparticles embedded in multi-walled carbon nanotubes attracts great attentions. The room-temperature saturation magnetization of the nickel nanoparticles embedded in the multiwalled carbon nanotubes is enhanced by a factor of 3.4 ± 1.0 as compared with what they would be expected to have for free nanoparticles [130], which assumed to be resulted from the interplay between ferromagnetism in the nickel nanoparticles and strong diamagnetism in multi-walled carbon nanotubes. Similar studies were also carried on multi-walled carbon nanotubes embedded with Fe_3C, Ni, Fe, and Fe_3O_4 magnetic nanoparticles [131]. The study shows that the saturation magnetizations of Fe, Fe_3O_4, Ni magnetic nanoparticles are enhanced by a factor of about 3 as compared with what they would be expected to have for free magnetic nanoparticles. In contrast, a smaller enhancement factor of 1.6 is found for Fe_3C nanoparticles. These enhancements can be regarded as giant magnetic moment of nanoparticles. The possible origin of this

giant magnetization enhancement of the magnetic nanoparticles embedded in multi-walled carbon nanotubes is that a strong diamagnetic tube that enhance the extrinsic magnetic moment of a (single-domain) magnetic embedded inside it.

In the last two chapters and the present one, we discussed the basic concepts we need for the following chapters, the main parts of our research. We may summarize the above chapters as follow. In the introductory chapter we have seen that basic concepts of spintronics like the electronic structure, two channel conduction, magnetoresistive ratio, relaxation time, and tunneling magnetoresstance (TMR). We have been also discussed the giant magnetoresitance (GMR), in plane and perpendicular currents, the perspective and the challenges of spintronics. The chapter gives good background of our works. Chapter 1 mainly devoted to the scattering theory; basically ways of obtaining spin polarized currents, Rashba and Dressselhaus spin-orbit interaction, 3D and 2D scattering theories, and the properties and applications of the 2DEGs. Chapter 1 is one of the cornerstone of our research as we deal with 2D spin-dependent electron scattering. The formulas derived in chapter 1 highly used in the coming three chapters. The theories and experimental results presented in chapter 2 be compared with our findings in the coming chapters.

In the next four chapters we presnt 2D electron scattering by neutral and charged nanomagnets for both polarized and unpolarized beam of electrons.

Chapter 3

2D Spin-Dependent Scattering of Polarized Beams of Electron by Neutral Nanomagnets

3.1 Born approximation in 2D scattering

The possibility of separation of the electron spins of different orientation with current in semiconductors was discussed in [6] about 40 years ago. Basically this paper is one of the first that started such fast developed field called now the spintronics. The main objectives of spintronics is finding reliable methods of controlling the spin orientations and arrangement of the so called spin currents. One of these methods is the usage of the spin-orbit interaction coupling of the electron momentum and its spin. It is known, that spin orbit coupling appears as the term proportional to $(v/c)^2$ (v is a velocity of a particle and c is the speed of light) in the non-relativistic limit of the Dirac equation [59] and is relatively small.

To exploit the spin degree of freedom there should be mechanism(s) to control their polarization. Many research recently conducted in these area use the spin-orbit interaction terms based on Rashba or Dresselhaus gate voltage that makes it

convenient in spintronics applications as discussed in chapter 1. In this chapter, we analyze the scattering of electrons by magnetized nanoparticles or nanomagnets.

The interaction of magnetic moments of the electron and of nanomagnet appears in the Pauli equation in the zeroth order with respect to the small parameter v/c. Below, we consider the two-dimensional (2D) scattering of electrons by the magnetic moment and show how the scattering amplitudes depend on mutual orientation of the magnetic moment of the nanomagnet and the electron, the energy of electron and the scattering angle. This section provides the Born approximation method to determine the scattering amplitude and the dependence of scattering length on spin orientation. The Pauli equation of an electron in a constant homogeneous magnetic field $\vec{B}$ has a form

$$\hat{H} = \frac{1}{2m}\left[\hat{\vec{p}} + \frac{e}{c}\vec{A}\right]^2 + \mu_B \vec{\sigma} \cdot \vec{B}. \tag{3.1.1}$$

Here m and e are the electron mass and its absolute charge respectively, $\hat{\vec{p}}$ is the momentum operator, $\vec{A}$ is the vector potential corresponding to the magnetic field $\vec{B}$, $\mu_B = e\hbar/2mc$ is the Bohr magneton, and $\hat{\sigma}$ are the Pauli matrices.

Further, we use a model of the nanomagnet particle as a point like dipole $\vec{\mu}$ built in a sphere of radius a, which specifies a radius of the nanoparticle. The magnetic moment of the nanoparticle is taken from the experimental data [122, 124,125, 129-131], theoretical work of [123, 126], and computer simulation [128] on gigantic magnetic moments. The vector potential of the dipole $\vec{\mu}$ and its magnetic field are given by the expressions

$$\vec{A} = \frac{\vec{\mu} \times \vec{\rho}}{\rho^3}, \quad \vec{B} = \frac{3(\vec{\mu} \cdot \vec{n})\vec{n} - \vec{\mu}}{\rho^3}, \tag{3.1.2}$$

where $\vec{n}$ is a unit vector along the radius vector $\vec{\rho}$. Substituting (3.1.2) in to (3.1.1)

we obtain,

$$\hat{H} = \frac{1}{2m}\hat{\vec{p}}^2 + \frac{e}{mc}\frac{\vec{\mu}\cdot\hat{\vec{L}}}{\rho^3} + \frac{\mu_B}{\rho^3}\Big(3(\vec{\mu}\cdot\vec{n})\vec{n}\cdot\hat{\sigma} - \vec{\mu}\cdot\hat{\sigma}\Big), \tag{3.1.3}$$

where, $\hat{\vec{L}} = \vec{\rho}\times\hat{\vec{p}}$ is the angular momentum operator and the term proportional to e^2/c^2 neglected.

Let the magnetic moment of the nanoparticle $\vec{\mu}$ and the electron momentum $\vec{p}$ be in the $x-z$ plane. In this 2D geometry, (3.1.3) takes the form

$$\hat{H} = \frac{1}{2m}\hat{\vec{p}}_2^2 + \frac{\mu_B}{\rho^3}\Big(3(\vec{\mu}\cdot\vec{n})\vec{n}\cdot\hat{\sigma} - \vec{\mu}\cdot\hat{\sigma}\Big). \tag{3.1.4}$$

Here, $\hat{\vec{p}}_2^2$ is the two dimensional momentum operator and ρ is the two dimensional radius vector in the $x-z$ plane and we took in to account that the term $\sim \vec{\mu}\cdot\hat{\vec{L}}$ in our geometry vanishes because $\vec{\mu}$ is perpendicular to the angular momentum $\hat{\vec{L}}$.

The Schrodinger equation corresponding to Hamiltonian (3.1.4) takes the form

$$\Big(\nabla_2^2 + k^2\Big)\vec{\psi} = \frac{2m}{\hbar^2}\hat{V}\vec{\psi}, \tag{3.1.5}$$

where, $k^2 = 2mE/\hbar^2$, E is the energy of the scattered electron, ∇_2^2 is 2D Laplace operator

$$\hat{V} = \frac{\mu_B}{\rho^3}\Big(3(\vec{\mu}\cdot\vec{n})\vec{n}\cdot\hat{\sigma} - \vec{\mu}\cdot\hat{\sigma}\Big), \tag{3.1.6}$$

and $\vec{\psi} = \begin{vmatrix} \psi_1 \\ \psi_2 \end{vmatrix}$ is a two-component spinor.

Equation (3.1.5) is a typical equation from the scattering theory with the interaction potential $\hat{V}$ depending on spin variables. Basically (3.1.5) is a system of two equations for unknown functions of ψ_1 and ψ_2.

The differential equation (3.1.5) (as discussed in chapter one equation (1.4.6)) can be

formally presented as the following integral equation

$$\vec{\psi}(\vec{\rho}) = \vec{\psi}_0(\vec{\rho}) + \frac{2m}{\hbar^2}\int G(\vec{\rho},\vec{\rho'})\hat{V}(\vec{\rho'})\vec{\psi}_0(\vec{\rho'})d^2\rho', \tag{3.1.7}$$

with $\vec{\psi}_0$ is a solution of the homogeneous equation

$$\left(\nabla_2^2 + k^2\right)\vec{\psi}_0 = 0 \tag{3.1.8}$$

and $G(\vec{\rho},\vec{\rho'})$ is the Green function of this equation, that was given by equation (1.4.15) of chapter one.

Below, we consider the case when the interaction $\hat{V}$ can be treated as a small perturbation. In this case, the solution of equation (3.1.7) is (see equations (1.4.17-1.4.19))

$$\vec{\psi}(\vec{\rho}) = \vec{\psi}_0(\vec{\rho}) + \vec{\psi}_s(\vec{\rho}), \tag{3.1.9}$$

where $\vec{\psi}_0(\vec{\rho})$ is a solution of the homogeneous equation (3.1.8) (incident wave) and $\vec{\psi}_s(\vec{\rho})$ is a scattered wave that is a small correction to $\vec{\psi}_0$.

Keeping this in mind, we can present the correction ψ_s in the form

$$\vec{\psi}_s(\vec{\rho}) = \frac{2m}{\hbar^2}\int G(\vec{\rho},\vec{\rho'})\hat{V}(\vec{\rho'})\vec{\psi}_0(\vec{\rho'})d^2\rho'. \tag{3.1.10}$$

Let the incident wave be the plane wave propagating along the z-axis

$$\vec{\psi}_0(\vec{\rho}) = \exp(ik_0 z)\vec{\chi}_0(S) \tag{3.1.11}$$

with the spin function $\vec{\chi}_0(S)$. At large distances ($\rho'/\rho \ll 1$) from the scattering center (nanomagnet), the scattered wave in 2D geometry is a cylindrical wave as given by equation (1.4.2)

$$\vec{\psi}_s(\rho) = \vec{f}(\varphi)\frac{e^{ik\rho}}{\sqrt{-i\rho}} \tag{3.1.12}$$

with the "scattering amplitude" $\vec{f}(\varphi) = \left| \begin{array}{c} f_1(\varphi) \\ f_2(\varphi) \end{array} \right|$ that is a two component spinor and has dimension of the square root of length, φ is the scattering angle between the incident wave vector $\vec{k_0}$ (along z-axis) and the scattered wave vector $\vec{k}$ (along $\vec{\rho}$, see Fig.3.1).

The Green function in (3.1.10) in the cylindrical geometry is the first kind zeroth order Hankel function [95] given by

$$G(\vec{\rho}, \vec{\rho'}) = -\frac{i}{4} H_0^{(1)}(k|\vec{\rho} - \vec{\rho'}|).$$

At $(\rho'/\rho \ll 1)$, it has the asymptotic behaviour (equation (1.4.16))

$$H_0^{(1)}(k|\vec{\rho} - \vec{\rho'}|) \simeq \frac{1-i}{\sqrt{\pi\rho k}} e^{ik(\rho - \vec{\rho'}\cdot\vec{n})}$$

where, $\vec{n} = \vec{\rho}/\rho$. Hence

$$G(\vec{\rho}, \vec{\rho'}) = -\frac{1}{\sqrt{8\pi k}} \frac{1}{\sqrt{-i\rho}} e^{ik(\rho - \vec{\rho'}\cdot\vec{n})}. \tag{3.1.13}$$

Substituting (3.1.11) and (3.1.13) into (3.1.10) and comparing the result with (3.1.12) we can single out the amplitude of the scattered cylindrical

$$\vec{f}(k, \varphi) = \left| \begin{array}{c} f_1(k, \varphi) \\ f_2(k, \varphi) \end{array} \right| = -\frac{m}{\hbar^2 \sqrt{2\pi k}} \int e^{-i\vec{q}\cdot\vec{\rho'}} \hat{V}(\vec{\rho'}) d^2\rho' \vec{\chi}_0(S), \tag{3.1.14}$$

where $\vec{q} = \vec{k} - \vec{k}_0$, $k_0^2 = k^2 = \frac{2mE}{\hbar^2}$, $q = 2k_0 \sin\varphi/2$ (here we consider the elastic collision). Equation (3.1.14) is the Born approximation of scattering amplitudes in 2D spin-dependent electron scattering.

We use (3.1.14) to find the differential scattering lengths in 2D spin-dependent electron scattering by nanomagnet. The scattering lengths for the case under consideration will be discussed below in details and the amplitude square of equation (3.1.14)

has the unit of length where it has been the unit of area in the case of 3D scattering as shown in Chapter 1.

For the spin independent scattering potential $\hat{V}$, the scattering amplitude becomes a scalar and (3.1.14) coincides with the known formula for 2D scattering in Born approximation [60]. In the next section we use (3.1.14) to calculate the scattering amplitude of electrons by magnetic nanoparticles.

3.2 Born approximation in 2D spin-dependent electron scattering by single neutral nanomagnet

Now we discuss the applicability of the Born approximation. It is valid only for conditions that satisfies equation (3.1.9) with the second term in the right hand side of (3.1.9) is very small. It works well for the scattering of particles with arbitrary energy provided that the following inequality holds true [60]

$$|V| << \hbar^2/m\bar{\rho}^2.$$

Here, $\bar{\rho}$ is the range of action of the scattering potential $\hat{V}(\rho)$, which is given by equation (3.1.6). For evaluations we set $|V| \sim \frac{\mu\mu_B}{\rho^3}$. Due to the fast decay of the dipole-dipole interaction with distance we take $\bar{\rho} = 2a$ (a is radius of the nanomagnet). Keeping this in mind, we obtain that the Born approximation is applicable if the following inequality is true

$$\frac{16\pi\nu\mu_B^2 n_a m a^2}{3\hbar^2} \ll 1. \tag{3.2.1}$$

For the magnetic moment of nanoparticle, we used the formula $\mu = \frac{4\pi}{3}\nu\mu_B n_a a^3$, ν is a number of Bohr magnetons carried by the ferromagnetic atom, and n_a is the density

of atoms of the nanomagnets. In agreement with the experimental data [122, 124, 125, 127, 129-131], theoretical data [123, 126], and computer simulation [128] ν lies in the range $6 - 113\mu_B$.

Due to the relative weakness of the spin-nanomagnet interaction, inequality (3.2.1) can be satisfied only for nanoparticles of the following size

$$a < \frac{100}{\sqrt{\nu}} nm.$$

This condition is obtained by substituting the numerical values of the parameters entering into (3.2.1) with $n_a = 10^{22} cm^{-3}$.

3.3 Scattering lengths of polarized beams of electrons scattered by nanomagnets

3.3.1 The magnetic moment $\vec{\mu}$ parallel to initial velocity of electrons

Consider the scattering of electrons (coming from infinity parallel to the z-axis) by a nanomagnet oriented along the z-axis. To evaluate the integral (3.1.14) one has to choose appropriate coordinate system. Figure 3.1 shows two coordinate systems. In the first one (x, z), the magnetic moment of nanoparticle $\vec{\mu}$ is along the z axis. But the calculation of the integral in (3.1.14) is convenient to carry out in another coordinate system with x'-axis directed along $\vec{q}$, in which the dot product in the exponent (3.1.14) has the simplest form $\vec{q} \cdot \vec{\rho'} = q\rho' \cos\varphi'$ (ρ' and φ' are variables of integration). The operator of potential energy (3.1.6) in this coordinate system takes

the form

$$\hat{V} = \frac{\mu_B}{\rho'^3}\left\{\left[\mu_{x'}\left(3\cos^2\varphi' - 1\right) + \frac{3}{2}\mu_{z'}\sin 2\varphi'\right]\hat{\sigma}_{x'} + \left[\mu_{z'}\left(3\sin^2\varphi' - 1\right) + \frac{3}{2}\mu_{x'}\sin 2\varphi'\right]\hat{\sigma}_{z'}\right\}. \tag{3.3.1}$$

In this coordinate system the magnetic moment μ has two components $\mu_{z'} = \mu\cos\frac{\varphi}{2}$, and $\mu_{x'} = -\mu\sin\frac{\varphi}{2}$. In the $x - z$ coordinate system $\vec{\chi}_0(S) = \vec{\chi}_\uparrow(S) = \begin{vmatrix} 1 \\ 0 \end{vmatrix}$ for the

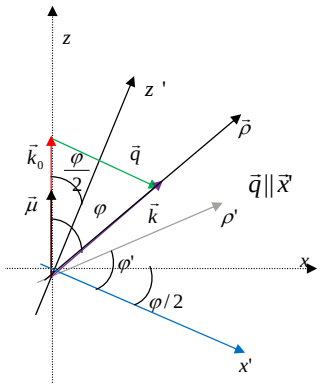

Figure 3.1: The coordinate systems: (x, z) and (x', z'). The x' axis is parallel to $\vec{q}$.

electron with spin parallel to $\vec{\mu}$. But the calculation of (3.1.14) is carried out in the coordinate system $x' - z'$, we have to transform the spinor wave function $\vec{\chi}_0(S)$ to this coordinate system. The operator of rotation of a two component spinor through a finite angle θ about the given axis is given by [60]

$$\hat{U}_n = \mathbf{1}\cos\frac{\theta}{2} + i\mathbf{n}\cdot\hat{\sigma}\sin\frac{\theta}{2}, \tag{3.3.2}$$

where $\mathbf{1} = \begin{pmatrix} 1 & 0 \\ 0 & 1 \end{pmatrix}$ and $\mathbf{n}$ is a unit vector along the rotation axis. From Fig. 3.1 one can see that the required transformation is rotation about the y-axis in the $x - z$

plane by an angle $\theta = \frac{\varphi}{2}$. The operator of this rotation is

$$\hat{U}_y = \begin{pmatrix} \cos\frac{\varphi}{4} & \sin\frac{\varphi}{4} \\ -\sin\frac{\varphi}{4} & \cos\frac{\varphi}{4} \end{pmatrix}. \tag{3.3.3}$$

Hence, the spinor $\vec{\chi}_{0\uparrow}(S)$ in the x', z' coordinate system expressed as

$$\vec{\chi'}_{\uparrow}(S) = \hat{U}_y \begin{vmatrix} 1 \\ 0 \end{vmatrix} = \begin{pmatrix} \cos\frac{\varphi}{4} \\ -\sin\frac{\varphi}{4} \end{pmatrix}.$$

Inserting (3.3.1) into (3.1.14) with account of results $\hat{\sigma}_x\vec{\chi'}_{\uparrow}(S)$ and $\hat{\sigma}_z\vec{\chi'}_{\uparrow}(S)$ ($\hat{\sigma_x} = \begin{pmatrix} 0 & 1 \\ 1 & 0 \end{pmatrix}$ and $\hat{\sigma_z} = \begin{pmatrix} 1 & 0 \\ 0 & -1 \end{pmatrix}$), we obtain

$$\vec{f'}(\varphi) = \gamma \int_0^{2\pi}\int_a^{\infty} \frac{e^{-i\rho' q\cos\varphi'}}{\rho'^2}\Big[\big[-\sin\frac{\varphi}{2}(3\cos^2\varphi' - 1) + \frac{3}{2}\cos\frac{\varphi}{2}\sin 2\varphi'\big]\begin{pmatrix} -\sin\frac{\varphi}{4} \\ \cos\frac{\varphi}{4} \end{pmatrix} +$$

$$\big[\cos\frac{\varphi}{2}(3\sin^2\varphi' - 1) - \frac{3}{2}\sin\frac{\varphi}{2}\sin 2\varphi'\big]\begin{pmatrix} \cos\frac{\varphi}{4} \\ \sin\frac{\varphi}{4} \end{pmatrix}\Big] d\rho' d\varphi', \tag{3.3.4}$$

where $\gamma = -\frac{m\mu\mu_B}{\hbar^2\sqrt{2\pi k}}$. It is necessary to note that the two component spinor $\vec{f'}(\varphi)$ relates to the $x' - z'$ coordinate system that is denoted by the sign ($'$).

Now it is convenient first to carry out integration over φ' in (3.3.4) with the help of the known presentations of the Bessel functions:

$$\int_0^{2\pi} e^{-ix\cos\varphi'} d\varphi' = 2\pi J_0(x),$$

$$\int_0^{2\pi} \cos^2\varphi' e^{-ix\cos\varphi'} d\varphi' = \frac{-\partial^2}{\partial x^2}\int_0^{2\pi} e^{-ix\cos\varphi'} d\varphi'$$

$$= -2\pi\frac{\partial^2}{\partial x^2}J_0(x) = 2\pi\frac{J_1(x)}{x} - 2\pi J_2(x).$$

Here $J_0(x)$, $J_1(x)$, and $J_2(x)$ are the first kind of Bessel functions of the zeroth, first, and second order respectively ($x = q\rho'$). The last formula is obtained with the help

of recurrence relation $xJ_n'(x) = nJ_n(x) - xJ_{n+1}(x)$. We also need one more integral

$$\int_0^{2\pi} (\sin\varphi' \cos\varphi') e^{-ix\cos\varphi'} d\varphi' = 0.$$

Employing the obtained results in (3.3.4) together with the recurrence relation $x[J_{n-1}(x) + J_{n+1}(x)] = 2nJ_n(x)$, we find

$$\vec{f}'(\varphi) = \frac{6\gamma\pi}{a}\Big[- I_1 \sin\frac{\varphi}{2} \begin{pmatrix} -\sin\frac{\varphi}{4} \\ \cos\frac{\varphi}{4} \end{pmatrix} + I_2 \cos\frac{\varphi}{2} \begin{pmatrix} \cos\frac{\varphi}{4} \\ \sin\frac{\varphi}{4} \end{pmatrix} \Big], \tag{3.3.5}$$

where

$$I_1 = qa \int_{qa}^{\infty} \frac{1}{x^2} \big[\frac{2}{3} J_0(x) - \frac{1}{x} J_1(x)\big] dx, \tag{3.3.6}$$

$$I_2 = qa \int_{qa}^{\infty} \frac{1}{x^2} \big[\frac{1}{x} J_1(x) - \frac{1}{3} J_0(x)\big] dx. \tag{3.3.7}$$

The dimensionless factor qa in I_1 and I_2 compensates divergence of these integrals at $qa \to$ zero. For detail expressions of I_1 and I_2 see Appendix.

To obtain the spin dependent scattering amplitudes in the original coordinate system, we have to rotate the spinors in (3.3.5) by $-\varphi/2$:

$$\vec{f}(\varphi) = \frac{6\gamma\pi}{a}\Big\{ - I_1 \sin\frac{\varphi}{2} \hat{U}_y(-\frac{\varphi}{4}) \begin{pmatrix} -\sin\frac{\varphi}{4} \\ \cos\frac{\varphi}{4} \end{pmatrix} + I_2 \cos\frac{\varphi}{2} \hat{U}_y(-\frac{\varphi}{4}) \begin{pmatrix} \cos\frac{\varphi}{4} \\ \sin\frac{\varphi}{4} \end{pmatrix} \Big\}.$$

With account of (3.3.3), this gives

$$\begin{vmatrix} f^{\parallel}_{\uparrow\uparrow}(\varphi) \\ f^{\parallel}_{\uparrow\downarrow}(\varphi) \end{vmatrix} = \frac{6\gamma\pi}{a}\Big\{ \big[I_1 \sin^2\frac{\varphi}{2} + I_2 \cos^2\frac{\varphi}{2}\big] \begin{pmatrix} 1 \\ 0 \end{pmatrix} + \frac{1}{2}\big[I_2 - I_1\big] \sin\varphi \begin{pmatrix} 0 \\ 1 \end{pmatrix} \Big\}. \tag{3.3.8}$$

Here we introduce the scattering amplitude with no spin flipping $f^{\parallel}_{\uparrow\uparrow}$ and scattering amplitude with spin flipping $f^{\parallel}_{\uparrow\downarrow}$. After substituting the value of γ the scattering amplitudes (3.3.8) take the form

$$f^{\parallel}_{\uparrow\uparrow} = -\sqrt{L_0}\frac{I_1 \sin^2\frac{\varphi}{2} + I_2 \cos^2\frac{\varphi}{2}}{\sqrt{ka}}, \tag{3.3.9}$$

$$f^{\parallel}_{\uparrow\downarrow} = -\sqrt{L_0}\frac{[I_2 - I_1]\sin\varphi}{2\sqrt{ka}}, \tag{3.3.10}$$

where

$$L_0 = 18\pi a\left(\frac{m\mu\mu_B}{a\hbar^2}\right)^2 \tag{3.3.11}$$

specifies the scattering length with the typical radius a of the nanomagnet.

Now, we consider the scattering of electrons moving along the z-axis with the spins aligned opposite to the magnetic monent $\vec{\mu}$. The spin wave function $\vec{\chi}_{0\downarrow}(S) = \begin{pmatrix} 0 \\ 1 \end{pmatrix}$ in the coordinate system with the z-axis parallel to $\vec{\mu}$. Hence, in the coordinate system $x' - z'$

$$\vec{\chi}_{\downarrow}(S) = \hat{U}_y\vec{\chi}_{0\downarrow}(S) = \begin{pmatrix} \cos\frac{\varphi}{4} & \sin\frac{\varphi}{4} \\ -\sin\frac{\varphi}{4} & \cos\frac{\varphi}{4} \end{pmatrix}\begin{vmatrix} 0 \\ 1 \end{vmatrix} = \begin{pmatrix} \sin\frac{\varphi}{4} \\ \cos\frac{\varphi}{4} \end{pmatrix}.$$

Substituting this spinor and interaction potential (3.3.1) into (3.1.14) and following the same procedure as for the electron spin aligned parallel to magnetic moment $\vec{\mu}$, we find the following relations.

$$f^{\parallel}_{\downarrow\uparrow}(ka,\varphi) = -f^{\parallel}_{\uparrow\downarrow}(ka,\varphi), \tag{3.3.12}$$

$$f^{\parallel}_{\downarrow\downarrow}(ka,\varphi) = f^{\parallel}_{\uparrow\uparrow}(ka,\varphi). \tag{3.3.13}$$

Here, $f^{\parallel}_{\downarrow\uparrow}(\varphi)$ and $f^{\parallel}_{\downarrow\downarrow}(\varphi)$ are the scattering amplitudes with spin flipping and no spin flipping after scattering, respectively. This means that the probability of spin flipping proportional to square of the scattering amplitudes for down state is same as for the up state case.

3.3.2 The magnetic moment $\vec{\mu}$ perpendicular to initial velocity of electrons

In this subsection we consider the case when the magnetic moment $\vec{\mu}$ is transverse to the incident wave. We keep the previous direction for incident wave along z-axis. But now $\vec{\mu}$ is along positive x. The interaction potential (3.3.1) preserves its form. Acting as above and taking in to account that the components of the magnetic moment of the nanoparticle $\mu_{x'} = \mu \cos\frac{\varphi}{2}$ and $\mu_{z'} = \mu \sin\frac{\varphi}{2,}$ we obtain

$$\left| \begin{array}{c} f'^{\perp}_{\uparrow\uparrow}(\varphi) \\ f'^{\perp}_{\uparrow\downarrow}(\varphi) \end{array} \right| = \frac{6\gamma\pi}{a}\left[I_1 \cos\frac{\varphi}{2} \begin{pmatrix} -\sin\frac{\varphi}{4} \\ \cos\frac{\varphi}{4} \end{pmatrix} + I_2 \sin\frac{\varphi}{2} \begin{pmatrix} \cos\frac{\varphi}{2} \\ \sin\frac{\varphi}{4} \end{pmatrix} \right]. \tag{3.3.14}$$

The scattering amplitudes $f'^{\perp}_{\uparrow\uparrow}(\varphi)$ and $f'^{\perp}_{\uparrow\downarrow}(\varphi))$ describe scattering of the electron by the transverse magnetic moment with no spin flipping and spin flipping, respectively. The spinors in (3.3.14) are related to the $x' - z'$ coordinate system. To observe the effect of spin dependent electron scattering amplitudes, we have to rotate the spinors in (3.3.14) back to the original coordinate system $(x - z)$ by $-\varphi/2$ along the y-axis. Doing this rotation and following the same procedure that we have done for the case of magnetic moment parallel to velocity of electron, the scattering amplitudes of electron whose spin is transverse to the magnetic moment $\vec{\mu}$, we obtain

$$f^{\perp}_{\uparrow\uparrow}(ka, \varphi) = f^{\parallel}_{\downarrow\uparrow}(ka, \varphi), \tag{3.3.15}$$

$$f^{\perp}_{\uparrow\downarrow}(ka,\varphi) = -\sqrt{L_0}\frac{I_1\cos^2\frac{\varphi}{2} + I_2\sin^2\frac{\varphi}{2}}{\sqrt{ka}}. \tag{3.3.16}$$

For the electrons with spin antparallel to direction of propagation ($\vec{\chi}_{0\downarrow}(S) = \begin{vmatrix} 0 \\ 1 \end{vmatrix}$ for down state) before scattering and perpendicular to the magnetic moment $\vec{\mu}$, we get

$$f^{\perp}_{\downarrow\downarrow}(ka,\varphi) = -f^{\perp}_{\uparrow\uparrow}(ka,\varphi), \tag{3.3.17}$$

$$f^{\perp}_{\downarrow\uparrow}(ka,\varphi) = f^{\perp}_{\uparrow\downarrow}(ka,\varphi). \tag{3.3.18}$$

In 2D spin independent scattering problem, the measurable quantities are the differential scattering lengths $dL(k,\varphi) = |f(k,\varphi)|^2 d\varphi$ (function of the energy of incident particle and the scattering angle φ) and the total scattering length $L = \int |f(k,\varphi)|^2 d\varphi$. Moreover, in 2D spin dependent scattering problem, the scattering amplitudes are two component spinors, which describe the processes with different orientation of spins after scattering and in general case depend on a mutual orientation of spin of scattering electrons and the magnetic moment of nano-particle. In this paper, we consider only two spin orientation $\parallel$ and $\perp$ to $\vec{\mu}$. In the next section, we analyze the scattering lengths of the considered processes and discuss their peculiarities for typical cases of 2D spin dependent electron scattering by gigantic nanomagnets.

3.4 Numerical and graphical analysis of scattering lengths

Comparison of scattering amplitudes (3.3.9-3.3.10), (3.3.12-3.3.13); (3.3.15-3.3.18), results in the following equalities

$$|f^{\parallel}_{\uparrow\uparrow}|^2 = |f^{\parallel}_{\downarrow\downarrow}|^2, \tag{3.4.1}$$

$$|f^{\perp}_{\uparrow\downarrow}|^2 = |f^{\perp}_{\downarrow\uparrow}|^2, \tag{3.4.2}$$

$$|f^{\parallel}_{\uparrow\downarrow}|^2 = |f^{\parallel}_{\downarrow\uparrow}|^2 = |f^{\perp}_{\uparrow\uparrow}|^2 = |f^{\perp}_{\downarrow\downarrow}|^2. \tag{3.4.3}$$

These relations simplify the further analysis.

As in 3D scattering theory [60], we can made general conclusions concerning the scattering amplitudes in the limit of slow particles ($ka \ll 1$) and fast particles ($ka \gg 1$). In the first case, $I_1 = I_2 = 1/6$. This can be checked straight forward using the definitions of I_1 and I_2 (see Appendixes). With this in mind, we get

$$|f^{\parallel}_{\uparrow\uparrow}|^2 = f|^{\parallel}_{\downarrow\downarrow}|^2 = |f^{\perp}_{\uparrow\downarrow}|^2 = |f^{\perp}_{\downarrow\uparrow}|^2 = \frac{L_0}{36ka}, \tag{3.4.4}$$

$$|f^{\parallel}_{\uparrow\downarrow}|^2 = |f^{\parallel}_{\downarrow\uparrow}|^2 = |f^{\perp}_{\uparrow\uparrow}|^2 = |f^{\perp}_{\downarrow\downarrow}|^2 = 0. \tag{3.4.5}$$

The total scattering lengths of slow particles for the process denoted by (3.4.4) is obtained by integration over all φ and equals

$$L(ka) = \frac{\pi L_0}{18ka}. \tag{3.4.6}$$

From (3.4.4) one can see that the spin dependent electron scattering is isotropic for slow particles ($ka \ll 1$). Relation (3.4.5) shows the probability of scattering with spin

flipping by the magnetic moment parallel to the velocity of electron and the scattering with no spin flipping by the transversal magnetic moment are close to zero.

For the fast particles ($ka >> 1$), the exponent in (3.1.14) is fast oscillating and the result of integration is nonzero only for small scattering angles ($2ka \sin\frac{\varphi}{2} \sim 1$ or $\varphi \sim 1/ka \ll 1$). The scattering length is very small in this case because it suppressed by a large factor $ka \gg 1$. These conclusions are in agreement with the general scattering theory [60] and our numerical calculations given below.

Equalities (3.4.1)-(3.4.3) allow us to inroduce three normalised dimenssionless scattering lengths

$$\widetilde{L}_1 = \frac{1}{L_0}\frac{dL_1}{d\varphi} = \frac{1}{ka}[I_1 \sin^2\frac{\varphi}{2} + I_2 \cos^2\frac{\varphi}{2}]^2, \tag{3.4.7}$$

$$\widetilde{L}_2 = \frac{1}{L_0}\frac{dL_2}{d\varphi} = \frac{1}{ka}[I_1 \cos^2\frac{\varphi}{2} + I_2 \sin^2\frac{\varphi}{2}]^2, \tag{3.4.8}$$

$$\widetilde{L}_3 = \frac{1}{L_0}\frac{dL_3}{d\varphi} = \frac{1}{4ka}[I_1 - I_2]^2 \sin^2\varphi. \tag{3.4.9}$$

Analytical expressions of I_1 and I_2 as functions of ka and φ are given in the Appendix. The dimensionless scattering length $\widetilde{L}_1$ relates to the scattering with no spin flipping of electrons with initial velocity parallel to magnetic moment of nanoparticle $\vec{\mu}$ and $\widetilde{L}_2$ relates to the scattering with spin flipping of electrons with initial velocity of electrons perpendicular to the magnetic moment of nanoparticle $\vec{\mu}$. The quantity $\widetilde{L}_3$ relates to the scattering with spin flipping when initial velocity of electrons is parallel to the magnetic moment of nanoparticle $\vec{\mu}$ and scattering of electrons with no spin flipping when the initial electrons velocity is perpendicular to the magnetic moment of nanoparticle $\vec{\mu}$. Formulae (A5), (A6), and (A7) show all these functions are periodical with a period of 2π. This means that for small angles in the vicinity of $\varphi = 0$ and

of $\varphi = 2\pi$ correspond to the forward scattering. The small angles in the vicinity of $\varphi = \pi$ correspond to the back scattering.

Figures 3.2 (a-c) present 3D graphs of $\widetilde{L}_1$, $\widetilde{L}_2$, and $\widetilde{L}_3$ as functions of ka and φ built with the help of formulas $(A5)$, $(A6)$, and $(A7)$ in the range of ka where the spin dependent scattering is anisotropic. Our numerical calculations allow us to specify more precisely the range of ka where the scattering becomes anistotropic. In particular, for $ka \approx 0.1$ the scattering shows anisotropy. At $ka \approx 5$ the scattering length is practically zero.

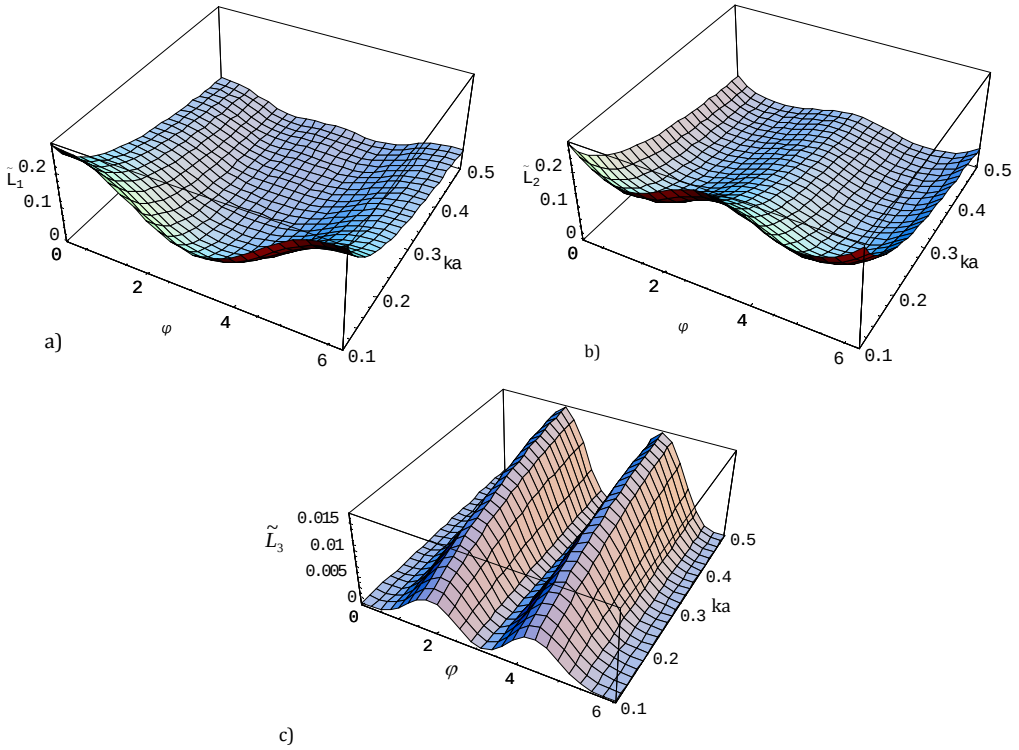

Figure 3.2: The dimensionless differential scattering length $\widetilde{L}_1$ (a), $\widetilde{L}_2$ (b), and $\widetilde{L}_3$ (c) versus ka and φ (in radians). The graphs clearly show anisotropy of the scattering with respect to the scattering angle φ.

An inspection of graphs (Fig. 3.2 (a-c)) show that $\widetilde{L}_1$ and $\widetilde{L}_2$ have maxima of the same order, but $\widetilde{L}_3$ have maxima of one order smaller than $\widetilde{L}_1$ and $\widetilde{L}_2$ for $ka = 0.2$. The cross sections of these graphs by a plane $ka = constant$ give dependencies of $\widetilde{L}_i (i = 1, 2, 3)$ on φ.

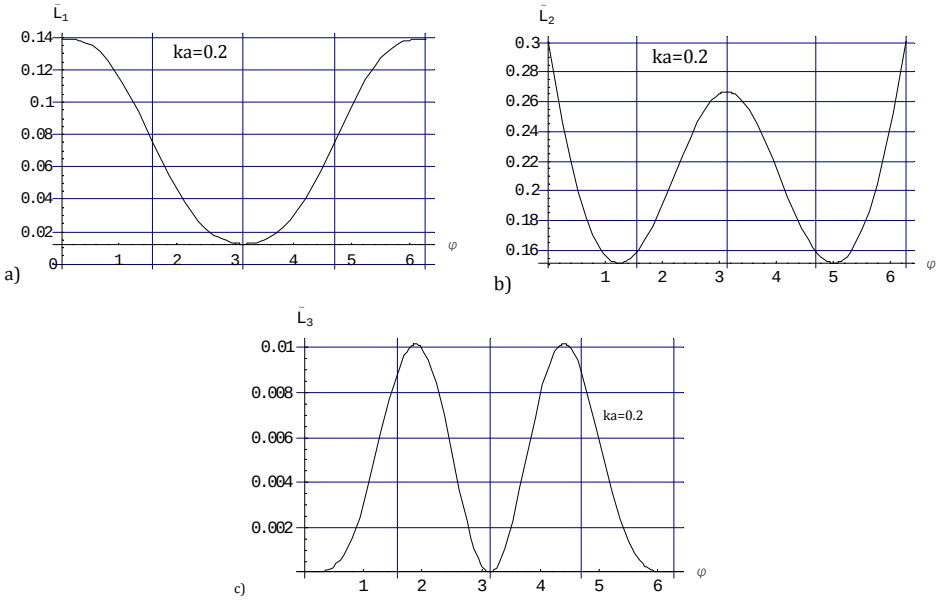

Figure 3.3: The dimensionless differential scattering length $\widetilde{L}_1$ (a), $\widetilde{L}_2$ (b), and $\widetilde{L}_3$ (c) versus φ for $ka = 0.2$.

Figures 3.3 (a-c) show the differential scattering lengths as functions of φ at $ka = 0.2$. In this case, the wave length of incident electrons considerably exceeds the size of nanomagnets, $\lambda = 10\pi a \gg a$. With the help of these graphs one can evaluate a number of particles scattered with an angle φ in the small interval $\delta\varphi$ in the vicinity of this angle. It is proportional to $\widetilde{L}_i(\varphi)\delta\varphi$. For example, from Fig. 3.3 (a) one can see that a number of scattered electrons with no spin flipping is the largest for small scattering angles. From Fig. 3.3 (b) follows that the scattering with spin flipping is

the largest in the vicinity of small angles as well. In the vicinity of $\varphi = \pi$, the graph of Fig. 3.3 (b) shows the second maxima. It corresponds to the backward scattering with spin flipping. The probability of this scattering is smaller than the probability of the forward scattering. Such a maximum appears for $\widetilde{L}_1$ at $\varphi \sim \ 3rad$ and $ka = 0.5$. But it is five times smaller than the probability of forward scattering. Figure 3.3 (c) relates to the scattering with spin flipping for the initial velocity of electrons parallel to $\vec{\mu}$. For the initial velocity of electrons is perpendicular to $\vec{\mu}$, it describes the non spin flipping scattering. The position of maxima of graph Fig. 3.3 (b) corresponds to the position of minima of Fig. 3.3 (c). The maxima of $\widetilde{L}_3$ located near $\varphi = \pi/2$ and $\varphi = 3\pi/2$. For example, the scattered electrons with flipped spin initially moving along $\vec{\mu}$ are concentrated in the direction transversal to their initial velocity. The scattered electrons with their spin flipped and initially moving perpendicular to $\vec{\mu}$ are concentrated at small scattering angles.

This feature of $2D$ spin dependent electron scattering by the nanomagnet allows performing experiments on separation of electrons with different orientation of spins. In particular, launching a polarized beam of electrons (spins along the velocity) with $ka = 0.2$ along the magnetic moment of a nanoparticle ($a \approx 10nm$), we have electrons with non flipped spins and electrons with spin flipped. It is possible to compare numbers of these electrons by using the formula $(\widetilde{L}_3(\pi/2)\delta\varphi)/(\widetilde{L}_1(0)\delta\varphi)$. According to graphs 3.3 (a) and 3.3 (c), we obtain that this ratio close to 1/13. From the other hand, launching a polarized beam of electrons with the same ka perpendicular to the magnetic moment of the nanoparticle ($a \approx 10nm$), we can see from graphs 3.3 (b) and 3.3 (c) that the ratio $(\widetilde{L}_2(0))/(\widetilde{L}_3(\pi/2)) \sim 15$. These examples illustrate anisotropy spin dependent scattering of electrons by nanomagnets.

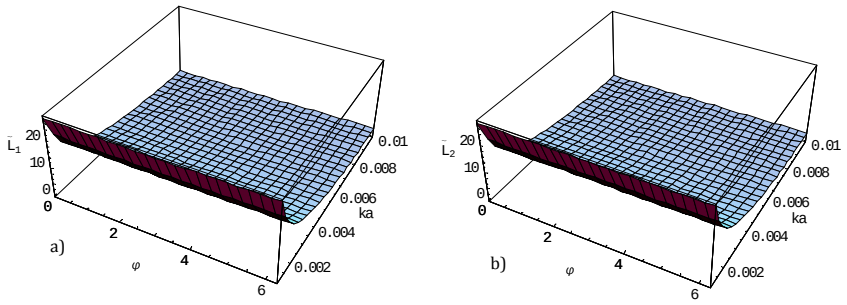

Figure 3.4: The dimensionless differential scattering length $\widetilde{L}_1$ (a), and $\widetilde{L}_2$ (b), versus φ for $ka = 0.001$ to 0.1.

Figures 3.4 (a) and (b) depict the dimensionless differential scattering lengths $\widetilde{L}_1$ and $\widetilde{L}_2$ for small value of ka ($ka \ll 1$), respectively. As we explained above, the scattering processes for very slow electrons are isotropic, which can be seen from Fig. 3.4.

To show the range of effective scattering, we present Fig. 3.5. The graph is drawn for $0.001 \leq ka \leq 2$. In the range of $0.001 \leq ka \leq 0.1$, the scattering is isotropic and in the range of $0.1 \leq ka \leq 0.5$, the scattering is anisotropic and for large value of ka it goes to zero. The direct observation of Figures 3.4 and 3.5 indicate that the values of I_1 and I_2 are the same for very slow electrons. This is because from Fig. 3.4 (a) and (b) we have the same value of the scattering lengths in small ka regions and from Fig. 3.5 we have zero dimensionless scattering length $\tilde{L}_3$, which depends on the difference of I_1 and I_2.

It would be interesting to compare the parameter L_0, which specifies the scattering length with the typical radius a of the nanomagnet. The quantity L_0 (see its definition (3.3.11) and inequality (3.2.1)) can be presented in the form

$$\frac{L_0}{a} \simeq 10^3 \nu^2 \left(\frac{m\mu_B^2 n_a a^2}{\hbar^2} \right)^2, \tag{3.4.10}$$

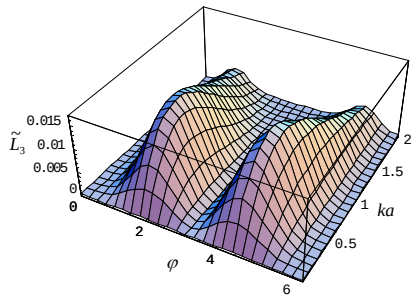

Figure 3.5: The dimensionless differential scattering length $\widetilde{L}_3$ versus φ for $ka = 0.001$ to 2.

The dimensionless combinations L_0/a basically determines the scale of spin dependent scattering. Comparing (3.4.10) with the criterion of applicability of the Born approximation (3.2.1), we obtain the following constraint $L_0/a < 4$. It shows that L_0/a is always small regardless of the values of the parameters of 2D spin dependent electron scattering. To our mind it is a manifestation of the short range character of the dipole-dipole interaction in the 2D geometry. According to (3.4.10), taking $\nu = 10$ that is in agreement with references [122-128], we obtain $L_0/a = 0.1$ for $a \approx 10nm$,which is in agreement with $L_0/a < 4$.

3.5 Conclusions

We considered the 2D scattering of electrons by a nanomagnet when the electron momentum and the magnetic moment $\vec{\mu}$ of the nanoparticle are in the same plane. Considering the dipole-dipole interaction of the magnetic moments, we solved the problem in the Born approximation. The interaction potential is not spherically symmetric and depends on the electron spin and orientation of $\vec{\mu}$. It considerably

complicates the calculations of the scattering lengths that become two-component spinors.

We obtained the scattering lengths for the electrons with energies parameter $ka = 0.2 - 0.5$ with the same orientation of spins scattered by a gigantic nanomagnet ($\vec{\mu}$ is parallel or perpendicular to the velocity of incident electrons). It is shown that the scattering lengths for the spin flipping and non spin flipping processes have rather sharp maxima as functions of the scattering angle. The forward and backward scattered electrons preserve the initial direction of spin for the case when the initial velocity of electrons are parallel to magnetic moment of nanoparticle $\vec{\mu}$. This property of the spin dependent scattering allows one to separate electrons with different orientation of spin and compare their numbers. The electrons scattered by angles $\pi/2$ and $3\pi/2$ are oppositely directed beams. This can be used as one more method of controlling of the electron currents with different spin orientation.

The above described picture relates to the scattering of electrons by a single scattering center. These effects can be increased if we consider the scattering of electrons by a chain of scattering centers provided that the wave length of the incident electrons is smaller than the average distance between the nanomagnets. It is clear that every subsequent scattering will independently contribute to the relevant scattering length.

Chapter 4

2D Spin-Dependent Scattering of Unpolarized Beams of Electrons by Neutral Nanomagnets

4.1 Scattering lengths of unpolarized beams of electrons scattered by neutral nanomagnets

In section 3.1 we have derived the scattering amplitude equation (3.1.14) for polarized electron beams scattered from neutral nanomagnets. We use this equation for unpolarized beams of electrons by modifying the spinor part of the equation. That is

$$\vec{f}(\varphi) = -\frac{m}{\hbar^2\sqrt{2\pi k}} \int e^{-i\vec{q}\cdot\vec{\rho'}} \hat{V}(\vec{\rho'}) \rho' d\rho' d\varphi \vec{\chi}_0(S). \tag{4.1.1}$$

The spin function of incident electron is chosen in the form

$$\vec{\chi}_0(S) = \alpha \begin{vmatrix} 1 \\ 0 \end{vmatrix} + \beta \begin{vmatrix} 0 \\ 1 \end{vmatrix} \tag{4.1.2}$$

with $\alpha^2 + \beta^2 = 1$, α^2, β^2 are the fractions of electrons whose spin are parallel and antiparallel to their initial velocity (along z-axis), respectively.

In Chapter 3, we considered the spin-dependent electron scattering by a neutral nanomagnet for polarized beams and discussed the validity of the Born approximation. As a result, we obtained that the Born approximation can be applied to neutral nanomagnets with a radius $a < 100/\sqrt{\nu}\ nm$. This condition of Born approximation is also valid for unpolarized beams of electron scattered from neutral nanomagnets. In the next section, we use (4.1.1) to calculate the scattering amplitudes of electrons by neutral nanomagnets for unpolarized beams.

4.1.1 The magnetic moment $\vec{\mu}$ parallel to initial velocity of electrons

Firstly, we consider the scattering of electrons coming with velocity $\vec{v}$ from infinity parallel to the z-axis by a nanomagnet with a magnetic moment $\vec{\mu}$ oriented along the z-axis. Just as discussed in previous chapter, the nanomagnet is modeled by a spherical particle of radius a possessing the magnetic moment $\vec{\mu}$.

The scattering amplitudes resulted from the spin-dependent scattering potential (3.1.6) for unpolarized beams is given by the following expression

$$\vec{f}'(\varphi) = -\frac{m}{\hbar^2\sqrt{2\pi k}}\int_0^{2\pi}\int_a^{\infty} e^{-i\vec{q}\cdot\vec{\rho}'}\frac{\mu_B}{\rho'^3}\big(3(\vec{\mu}\cdot\vec{n})\vec{n}\cdot\hat{\sigma} - \vec{\mu}\cdot\hat{\sigma}\big)\rho' d\rho'\varphi'\vec{\chi}_0(S). \qquad (4.1.3)$$

Here, again to evaluate the integral (4.1.3) one has to choose appropriate coordinate system as shown in Fig. 3.1. The operator of potential energy (3.1.6) in (x', z') coordinate system takes the same form as (3.3.1)

$$\hat{V} = \frac{\mu_B}{\rho'^3}\left\{\left[\mu_{x'}\big(3\cos^2\varphi' - 1\big) + \frac{3}{2}\mu_{z'}\sin 2\varphi'\right]\hat{\sigma}_{x'} + \left[\mu_{z'}\big(3\sin^2\varphi' - 1\big) + \frac{3}{2}\mu_{x'}\sin 2\varphi'\right]\hat{\sigma}_{z'}\right\}. \qquad (4.1.4)$$

It is necessary to remember that integration in the coordinate system (x', z') requires transformation of the spinor wave function $\vec{\chi}_0(S)$ to this coordinate system. Substituting equation (4.1.4) into (4.1.3), performing integrations with respect to φ' and ρ' and finally rotating back to the unprimed coordinate system, we get

$$\vec{f}(\varphi) = f_{\uparrow}^{\parallel}(\varphi) \begin{pmatrix} 1 \\ 0 \end{pmatrix} + f_{\downarrow}^{\parallel}(\varphi) \begin{pmatrix} 0 \\ 1 \end{pmatrix}, \tag{4.1.5}$$

where

$$f_{\uparrow}^{\parallel}(\varphi) = \frac{6\gamma\pi}{a}\big[\alpha(I_1 \sin^2\frac{\varphi}{2} + I_2 \cos^2\frac{\varphi}{2}) + \frac{\beta}{2}\big(I_2 - I_1\big)\sin\varphi\big], \tag{4.1.6}$$

$$f_{\downarrow}^{\parallel}(\varphi) = \frac{6\gamma\pi}{a}\big[-\beta(I_1 \sin^2\frac{\varphi}{2} + I_2 \cos^2\frac{\varphi}{2}) + \frac{\alpha}{2}\big(I_2 - I_1\big)\sin\varphi\big]. \tag{4.1.7}$$

Here, I_1 and I_2 are given by equations (3.3.6) and (3.3.7), respectively. The superscript $\parallel$ denotes that the incident electron beams are parallel to $\vec{\mu}$, the arrows specify direction of the electron spin after scattering.

The total scattering amplitude can be represented as the following two component spinor

$$\vec{f}^{\parallel}(\varphi) = \begin{vmatrix} f_{\uparrow}^{\parallel}(\varphi) \\ f_{\downarrow}^{\parallel}(\varphi) \end{vmatrix}. \tag{4.1.8}$$

The first component of the spinor is the scattering amplitude of electrons having spin along z-axis (spin up) and the second component is the electrons scattering amplitude with spin down. The scattering amplitudes in (4.1.8) can be written as

$$f_{\uparrow}^{\parallel}(ka, \varphi) = \sqrt{L_0}\Big[\alpha\sqrt{\tilde{L}_1} + \beta\sqrt{\tilde{L}_3}\Big], \tag{4.1.9}$$

$$f_{\downarrow}^{\parallel}(ka, \varphi) = \sqrt{L_0}\Big[-\beta\sqrt{\tilde{L}_1} + \alpha\sqrt{\tilde{L}_3}\Big]. \tag{4.1.10}$$

The expressions of L_0, $\tilde{L}_1$, and $\tilde{L}_3$ are given by equations (3.3.11), (3.4.7), and (3.4.9), respectively.

The differential scattering lengths when $\vec{v}$ of incident beam of electrons are parallel to $\vec{\mu}$ of nanomagnets can be written as

$$|f_{\uparrow}^{\parallel}(ka,\varphi)|^2 = L_0\left[\alpha\sqrt{\tilde{L}_1} + \beta\sqrt{\tilde{L}_3}\right]^2, \tag{4.1.11}$$

$$|f_{\downarrow}^{\parallel}(ka,\varphi)|^2 = L_0\left[-\beta\sqrt{\tilde{L}_1} + \alpha\sqrt{\tilde{L}_3}\right]^2. \tag{4.1.12}$$

The scattering lengths (4.1.11) and (4.1.12) symmetrically depend on the spin polarization of the incident beam of electrons α and β. The general property of these lengths are discussed below in Section 4.2.

4.1.2 The magnetic moment $\vec{\mu}$ perpendicular to initial velocity of electrons

Now we consider the case when the magnetic moment $\vec{\mu}$ is transverse to z-axis. We keep the previous direction for velocity $\vec{v}$ of electrons along the z-axis. Let $\vec{\mu}$ be along positive x-axis. The interaction potential (3.1.6) preserves its form. Acting as above and following the same procedures as in section 3.3, we obtain the spin dependent scattering amplitudes

$$\vec{f}^{\perp}(\varphi) = \begin{vmatrix} f_{\uparrow}^{\perp}(\varphi) \\ f_{\downarrow}^{\perp}(\varphi) \end{vmatrix}, \tag{4.1.13}$$

where $f_{\uparrow}^{\perp}(\varphi)$ and $f_{\downarrow}^{\perp}(\varphi)$ represent the spin dependent 2D scattering amplitudes of electron with initial velocity perpendicular ($\perp$) to $\vec{\mu}$ with the spin up and down after

scattering, respectively. The scattering amplitudes $f_{\uparrow}^{\perp}(\varphi)$ and $f_{\downarrow}^{\perp}(\varphi)$ can be presented as

$$f_{\uparrow}^{\perp}(ka,\varphi) = \sqrt{L_0}\left[\beta\sqrt{\tilde{L}_2} + \alpha\sqrt{\tilde{L}_3}\right], \tag{4.1.14}$$

$$f_{\downarrow}^{\perp}(ka,\varphi) = \sqrt{L_0}\left[\alpha\sqrt{\tilde{L}_2} - \beta\sqrt{\tilde{L}_3}\right], \tag{4.1.15}$$

where we used equations (3.1.11), (3.4.8) and (3.4.9).

The differential scattering lengths in this case can be presented as

$$|f_{\uparrow}^{\perp}(ka,\varphi)|^2 = L_0\left[\beta\sqrt{\tilde{L}_2} + \alpha\sqrt{\tilde{L}_3}\right]^2, \tag{4.1.16}$$

$$|f_{\downarrow}^{\perp}(ka,\varphi)|^2 = L_0\left[\alpha\sqrt{\tilde{L}_2} - \beta\sqrt{\tilde{L}_3}\right]^2. \tag{4.1.17}$$

In next section, we discuss the general properties of the differential scattering lengths (4.1.11, 4.1.12) and (4.1.16, 4.1.17) as functions of the scattering angle φ and the dimensionless parameter ka, which characterizes the energy of incident electrons for the unpolarized beams of electrons $\alpha = \beta = 1/\sqrt{2}$.

4.2 Numerical and graphical analysis of scattering lengths

In Chapter 3, we studied the scattering of the polarized electron beams by neutral nanomagnets. The above obtained formulas allow us to clarify the peculiarities of the scattering of unpolarized beams of electrons. Consider the scattering of electrons initially moving parallel to $\vec{\mu}$ (equations (4.1.11) and (4.1.12)) and perpendicular to

$\vec{\mu}$ (equations (4.1.16) and (4.1.17)). Below, we present the graphs of the following dimensionless differential scattering lengths

$$\tilde{L}^{\parallel}_{\uparrow} = \frac{1}{L_0}\frac{dL^{\parallel}_{\uparrow}}{d\varphi} = \frac{1}{L_0}\big[f^{\parallel}_{\uparrow}(ka,\varphi)\big]^2, \tag{4.2.1}$$

$$\tilde{L}^{\parallel}_{\downarrow} = \frac{1}{L_0}\frac{dL^{\parallel}_{\downarrow}}{d\varphi} = \frac{1}{L_0}\big[f^{\parallel}_{\downarrow}(ka,\varphi)\big]^2, \tag{4.2.2}$$

$$\tilde{L}^{\perp}_{\uparrow} = \frac{1}{L_0}\frac{dL^{\perp}_{\uparrow}}{d\varphi} = \frac{1}{L_0}\big[f^{\perp}_{\uparrow}(ka,\varphi)\big]^2, \tag{4.2.3}$$

$$\tilde{L}^{\perp}_{\downarrow} = \frac{1}{L_0}\frac{dL^{\perp}_{\downarrow}}{d\varphi} = \frac{1}{L_0}\big[f^{\perp}_{\downarrow}(ka,\varphi)\big]^2. \tag{4.2.4}$$

In Chapter 3, we obtained that 2D spin dependent scattering of polarized beams of electrons is practically isotropic for very slow particles $ka \ll 1$. It is true for the scattering of unpolarized beams of slow electrons as well. Firstly, we consider the scattering of electrons with an initial velocity $\vec{v}$ parallel to $\vec{\mu}$.

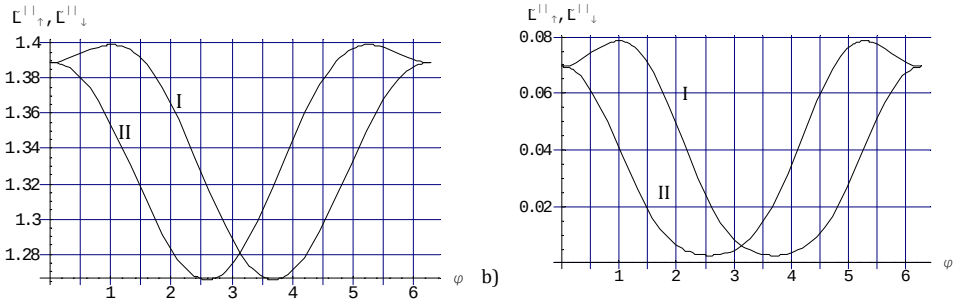

Figure 4.1: $\tilde{L}^{\parallel}_{\uparrow}$ (curve I) and $\tilde{L}^{\parallel}_{\downarrow}$ (curve II) versus φ, (a) for $ka = 0.01$, and (b) for $ka = 0.2$, according to equations (4.2.1) and (4.2.2).

Figure 4.1 (a) shows the scattering lengths for spin up (curve I) and spin down (curve

II). The maximum difference between these scattering lengths is 8% for $\varphi = 2$ rad. It allows us to claim that the scattering is weakly anisotropic. With increasing ka, the scattering becomes anisotropic. The ratio of numbers of the scattered electrons with spin up and spin down depends on φ. Figure 4.1 (b) shows the scattering lengths for $ka = 0.2$. At $\varphi \simeq \pi/2$ the ratio of $\tilde{L}^{\parallel}_{\uparrow}$ to $\tilde{L}^{\parallel}_{\uparrow}$ is about 4. This means that around the scattering angle $\varphi = \pi/2$, 80% of the scattered electrons have spin up and 20% spin down. Unfortunately, the values of the corresponding scattering lengths are very small. The scattering by charged nanomagnets may enhance these lengths. We may note that in nuclear physics the scattering by the Coulomb and short range potentials allows to study the details of the short range potentials [133].

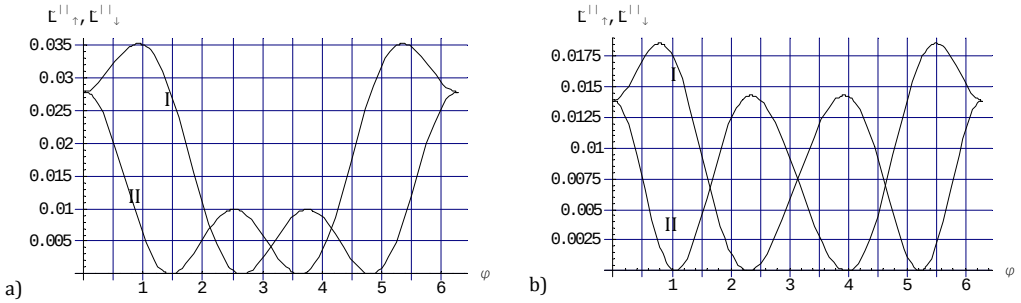

Figure 4.2: $\tilde{L}^{\parallel}_{\uparrow}$ (curve I) and $\tilde{L}^{\parallel}_{\downarrow}$ (curve II) versus φ, (a) for $ka = 0.5$, and (b) for $ka = 1$ according to equations (4.2.1) and (4.2.2).

Figures 4.2 (a) and (b) illustrate the scattering of unpolarized beams of electrons from neutral nanomagnets for $ka = 0.5$ and $ka = 1$, respectively. As one can see from these graphs the scattering lengths became smaller as the energy of the incident electron increases. However, the probability of polarizing the beams considerably increases and for particular values of φ one can get 100% polarization. From Fig. 4.2 (a), one can see that around $\varphi = \pi/2$ all electrons spin point up and around $\varphi = 3\pi/2$ all

electrons spin point down. The complete spin polarization can be also seen from Fig. 4.2 (b) at $\varphi = 1$ and $\varphi = 4$ rad, which shows all spin point up and at $\varphi = 2.3$ and $\varphi = 5.3$ rad, all spins point down. The other feature of these graphs is that as the energy of the incoming beams doubled the scattering lengths reduced by half.

Now, we consider the peculiarities of scattering of unpolarized beams of electrons with initial velocity perpendicular to $\vec{\mu}$. Figures 4.3 (a) and (b) present the corresponding scattering lengths of electrons for $ka = 0.01$ and $ka = 0.2$, respectively. It can be seen that the properties of these scattering are practically the same comparing to the above described. In particular, the ratio of the scattering lengths for electrons with spin up and spin down around $\varphi = \pi/2$ is close to 4 for $ka = 0.2$.

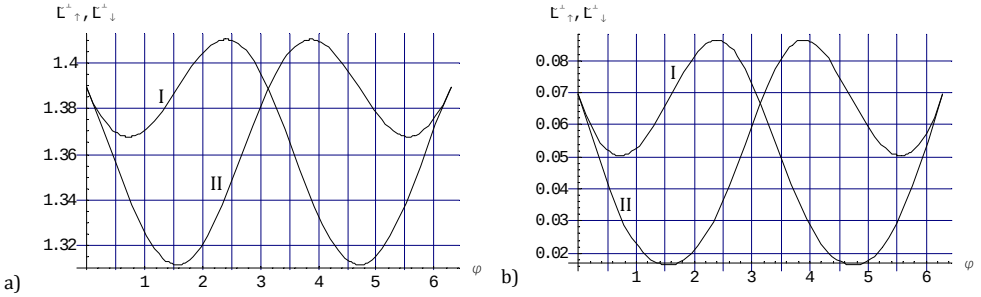

Figure 4.3: $\tilde{L}^{\perp}_{\uparrow}$ (curve I) and $\tilde{L}^{\perp}_{\downarrow}$ (curve II) versus φ, (a) for $ka = 0.01$, and (b) for $ka = 0.2$, according to equations (4.2.3) and (4.2.4).

Figures 4.4 (a) and (b) show the dimensionless scattering lengths $\tilde{L}^{\perp}_{\uparrow}$ (curve I) and $\tilde{L}^{\perp}_{\downarrow}$ (curve II) versus φ, respectively. Just as the case of $\vec{\mu}$ parallel to $\vec{v}$, here also we have complete spin polarization of the beams for particular values of φ. Particularly, for $ka = 0.5$ around $\varphi = 1$ and 2 rad, all scattered electrons spin point up and around $\varphi = 4.3$ and 5.3 rad, point down. From Fig. 4.4(b) all spin of electrons point up around $\varphi = 0.5$ and 2.5 rad, and point down for scattering angle $\varphi = 3.8$ and 5.8 rad.

Here also the dimensionless differential scattering lengths reduced by half as initial electrons beam energy doubled.

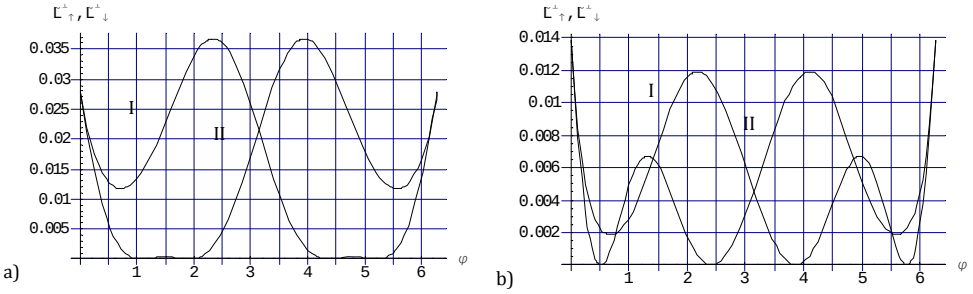

Figure 4.4: $\tilde{L}^{\perp}_{\uparrow}$ (curve I) and $\tilde{L}^{\perp}_{\downarrow}$ (curve II) versus φ, (a) for $ka = 0.5$, and (b) for $ka = 1$ according to equations (4.2.3) and (4.2.4).

4.3 Conclusions

In this Chapter we studied spin-dependent scattering of unpolarized beams of electrons from neutral nanomagnets. The obtained results show that the possibility of completely polarizing beams of electron that were initially unpolarized for certain values of scattering angles. The scattering lengths obtained for both electrons initial velocity parallel and transverse to the magnetic moment of the nanomagnets are relatively small in comparison with the scattering lengths obtained for spin dependent electron scattering by neutral nanomagnets of polarized beam as discussed in Chapter 3. The complete polarization occurs for $ka = 0.5$ and $ka = 1$ or for values of ka in this rage. The corresponding scattering lengths are smaller than those of $ka = 0.2$. As we doubled the energy of electron, the scattering lengths reduced by half and the scattering angle at which complete polarization of beams of electron found shifted to

left (to small angle).

From the obatined results, we can claim that this method can be used as one method of separating electrons spin. The obtained small scattering lengths may be enhanced by using array of scatterer and also by using charged nanomagnets.

Chapter 5

2D Spin-Dependent Scattering of Unpolarized Beams of Electrons by Charged Nanomagnets

Development of different methods of manipulating and detecting the spin-polarized currents became of great interest because of requirements of spintronics [4,7]. It is known that usage of the spin-orbit interaction is one of the possible ways of controlling the spin-polarized currents [134]. This theoretical approach is based on the Rashba or Dresselhaus Hamiltonian [64, 65, 68]. In general case the spin-orbit interaction is comparatively small, which results in weak spin polarized currents.

One more possible mechanism of controlling the spin-polarized currents is the spin-dependent scattering by the nanomagnets with large magnetic moments when the scattering is controlled by the interaction of the magnetic dipole moments of the electron and the nanomagnet. The scattering of polarized electron beams in 2D geometry have been studied in Chapter 3 and 4 and revealed the angular anisotropy of the scattered electrons depending on the spin orientation. Because of the smallness of magnetic interactions the scattering lengths are happened to be rather small. In this Chapter we study the peculiarities of 2D scattering of unpolarized beams of

electrons by charged nanomagnets. It is shown that the Coulomb interaction enhances anisotropy of spin dependent scattering and enhances the corresponding scattering lengths, and can considerably the polarization of incident electrons beams.

5.1 Screening of Coulomb potential in 2DEG

The screening potential in 2D geometry is different from the usual form of 3D geometry. The difference between these geometry results in different scattering processes. The scattering of electrons in 2D geometry was discussed in details for neutral nanomagnets in Chapters 3 and 4 for polarized and unpolarized electrons beams. We haven been also developed the spin-dependent scattering potential. Now we add the Coulomb potential term to the spin-dependent potential to observe the influence of charged nanomagnets on the scattering process. In the case under consideration the scattering potential of the problem $\hat{V}(\vec{\rho})$ consists of two terms

$$\hat{V}(\vec{\rho}) = V_C(\vec{\rho}) + \hat{V}_S(\vec{\rho}), \tag{5.1.1}$$

where $V_C(\vec{\rho})$ is the Coulomb potential of the charged nanomagnet and

$$\hat{V}_S(\vec{\rho}) = \frac{\mu_B}{\rho^3}\left(3(\vec{\mu}\cdot\vec{n})\vec{n}\cdot\hat{\sigma} - \vec{\mu}\cdot\hat{\sigma}\right) \tag{5.1.2}$$

is the interaction of magnetic moments of the nanomagnet $\vec{\mu}$ and the magnetic moment of the electron equal to the Bohr magneton $\mu_B = e\hbar/(2m_e c)$, $\hat{\sigma}$ denotes the Pauli matrices, $\vec{n}$ is a unit vector along the radius vector $\vec{\rho}$.

The 2D electron gas (2DEG) screens the Coulomb potential of scattering center. The analytic expression of the 2D screened Coulomb potential of a point-like charge Ze

is different from the 3D case and given by the integral [135-138]

$$V_C(\vec{\rho}) = \frac{Ze^2}{\epsilon}\int_0^\infty dq\left(\frac{q}{q+q_s}J_0(q\rho)\right), \tag{5.1.3}$$

where e is the electron charge, ϵ is a static dielectric constant, q_s is the 2D screened wave number, q is the wave number, and $J_0(q\rho)$ is the first kind zeroth order of Bessel function. Integration of equation (5.1.3) yields the known result

$$V_C(\vec{\rho}) = \frac{Ze^2}{\epsilon}\left[\frac{1}{\rho} - q_s\frac{\pi}{2}[H_0(q_s\rho) - Y_0(q_s\rho)]\right]. \tag{5.1.4}$$

Here, $H_0(q_s\rho)$ and $Y_0(q_s\rho)$ are the zeroth order the Struve and Neumann functions, respectively. The asymptotic expressions of (5.1.4) are $V_C(\rho) \sim \rho^{-1}$, $q_s\rho \ll 1$ and $V_C(\rho) \sim \rho^{-3}$, $q_s\rho \gg 1$ [136-137].

In 2D scattering process, the amplitude of the cylindrical scattered wave in the Born approximation is given by

$$\vec{f}(\varphi) = -\frac{m^*}{\hbar^2\sqrt{2\pi k}}\int e^{-i\vec{q}\cdot\vec{\rho'}}\left[V_C(\vec{\rho'}) + \hat{V}_S(\vec{\rho'})\right]\rho' d\rho' d\varphi \vec{\chi}_0(S), \tag{5.1.5}$$

where m^* is the effective mass of electron, $\vec{q} = \vec{k} - \vec{k}_0$, $k_0^2 = k^2 = \frac{2m^*E}{\hbar^2}$, $q = 2k_0\sin\frac{\varphi}{2}$ is the transferred momentum (here we consider the elastic collisions), φ is the scattering angle. The spin function of incident electron is given by equation (4.1.2).

For the spin independent scattering $\hat{V}$ reduces to the Coulomb part only. In this case, (5.1.5) coincides with the known formula for 2D scattering in Born approximation [60, 133]. In Chapter 3, we considered the spin-dependent scattering by a neutral nanomagnet and discussed the validity of the Born approximation. As a result we obtained that the Born approximation can be applied to neutral nanomagnets with a radius $a < 100/\sqrt{\nu}\ nm$. The presence of the Coulomb potential implies that additional constrain on a through dimensionless combination $q_s a$ for applicability of

the Born approximation. In the next section, we use (5.1.5) to calculate the scattering amplitudes of electrons scattered by charged nanomagnets.

5.2 Scattering lengths of unpolarized beams of electrons scattered by charged nanomagnets

In the previous two chapters we have calculated the scattering lengths of electron scattered by neutral nanomagnets for both orientations; magnetic moment of nanomagnets parallel and perpendicular to the electron initial velocity for polarized and unpolarized electron beams. The scattering lengths obtained in each cases are small. We are interested to enhance this small scattering lengths using charged nanomagnets. Below we present the method to do this.

5.2.1 The magnetic moment $\vec{\mu}$ parallel to initial velocity of electrons

Consider the scattering of electrons coming with velocity $\vec{v}$ from infinity parallel to the z-axis by a nanomagnet with a magnetic moment $\vec{\mu}$ oriented along the z-axis. The nanomagnet is modeled by a spherical particle of radius a possessing the magnetic moment $\vec{\mu}$. The contribution of the Coulomb potential to the scattering amplitude according to (5.1.5) is given by

$$\vec{f_C}(\varphi) = -\frac{m^*}{\hbar^2\sqrt{2\pi k}} \int_0^{2\pi} \int_a^{\infty} e^{-i\vec{q}\cdot\vec{\rho'}} V_C(\vec{\rho'}) \rho' d\rho' d\varphi \vec{\chi}_0(S), \tag{5.2.1}$$

where $V_C(\vec{\rho'})$ is given by (5.1.3). The integration in (5.2.1) with respect to ρ' starts with $\rho' = a$ due to the finite size of the nanomagnet. Using $\int_a^{\infty} = \int_0^{\infty} - \int_0^a$, we carry

out integration in (5.2.1) and present the final result in the form

$$\vec{f}_C(ka,\varphi) = f_C(ka,\varphi)\vec{\chi}_0(S), \tag{5.2.2}$$

where

$$f_C(ka,\varphi) = \sqrt{\frac{L_{0C}}{ka}}\left[\frac{1}{qa+q_sa} - F(qa,q_sa)\right] \tag{5.2.3}$$

and

$$L_{0C} = \frac{2\pi Z^2}{\epsilon^2}\left(\frac{e^2}{a}\right)^2\left(\frac{m^*a^2}{\hbar^2}\right)^2 a \tag{5.2.4}$$

specifies scattering length of the Coulomb scattering of a nanomagnet of radius a. Details of calculations and definition of $F(qa,q_sa)$ are given in the Appendix.

The contribution of the spin-dependent part of the scattering potential (5.1.2) is studied in details in Chapter 3 for the polarized beams of electrons with velocities parallel and perpendicular to the magnetic moment of nanomagnet. For unpolarized beams, the spin dependent scattering amplitude is discussed in Chapter 4 and given by equation (4.1.5). We may rewrite this equation by introducing a subscript S as follow

$$\vec{f}_S(\varphi) = f^{\parallel}_{S\uparrow}(\varphi)\begin{pmatrix}1\\0\end{pmatrix} + f^{\parallel}_{S\downarrow}(\varphi)\begin{pmatrix}0\\1\end{pmatrix}, \tag{5.2.5}$$

where

$$f^{\parallel}_{\uparrow S}(\varphi) = \frac{6\gamma\pi}{a}\big[\alpha(I_1\sin^2\frac{\varphi}{2} + I_2\cos^2\frac{\varphi}{2}) + \frac{\beta}{2}\big(I_2-I_1\big)\sin\varphi\big], \tag{5.2.6}$$

$$f^{\parallel}_{\downarrow S}(\varphi) = \frac{6\gamma\pi}{a}\big[-\beta(I_1\sin^2\frac{\varphi}{2} + I_2\cos^2\frac{\varphi}{2}) + \frac{\alpha}{2}\big(I_2-I_1\big)\sin\varphi\big]. \tag{5.2.7}$$

The superscript $\|$ denotes that the incident electron beam is parallel to $\vec{\mu}$, the arrows specify direction of the electron spin after scattering. I_1 and I_2 are given by equations (3.3.6) and (3.3.7). The total scattering amplitude is the sum of (5.2.2) and (5.2.5). It would be convenient to present it as the following two component spinor

$$\vec{f}^{\|}(\varphi) = \left| \begin{array}{c} \alpha f_C(\varphi) + f^{\|}_{\uparrow S}(\varphi) \\ \beta f_C(\varphi) + f^{\|}_{\downarrow S}(\varphi) \end{array} \right|. \tag{5.2.8}$$

The first component of the spinor is the scattering amplitude of electrons having spin along z-axis (spin up) after scattering and the second component is the electrons scattering amplitude with spin down after scattering. The scattering amplitudes (5.2.8) contains two scattering sources, one from screened Coulomb potential and the other from the spin dependent interaction.

For sake of convenience we may rewrite equations (5.2.6) and (5.2.7) as follow

$$f^{\|}_{\uparrow S}(ka,\varphi) = \sqrt{L_0}\left[\alpha\sqrt{\tilde{L}_1} + \beta\sqrt{\tilde{L}_3}\right], \tag{5.2.9}$$

$$f^{\|}_{\downarrow S}(ka,\varphi) = \sqrt{L_0}\left[-\beta\sqrt{\tilde{L}_1} + \alpha\sqrt{\tilde{L}_3}\right], \tag{5.2.10}$$

where L_0, $\tilde{L}_1$, and $\tilde{L}_3$ are given by equations (3.3.11), (3.4.7), and (3.4.9), respectively. The total differential scattering lengths when $\vec{v}$ of incident beam of electrons are parallel to $\vec{\mu}$ of nanomagnets can be written as

$$|f^{\|}_{\uparrow}(ka,\varphi)|^2 = [\alpha f_C(ka,\varphi) + f^{\|}_{\uparrow S}(ka,\varphi)]^2, \tag{5.2.11}$$

$$|f^{\|}_{\downarrow}(ka,\varphi)|^2 = [\beta f_C(ka,\varphi) + f^{\|}_{\downarrow S}(ka,\varphi)]^2 \tag{5.2.12}$$

The scattering lengths (5.2.11) and (5.2.12) symmetrically depend on the spin polarization of the incident beam of electrons α and β. The general properties of these lengths are discussed below in Section 5.4.

5.2.2 The magnetic moment $\vec{\mu}$ perpendicular to initial velocity of electrons

Now we consider the case when the magnetic moment $\vec{\mu}$ is transverse to z-axis. We keep the previous direction for velocity $\vec{v}$ of electrons along the z-axis. Let $\vec{\mu}$ be along positive x-axis. The interaction potential (3.3.1) preserves its form. Acting as above and following the same procedures as in Chapter 3, we obtain the spin dependent scattering amplitudes

$$\vec{f}^{\perp}(\varphi) = \left| \begin{array}{c} \alpha f_C(\varphi) + f^{\perp}_{\uparrow S}(\varphi) \\ \beta f_C(\varphi) + f^{\perp}_{\downarrow S}(\varphi) \end{array} \right|, \tag{5.2.13}$$

where $f^{\perp}_{\uparrow S}(\varphi)$ and $f^{\perp}_{\downarrow S}(\varphi)$ represent the spin dependent 2D scattering amplitudes of electron with initial velocity perpendicular ($\perp$) to $\vec{\mu}$ with the spin up and down after scattering, respectively.

The amplitudes $\vec{f}^{\perp}_{\uparrow S}(\varphi)$ and $\vec{f}^{\perp}_{\downarrow S}(\varphi)$ are presented as

$$f^{\perp}_{\uparrow S}(\varphi) = \sqrt{L_0}\big[\beta\sqrt{\tilde{L}_2} + \alpha\sqrt{\tilde{L}_3}\big], \tag{5.2.14}$$

$$f^{\perp}_{\downarrow S}(\varphi) = \sqrt{L_0}\big[\alpha\sqrt{\tilde{L}_2} - \beta\sqrt{\tilde{L}_3}\big], \tag{5.2.15}$$

where we used equations (3.3.11), (3.4.8),and (3.4.9). The total differential scattering lengths in this case can be presented as

$$|f_{\uparrow}^{\perp}(ka,\varphi)|^2 = [\alpha f_C(ka,\varphi) + f_{\uparrow S}^{\perp}(ka,\varphi)]^2, \tag{5.2.16}$$

$$|f_{\downarrow}^{\perp}(ka,\varphi)|^2 = [\beta f_C(ka,\varphi) + f_{\downarrow S}^{\perp}(ka,\varphi)]^2. \tag{5.2.17}$$

In next section, we discuss the general properties of the differential scattering lengths (5.2.11-5.2.12) and (5.2.16-5.2.17) as functions of the scattering angle φ and the dimensionless parameter ka.

5.3 Possibility of obtaining complete polarization of scattered electrons

The Born approximation used in this paper holds true provided that $|V_C(\rho)+\hat{V}_S(\rho)| \ll \hbar^2/(m^*\bar{\rho}^2)$ [60]. It is necessary to note that unscreened Coulomb potential always completely suppresses the spin-dependent interaction. The last interaction is important only for $q_s\rho >> 1$, where $V_C(\rho) \simeq Ze^2/(\epsilon q_s^2\rho^3)$ [136-137] can be comparable with the spin interaction.

Now we evaluate the charge of the nanomagnet Z. Roughly it can be done by comparing the potential energy of the charged sphere and the kinetic energy of the incident electron

$$Ze^2/\epsilon a = m^* v_F^2/2.$$

Substituting the typical numerical values of the Fermi velocity for 2DEG $v_F = 10^7 cms^{-1}$ [139], $\epsilon = 11.7$, the effective mass $m^* = 0.2m$ (for Si), and setting

$a \sim 10nm$, we obtain $Z \sim 1$. This evaluation allows us to claim that nanomagnets of a radius $a \sim 10\ nm$ immersed into 2DEG at low temperatures carry negative charge approximately equal to one electron.

For evaluation of the screening wave length q_s, we use the relation $q_s = 2/a_B^*$, which gives its upper bound ($a_B^* = \frac{\epsilon\hbar^2}{m^* e^2}$ is the effective Bohr radius) [136]. Using the numerical values of the effective masses (m^*) and static dielectric constants (ϵ) of some 2DEGs, we calculate q_s. The limitations on the nanomagnet size a can be obtained from condition of validity of the Born approximation to the scattering of electrons by 2D screened Coulomb potential. Considering the screened Coulomb potential at $q_s\rho \gg 1$ and using inequality $|e^2/(\epsilon q_s^2 \bar{\rho}^3)| \ll \hbar^2/(m^*\bar{\rho}^2)$ after setting $\bar{\rho} \sim a$, we obtain $a \gg (e^2 m^*)/(\epsilon\hbar^2 q_s^2)$. Substituting the numerical values of m^* and q_s, we obtain the lower limit of the nanomagnet size a. The results of these calculations are given in Table 5.1. In Chapter 3, we found that the upper limit of the typical size of nanomagnet is specified by $a^2 \ll (100\ nm)^2/\nu$. In this paper, we deal with $a \geq 10\ nm$ and $\nu > 1$. It means that conditions of the lower limit of a are made (see Table 1). Therefore, only the upper limit of a is important for applicability of the Born approximation for charged nanomagnets. We present the corresponding inequality in the following form

$$a < \frac{100}{\sqrt{\nu}}\ nm. \tag{5.3.1}$$

The scattering length of electrons scattered from the charged nanomagnet is given by $|f_C + f_S|^2$. Factorizing out L_0, we obtain the following result

$$|\vec{f}^{\parallel}_{\uparrow,\downarrow}|^2 = \frac{L_0}{ka}\left\{\sqrt{\frac{L_{0C}}{L_0}}\left[\frac{1}{qa + q_s a} - F(qa, q_s a)\right] + \sqrt{ka}\left(\sqrt{\tilde{L}_3} \pm \sqrt{\tilde{L}_1}\right)\right\}^2, \tag{5.3.2}$$

Material	m*	ϵ	calculated q_s	lower limit of a (nm)	q_s from [135]
Ge	0.082	15.8	2.4	2	-
Si	0.19	11.7	7.8	0.6	18
GaAs	0.066	13.13	2.5	1.8	-
InAs	0.026	14.55	0.95	4.6	1.1

Table 5.1: Numerical values of q_s in units $10^6 cm^{-1}$, the effective mass m^* in units of the mass of free electron, and lower limit of a in nm.

where

$$\sqrt{\frac{L_{0C}}{L_0}} = \frac{Ze^2}{4\pi\epsilon\nu\mu_B^2 n_a a}. \tag{5.3.3}$$

Formula (5.3.2) uses the general expressions of the 2D screened Coulomb potential (5.2.3). Below we are working in the "far" distances from the scattering center where the asymptotic expression of $V_C = Ze^2/(\epsilon q_s^2 \rho^3)$. With this expression (5.3.2) reduces to

$$|\vec{f}^{\parallel}_{\uparrow,\downarrow}|^2 = \frac{L_0}{ka}\left\{\sqrt{\frac{L_{0C}}{L_0}}\frac{1}{(q_s a)^2}\big[F_2(qa) - qa\big] + \sqrt{ka}\left(\sqrt{\tilde{L}_3} \pm \sqrt{\tilde{L}_1}\right)\right\}^2, \tag{5.3.4}$$

where $F_2(qa) = HPFQ[\{-\frac{1}{2}\}, \{\frac{1}{2}, 1\}, -\frac{(qa)^2}{4}]$ (see Appendix). We note that the numerical calculations according to (5.3.2) and (5.3.4) give practically the same results for $q_s a >> 1$.

As discussed in Chapter 3, the 2D spin-dependent scattering of polarized electrons by neutral nanomagnets is considerably anisotropic for $ka \sim 0.2$. But this anisotropy is small. It is important to note that the scattering of unpolarized electron beams by neutral nanomagnets shows the possibility of obtaining dominant or even complete polarization at some scattering angles and it can be enhanced by charged nanomagnets. Our numerical analysis shows that along with the inequality $q_s a >> 1$ the additional condition $q_s a \gg qa$ must be true. These inequalities guaranty that scattering is controlled by screened Coulomb and spin-dependent potentials simultaneously. Below,

we analyze the graphs of the dimensionless scattering lengths, which are given by the relations:

$$\tilde{L}^{\parallel}_{\uparrow} = \frac{1}{L_0}\frac{dL^{\parallel}_{\uparrow}}{d\varphi} = \frac{1}{L_0}\big[f^{\parallel}_{\uparrow}(ka,\varphi)\big]^2, \qquad \tilde{L}^{\parallel}_{\downarrow} = \frac{1}{L_0}\frac{dL^{\parallel}_{\downarrow}}{d\varphi} = \frac{1}{L_0}\big[f^{\parallel}_{\downarrow}(ka,\varphi)\big]^2, \tag{5.3.5}$$

$$\tilde{L}^{\perp}_{\uparrow} = \frac{1}{L_0}\frac{dL^{\perp}_{\uparrow}}{d\varphi} = \frac{1}{L_0}\big[f^{\perp}_{\uparrow}(ka,\varphi)\big]^2, \qquad \tilde{L}^{\perp}_{\downarrow} = \frac{1}{L_0}\frac{dL^{\perp}_{\downarrow}}{d\varphi} = \frac{1}{L_0}\big[f^{\perp}_{\downarrow}(ka,\varphi)\big]^2. \tag{5.3.6}$$

The quantities $\tilde{L}^{\parallel}_{\uparrow}$, $\tilde{L}^{\parallel}_{\downarrow}$, $\tilde{L}^{\perp}_{\uparrow}$, and $\tilde{L}^{\perp}_{\downarrow}$ describe the scattering of electrons with $\vec{v} \parallel$ and $\perp$ to $\vec{\mu}$ and with spin up and down after scattering, respectively.

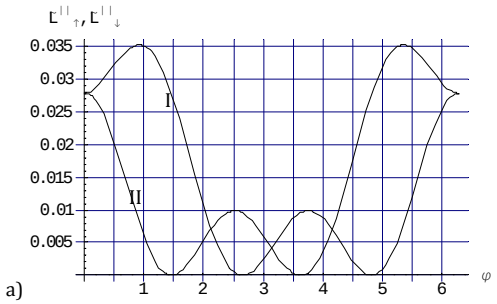

Figure 5.1: $\tilde{L}^{\parallel}_{\uparrow}$ (curve I) and $\tilde{L}^{\parallel}_{\downarrow}$ (curve II) versus φ for $ka = 0.5$, according to equation (5.3.5) for pure spin part only.

To illustrate the possibility of the complete spin polarization of scattered electrons, we consider the scattering of unpolarized beams of electrons by a neutral nanomagnets. Figure 5.1 shows that in the vicinity of scattering angles $\varphi = 1.5$ and 3.5 rad all scattered electrons have spin up. At the same time, in the vicinity of scattering angles 2.5 and 4.5 rad all scattered electrons have spin down. This means that we can obtain the complete spin polarization from unpolarized beams of electrons by a single nanomagnet. Curves I and II depend only on ka. The experimentally measurable scattering lengths are obtained by multiplication of $\tilde{L}^{\parallel}_{\uparrow}, \tilde{L}^{\parallel}_{\downarrow}$ by $L_0 = \nu^2 a^5 \big(m^*/m_e\big)^2 10^{21}$ cm (a

measured in cm). This formula is obtained according to (3.3.11) after substitution of numerical values of the universal constants and $n_a = 10^{22} cm^{-3}$.

Now we consider the scattering from cahrged nanomagets. The numerical calculations and graphical analysis show that peculiarities of spin-dependent scattering can be preserved only if $\sqrt{L_{0C}/L_0} < 10^2$ (see (5.3.3)). It gives one more restriction on the size of nanomagnet $\nu a \geq 100\ nm$, which is consistent with the condition of applicability of the Born approximation (5.3.1).

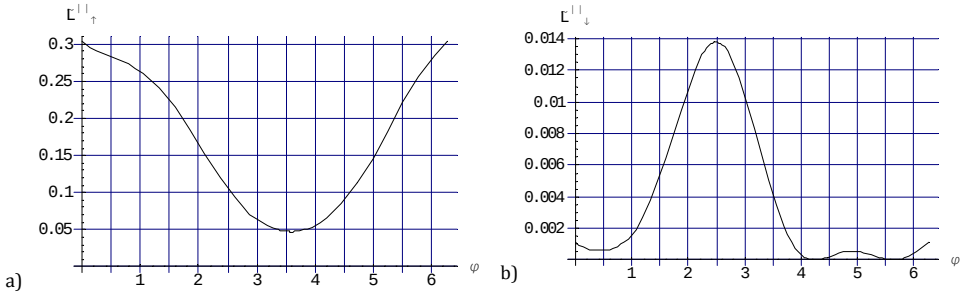

Figure 5.2: (a) $\tilde{L}_{\uparrow}^{\parallel}$ and (b) $\tilde{L}_{\downarrow}^{\parallel}$ versus φ for $ka = 0.2$, $a = 30\ nm$, $\nu = 5$, $q_s = 7.8 \times 10^6 cm^{-1}$ (Si), according to (5.3.5).

Figures 5.2(a) and (b) illustrate the dimensionless scattering lengths of Si 2DEGs, which is the most favorable candidate for the experimental separation of electron beams with different spin polarization. Comparisons of these two graphs shows that in the range of scattering angles $\varphi = 0$ to 1 rad practically all scattered electrons have spin up. The same is true for the scattering angles around $\varphi = 4.2$ and $\varphi = 5.6$ rad. Even at $\varphi = 2.33$ rad, where $\tilde{L}_{\downarrow}^{\parallel}$ has maximum value, 90% of the scattered electrons have spin up.

For comparison in Fig. 5.3 we present the same scattering lengths but for parameters that differs from those in Fig. 5.2. As one can see at every scattering angle φ $\tilde{L}_{\uparrow}^{\parallel}$

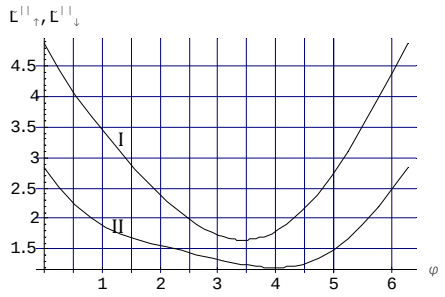

Figure 5.3: $\tilde{L}^{\parallel}_{\uparrow}$ (curve I) and $\tilde{L}^{\parallel}_{\downarrow}$ (curve II) versus φ for $ka = 0.2$, $a = 10\ nm$, $\nu = 20$, $q_s = 7.8 \times 10^6 cm^{-1}$ (Si), according to (5.3.5).

(curve I) is greater than $\tilde{L}^{\parallel}_{\downarrow}$ (curve II). In the range of scattering angles $0 \leq \varphi \leq 1.5$, the ratio of $\tilde{L}^{\parallel}_{\uparrow}$ and $\tilde{L}^{\parallel}_{\downarrow}$ is 1.3 (56% of electrons with spin up). The scattering length $\tilde{L}^{\parallel}_{\uparrow}$ of Fig. 5.3 is approximately 15 times greater than $\tilde{L}^{\parallel}_{\uparrow}$ of Fig. 5.2(a) and $\tilde{L}^{\parallel}_{\downarrow}$ 200 times greater than $\tilde{L}^{\parallel}_{\downarrow}$ of Fig. 5.2(b). But, according to Fig.5.3 one can not speak about the dominant spin polarization.

Now we consider the electron scattering by charged nanomagnets with magnetic moment perpendicular to the velocity of the incident electrons. Figure 5.4 shows $\tilde{L}^{\perp}_{\uparrow}$ (curve I) and $\tilde{L}^{\perp}_{\downarrow}$ (curve II) for the same parameters in Fig. 5.2. At scattering angle $\varphi = \pi/2$, $\tilde{L}^{\perp}_{\uparrow}$ approximately 2 times grater than $\tilde{L}^{\perp}_{\downarrow}$. It means that around $\varphi = \pi/2$ about 70% of the scattered electrons have spin up and 30% spin down.

Finally, we would like to note that Si 2DEG is not only one candidate for spin separation. The 2DEGs of Ge and $GaAs$ can be also used for this purpose. In particular, we calculated the differential scattering lengths for $GaAs$ when $ka = 0.2$, $\nu = 2$ and $a = 70\ nm$. The graphs of the scattering lengths $\tilde{L}^{\parallel}_{\uparrow}$ and $\tilde{L}^{\parallel}_{\downarrow}$ for $GaAs$ is depicted in Fig. 5.5. In the region $0 \leq \varphi \leq 0.5$ rad about 95% of the scattered electrons have spin point up. The complete spin polarization of the scattered electrons obtained in

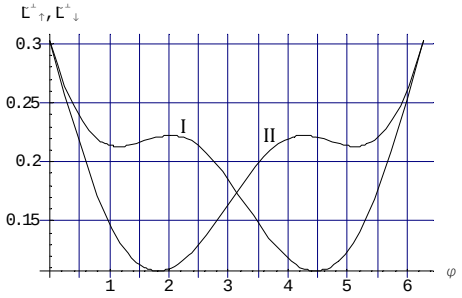

Figure 5.4: $\tilde{L}^{\perp}_{\uparrow}$ (curve I) and $\tilde{L}^{\perp}_{\downarrow}$ (curve II) versus φ for $ka = 0.2$, $a = 30\ nm$, $\nu = 5$, $q_s = 7.8 \times 10^6 cm^{-1}$ (Si), according to (5.3.6).

the vicinity of $\varphi = 4.8$ rad. However, the value $a^2\nu$ is on the edge of applicability of the Born approximation.

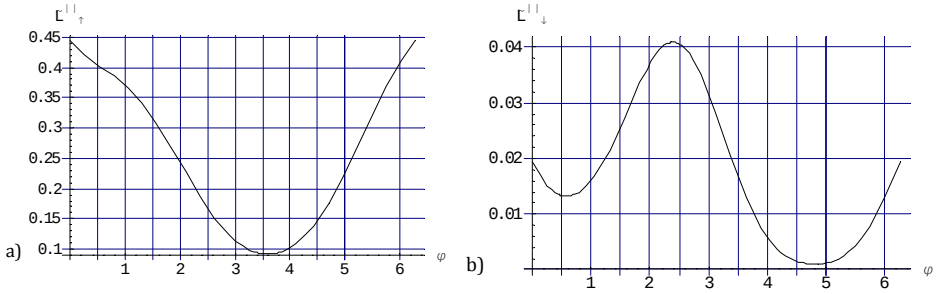

Figure 5.5: (a) $\tilde{L}^{\parallel}_{\uparrow}$ and (b) $\tilde{L}^{\parallel}_{\downarrow}$ versus φ for $ka = 0.2$, $a = 70nm$, $\nu = 2$, $q_s = 2.5 \times 10^6 cm^{-1}$ $(GaAS)$, according to (5.3.5).

On the other hand, one can expect that the scattering of very slow particles by charged nanomagnets is isotropic with considerable scattering lengths. We have calculated the scattering lengths for $ka = 0.01$ and obtained that the scattering is practically isotropic for the incident beams parallel and transverse to the magnetic moment of nanomagnets. The scattered electrons are unpolarized at any scattering angles and the scattering lengths are comparatively large. This feature of scattering for very

slow electrons are shown in Fig. 5.6(a) and (b) for initial electron velocity parallel and perpendicular to the magnetic moment of nanomagnets, respectively.

When one over look Fig. 5.6(b) it seems anisotopic. But, a close observation shows that it is isotropic. To confirm this we may consider the difference between the maximum and minimum value of the scattering length. This difference is only 3 or the ratio of $\tilde{L}^{\perp}_{\uparrow}$ when it gets maximum to $\tilde{L}^{\perp}_{\uparrow}$ its minimum gives ~ 1.

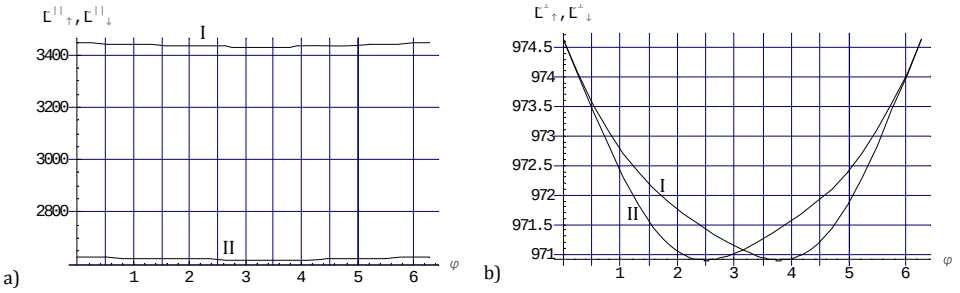

Figure 5.6: (a) $\tilde{L}^{\parallel}_{\uparrow}$ (curve I) and $\tilde{L}^{\parallel}_{\downarrow}$ (curve II), according to (5.3.5). (b) $\tilde{L}^{\perp}_{\uparrow}$ (curve I) and $\tilde{L}^{\perp}_{\downarrow}$ (curve II) according to (5.3.6) . Both graphs drawn for $ka = 0.001$, $a = 10nm$, $\nu = 10$, $q_s = 7.8 \times 10^6 cm^{-1}$ (Si).

5.4 Flux densities of scattered electrons with particular polarization

At the end of this section, we consider the 2D currents of the scattered electrons with account of the spin polarization. The 2D spin dependent scattered current density (flux density) of electrons is given by the following relations

$$J^{\parallel,\perp}_{Sc}(ka,\varphi) = \frac{\left|\vec{f}^{\parallel,\perp}(ka,\varphi)\right|^2 J_{inc}}{\rho}. \tag{5.4.1}$$

Here, $J_{Sc}^{\parallel,\perp}(ka,\varphi)$ is 2D flux density (number of electrons per unit length per unit time in the direction of $\varphi, \varphi + d\varphi$) scattered by a charged nanomagnets with $\vec{\mu} \parallel$ or $\perp$ to the initial velocity of incident beams, $J_{inc} = \frac{\hbar k}{m^*} n_s$ is the flux density of incident beams (n_s is the surface density number of electrons), $\vec{f}^{\parallel,\perp}(ka,\varphi)$ is the scattering amplitudes given by (5.2.8) or (5.2.13), and ρ is the distance from the scattering center to a detector. According to the requirements of the scattering theory, $\rho \gg a$ (for evaluations we may set $\rho = 100a$). The flux density (5.4.1) includes electrons with spin up and spin down. The above obtained formulas allow us to specify the flux densities for both orientations of spin. With the help of equations (5.3.5) and (5.3.6), we rewrite (5.4.1) in the following way

$$\frac{J_{Sc,j}^{i}}{J_{in}} = \frac{L_0 \tilde{L}_j^i}{\rho}. \tag{5.4.2}$$

The indexes i and j stand for $\parallel, \perp$ and $\uparrow, \downarrow$, respectively. For example, $J_{Sc,\uparrow}^{\parallel} = (L_0 \tilde{L}_{\uparrow}^{\parallel}/\rho) J_{in}$ gives the flux density of electrons with spin up scattered by the nanomagnets with $\vec{\mu}$ parallel to $\vec{v}$. Substituting the numerical values of the universal constants in L_0 (3.3.11) and setting $n_a = 10^{22} cm^{-3}$, $\rho = 100a$, we obtain

$$\frac{J_{Sc,j}^{i}(ka,\varphi)}{J_{inc}} = 10^{19} a^4 \nu^2 (m^*/m_e)^2 \tilde{L}_j^i(ka,\varphi). \tag{5.4.3}$$

We have calculated $\tilde{L}_j^i$ for nanomagnets with different a and ν for $ka = 0.2$, $m^*/m_e = 0.2$ (Si 2DEG). The most favorable situation corresponds to $a = 30\ nm$ and $\nu = 5$. In this case, the average $\tilde{L}_{\uparrow}^{\parallel} = 0.28$ in the intervals of the scattering angles $0 \leq \varphi \leq 1$ (see Fig. 5.2(a)). The formula (5.4.3) gives $J_{Sc\uparrow}^{\parallel} \simeq 2.2 \times 10^{-4} J_{inc}$ and $J_{Sc\downarrow}^{\parallel} \simeq 10^{-3} J_{Sc\uparrow}^{\parallel}$ (for the same ka and φ). This result shows that practically all scattered electrons in the above specified range of φ have spin up. The density

flux of these electrons can be increased by increasing a number of scattering centers (nanomagnets).

5.5 Conclusions

The results of our study shows that it is possible to obtain the complete spin polarization of unpolarized beams of electrons after scattering by single neutral nanomagnet for some scattering angles. However, the corresponding scattering lengths are very small. To enhance the scattering lengths one can use the charged nanomagnets. Our evaluations show that at low temperatures the nanomagnets with a typical size of the order of 10 nm carry a negative charge approximately equal to 1 electron. The screened Coulomb potential does not suppress the peculiarities of the spin dependent scattering when we use Si 2DEG for parameters $ka = 0.2$, $a = 30$ nm, and $\nu = 5$ that allow to use Born approximation. The scattering lengths by charged nanomagnets are larger by approximately one order comparing with the ones obtained for neutral nanomagets. The considerable spin polarized currents in 2D geometry can be obtained with the help of a large number of charged scatterers. We could not find the parameters of the scattering systems, which provide the complete polarization of electrons at any scattering angles $\vec{\mu}$ transverse to the velocity of incident beams.

Chapter 6

2D Spin-Dependent Diffraction of Electrons from Periodical Chains of Nanomagnets

Modern technology enables to manufacture the nanomagnets with anomalous magnetic moments [122, 125, 126]. Thier physical properties of these nanomagnets recently have been studied experimentally [124-125, 127, 129-130], theoretically [123, 126], and by computer simulation [128]. The interaction between anomalous magnetic moment of the nanomagnet and the magnetic moment of electron manifests itself in the spin-dependent electron scattering. The spin-dependent scattering of electrons by nanomagnets in 2D geometry was studied in Chapter 3. In this Chapter, in the Born approximation, we have studied the scattering of polarized beams of electrons by nanomagnets. The study indicated that such scattering can considerably change the polarization of the slow incident electrons. However, the scattering amplitudes of this process were relatively small due to the smallness of the magnetic interactions. The anisotropy of 2D spin-dependent electron scattering may be used to control the spin currents. The corresponding scattering amplitudes can be increased by using a large number of scatterers. The usage of periodical chains of nanomagnets with

specially tuned distance between them allows one to use the diffraction properties of the scattering. This helps to obtain rather sharp maximums in the angle distribution of the polarized electrons.

In this Chapter, we consider the elastic 2D scattering of electron by nanomagnets. We find out that the probabilities of scattering depend on the spin polarization of incident and scattered electrons. With the help of the obtained scattering lengths, we consider the diffraction of the unpolarized beams of electrons from the linear periodical chains of nanomagnets and analyze the angular-spin dependence of the diffraction patterns.

6.1 Probabilities of spin-dependent scattering by nanomagnet

The Pauli equation of an electron moving in the magnetic field of the nanomagnet may be presented by Eq. (3.1.1) and recalling this equation

$$\hat{H} = \frac{1}{2m}\big[\hat{\vec{p}} + \frac{e}{c}\vec{A}\big]^2 + \mu_B \hat{\sigma} \cdot \vec{B}. \tag{6.1.1}$$

Below we consider the case when the magnetic moment of the nanomagnet $\vec{\mu}$ is in the $x - z$ plane. For this case the Hamiltonian (6.1.1) is reduced to the 2D problem and takes the form

$$\hat{H} = \frac{1}{2m}\hat{\vec{p}}_2^2 + \hat{V}(\vec{\rho}). \tag{6.1.2}$$

Here, $\hat{\vec{p}}_2^2$ and $\vec{\rho}$ are the two dimensional momentum operator and the radius vector of the electron, respectively. The second term in (6.1.2) describes the interaction of the

magnetic moments of electrons and the nanomagnets in the dipole-dipole approximation

$$\hat{V}(\vec{\rho}) = \frac{\mu_B}{\rho^3}\bigg(3(\vec{\mu}\cdot\vec{n})\vec{n}\cdot\hat{\sigma} - \vec{\mu}\cdot\hat{\sigma}\bigg), \tag{6.1.3}$$

where $\vec{n}$ is a unit vector along the radius vector $\vec{\rho}$.

Treating (6.1.3) as a small perturbation, we use the Fermi golden rule and write down the probability of transition of the electron from the initial state i to the final state f as follows [60]

$$dW_{fi} = \left(\frac{2\pi}{\hbar}\right)|\hat{V}_{fi}|^2\delta(E_f - E_i)d\nu_f, \tag{6.1.4}$$

where E_i and E_f are the energies of the electron in its initial and final state, respectively. $\hat{V}_{fi}$ is the matrix element of perturbation (6.1.3), $d\nu_f$ is the interval of the quantum numbers which corresponds to the final states.

Now we apply this formula to the transition from the state of the incident particle with momentum $\vec{p}_i$ to the state with momentum $\vec{p}_f$. As the interval of states $d\nu_f$ we can take $d^2p_f/(2\pi\hbar)^2$. First we express the difference between energies in terms of their momenta as

$$E_f - E_i = (p_f^2 - p_i^2)/2m^*. \tag{6.1.5}$$

Substituting (6.1.5) into (6.1.4) and using the property of delta function, we obtain

$$dW_{fi} = \left(\frac{m^*}{\pi\hbar^3}\right)|\hat{V}_{fi}|^2\delta(p_f^2 - p_i^2)d^2p_f. \tag{6.1.6}$$

The wave functions of the incident and the scattered electron are the products of the plane waves and spin wave functions

$$|i\rangle = \sqrt{\frac{m^*}{p}}\exp\big(\frac{i\vec{p}_i\cdot\vec{\rho}}{\hbar}\big)\vec{\chi}(S_i), \tag{6.1.7}$$

$$|f\rangle = \exp\big(\frac{i\vec{p}_f \cdot \vec{\rho}}{\hbar}\big)\vec{\chi}(S_f). \tag{6.1.8}$$

The incident wave function (6.1.7) relates to the state with wave momentum $\vec{p}_i$ and spin S_i, and the scattered wave function (6.1.8) relates to $\vec{p}_f$ and S_f, respectively. The incident wave function normalized by unit current density and the scattered wave function normalized by the delta function of $\vec{p}_i/(2\pi\hbar)$ [60].

With account of the above normalizations of the wave functions, the relation (6.1.6) has dimension of length as it must be in 2D case and describes the differential scattering length. In 3D case it has dimension of area and describes differential cross-section. Integration in (6.1.6) with respect to p_f with the relation $dp_f^2 = (1/2)d(p_f^2)d\varphi$, we obtain the following expression of the differential scattering length

$$dL(k,\varphi;S_f,S_i) = \frac{m^{*2}}{2\pi\hbar^4 k}\left|\langle\vec{\chi}(S_f)|\int e^{-i\vec{q}\cdot\vec{\rho}}\hat{V}(\vec{\rho})d^2\rho|\vec{\chi}(S_i)\rangle\right|^2 d\varphi, \tag{6.1.9}$$

where $\vec{q} = \vec{k} - \vec{k}_0$, is the transferred momentum, $\vec{k}_0 = \vec{p}_i/\hbar$, $\vec{k} = \vec{p}_f/\hbar$, $k_0^2 = k^2 = \frac{2m^*E}{\hbar^2}$, $q = 2k\sin\frac{\varphi}{2}$, φ is the scattering angle. Realization of the delta function while integrating (6.1.6) with respect to d^2p_f deal that we consider only elastic collisions.

Because of the spin-dependent character of the scattering, the differential scattering length (6.1.9) includes the process with spin flipping and non spin flipping. To distinguish them, to our mind, it would be better to use the spin-dependent scattering amplitudes introduced in Chapter 3. Comparison of (6.1.9) with corresponding result of Chapter 3 (the amplitude square of Eq. (3.1.14), allows one to write down

$$dL(k,\varphi;S_f,S_i) = \big|\langle\vec{\chi}(S_f)|\vec{f}(k,\varphi)\rangle\big|^2, \tag{6.1.10}$$

where the scattering amplitude $\vec{f}(k,\varphi)$ is a two component spinor given by (3.1.14)

$$\vec{f}(k,\varphi) = -\frac{m^*}{\hbar^2\sqrt{2\pi k}}\int e^{-i\vec{q}\cdot\vec{\rho}'}\hat{V}(\vec{\rho}')\rho' d\rho' d\varphi'|\vec{\chi}(S_i)\rangle. \tag{6.1.11}$$

It worth noting that from (6.1.10) one can not obtain the minus sign in (6.1.11). It is known that the usage of the perturbation theory does not allow to obtain the phase factor [60]. The scattering amplitude (6.1.11) was obtained in Chapter 3 with the help of the Born approximation. Its applicability coincides with the applicability of the perturbation theory $|\hat{V}| \ll \hbar^2/(m\bar{\rho}^2)$, where $\bar{\rho}$ is the range of action of the scattering potential $\hat{V}(\rho)$, which is given by equation (6.1.3). For evaluation, we set $|V| \sim \frac{\mu\mu_B}{\rho^3}$. Due to the fast decay of the magnetic dipole-dipole interaction with distance, we take $\bar{\rho} = 2a$. Keeping this in mind, we obtain that the Born approximation is applicable if the following inequality is true (see Chapter 3)

$$\frac{16\pi\nu\mu_B^2 n_a m a^2}{3\hbar^2} \ll 1. \tag{6.1.12}$$

For the magnetic moment of nanoparticle, we used the formula $\mu = \frac{4\pi}{3}\nu\mu_B n_a a^3$, ν is a number of Bohr magnetons carried by the ferromagnetic atom, and n_a is the density of atoms of the nanomagnet. Substituting the numerical values of universal constants and $n_a = 10^{22} cm^{-3}$ we obtain the following restriction on the size of the nanomagnet

$$a < \frac{100}{\sqrt{\nu}}\ nm. \tag{6.1.13}$$

For the typical ν (6.1.13) gives a of the order of 10 nm that allows us to consider only one domain nanomagnets.

The perturbation (6.1.3) is non-spherically symmetric one and depending on the spin degrees of freedom of the electron. This creates some problems while evaluating integral (6.1.11). Basically the scattering amplitude is a two component spinor which depends on the spin polarization of incident electron.

6.2 Scattering amplitudes and scattering lengths

In this Chapter we deal with diffraction of unpolarized beams of electrons by neutral nanomagnets. In Chapter 4, we have been derived the expressions for scattering amplitudes and scattering lengths for the same case of this Chapter. Now, we can use those expressions derived in Chapter 4 for scattering amplitudes and scattering lengths. Those scattering amplitudes are given by equations (4.1.6) and (4.1.7) for the incident beams of electrons parallel to the magnetic moment of the nanomagnets and by equations (4.1.14) and (4.1.15) for the incident beams of electrons transverse to the magnetic moment of the nanomagnets. Moreover, the scattering lengths are given by (4.1.11) and (4.1.12) for $\vec{v}$ parallel to $\vec{\mu}$ and by (4.1.16) and (4.1.17) for $\vec{v}$ perpendicular to $\vec{\mu}$. The corresponding differential scattering lengths are also given by Eqs. (4.2.1-4.2.4). As we have been clearly stated earlier, the magnitude of those differential scattering lengths are small due to the smallness of the magnetic interactions. To increase this we propose to use diffraction of electron from chains of nanomagnets.

The differential scattering lengths (4.2.1-4.2.4) are relatively small as it shown in the corresponding graphs. For the sake of convenience we present Fig. 4.2 as Fig. 6.

Figures 6.1(a) and 6.1(b) illustrate the scattering lengths of unpolarized beams of electron by nanomagnets for $ka = 0.5$ and $ka = 1$, respectively. As one can see from these graphs the scattering lengths became smaller as the energy of the incident electron increases. However, the probability of polarizing the beams considerably increases and for particular values of φ one can get almost complete polarization. From Fig. 6.1(a) one can see that around $\varphi = \pi/2$ rad, practically all scattered electrons have spin up and around $\varphi = 3\pi/2$ rad, all scattered electrons have spin down. The

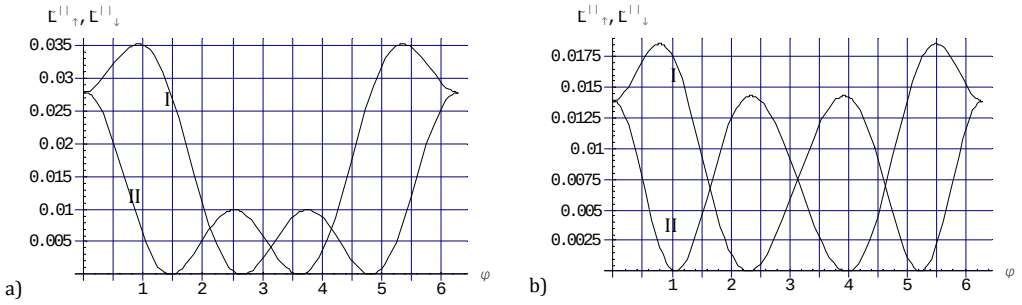

Figure 6.1: $\tilde{L}^{\parallel}_{\uparrow}$ (curve I) and $\tilde{L}^{\parallel}_{\downarrow}$ (curve II) versus φ (in radian). Fig. (a) for $ka = 0.5$, and Fig. (b) for $ka = 1$ according to equations (4.2.1) and (4.2.2).

complete polarization can be also seen in Fig. 6.1(b) at $\varphi = 1$ and $\varphi = 4$ rad (spin up). At the same time, at $\varphi = 2.3$ and $\varphi = 5.3$ rad, all scattered electrons have spin down. The further inspections of Fig. 6.1 (a, b) shows that in the range $0.5 < ka < 1$, the scattering length roughly behaves like $1/ka$.

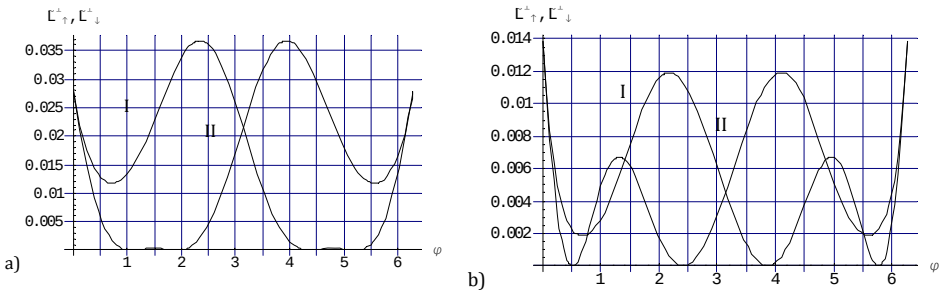

Figure 6.2: $\tilde{L}^{\perp}_{\uparrow}$ (curve I) and $\tilde{L}^{\perp}_{\downarrow}$ (curve II) versus φ (in radian). Fig. (a) for $ka = 0.5$, and Fig. (b) for $ka = 1$ according to equations (4.2.3) and (4.2.4).

Figures 6.2(a) and (b) show the dimensionless scattering lengths $\tilde{L}^{\perp}_{\uparrow}$ (curve I) and $\tilde{L}^{\perp}_{\downarrow}$ (curve II) versus φ, respectively. Just as the case of $\vec{\mu}$ parallel to $\vec{v}$, here also we have complete polarization of the beams for particular values of φ. For example, around $\varphi = 1$ and 2 rad all electrons spin point up and around $\varphi = 4.3$ and 5.3

rad all electrons spin point down for $ka = 0.5$. From Fig. 6.2(b), one can see that practically all spins of electrons oriented up (along $z-$ axis) around $\varphi = 0.5$ and 2.5 rad, and oriented down (along $-z$-axis) for scattering angle $\varphi = 3.8$ and 5.8 rad. Here also the dimensionless differential scattering lengths behave like $1/ka$ in the range of $0.5 \leq ka \leq 1$.

From the above reported graphical results one can conclude that at particular scattering angles in the range of $0.5 \leq ka \leq 1$, the initially unpolarized beam of electrons practically completely polarized. However, the corresponding scattering lengths are comparatively small. They can be considerably increased by interference effects in the scattering from the periodical structures of nanomagnets. We discuss this issue in the next section.

6.3 Diffraction of electrons by linear chains of nanomagnets

A diffraction grating is a pattern of equally spaced slits. Diffraction gratings with multiple slits allows more light through. In diffraction gratings the interference maxima are much sharper than the two slits, allowing the wavelength of the light to be measured more precisely. The condition needed for diffraction grating is an array of obstacles which act as a point like sources for radiation of spherical wavelets. A beams that passes through a diffraction grating exhibits a very sharp maxima interference. Figure 6.3 shows the Fraunhoffer diffraction pattern of a few slits of a grating with N slits, separated from each other by a distance d. The plane waves arrive with the same phase at each slit, and spreads waves are emitted in phase at each slit. We assume the screen position is too far so that the waves propagating allowing the lines indicated

by l_1, l_2, l_3 so on are parallel. The condition for the constructive interference is that each path length differs from one an other by integral multiples of the wave length λ. The path-length difference between adjacent waves is $d \sin\theta$. Hence, the principal maxima is

$$d \sin\theta = m\lambda, \qquad m = 0, \pm 1, \pm 2, ... \tag{6.3.1}$$

The pattern spreads in angle as the ratio λ/d increases. If there were no interference,

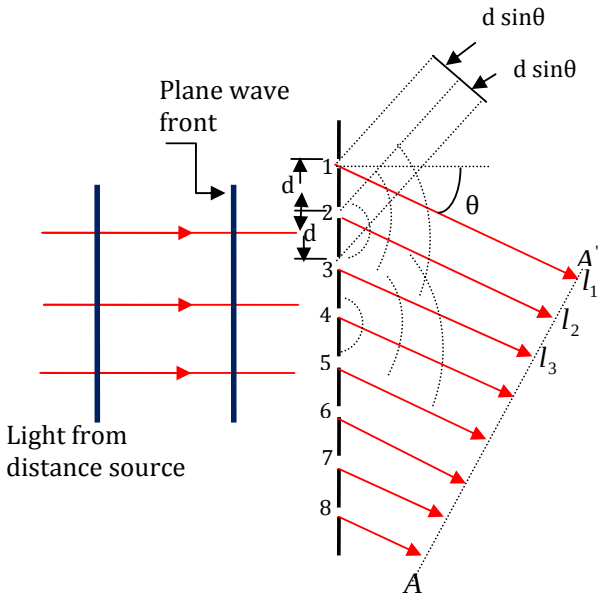

Figure 6.3: Geometry of diffraction grating.

the average intensity over the entire screen due to N slits would be NI_0, where I_0 is the average intensity for single slit [140]. Whether we have or not interference, energy must be conserved so that the average intensity over the whole screen must be NI_0 even with interference. Zero intensity in the region of destructive interference compensated by strong intensity in the constructively interfered region. The amplitudes

of waves arrived at screen from all N slits with the same phase add to N times the field from a single slit. From the other hand, intensity is proportional to the square of the fields. As the result the intensity at any maxima is N^2 times the intensity I_0 due to single slit.

$$I_{max} = N^2 I_0. \tag{6.3.2}$$

If the principal maxima has width $\Delta\theta$, the intensity with the averaged intensity between the maxima is related to this width with the relation [140]

$$I_{max}\Delta\theta \cong NI_0 \times (\textit{angular separation of succesive maxima}) \cong NI_0(\lambda/d).$$

From this the width of the principal maxima obtained as

$$\Delta\theta = \frac{NI_0(\lambda/d)}{I_{max}} = \frac{NI_0(\lambda/d)}{N^2 I_0} = \frac{1}{N}\frac{\lambda}{d}. \tag{6.3.3}$$

This last expression shows that as N increases, the width deceases and the principal maxima become sharper. Now we can apply the above discussed properties of diffraction gratings to our problem. Let us consider the scattering of electrons from a linear chain of equally spaced nanomagnets with lattice constant d. We assume that all nanomagnets are identical. The magnetic moments of the nanomagnets are oriented along the $z-$axis (see Fig. 6.4). This linear chain of nanomagnets can be treated as a diffraction grating for 2D electron beam. According to the Huygens-Fresnel principle every individual nanomagnet can be treated as the source of the spherical waves [141]. But, unlike the convectional 3D or 2D diffraction in the case of 2D spin-dependent scattering by nanomagnets, the amplitude of the scattered wave depends on the scattering angle. As it was illustrated in the previous section, there are some scattering angles (for particular energy of incident electrons) where the unpolarized

incident beams of electrons practically completely polarized. Particularly, according to Fig. 6.1(a), the scattered particles with $ka = 0.5$ completely polarized at $\varphi = 1.5$ rad $\simeq 87^0$. Similarly, it follows from Fig. 6.1(b) that complete polarization observed for scattered electrons with $ka = 1$ at $\varphi = 1$ rad $\simeq 57^0$.

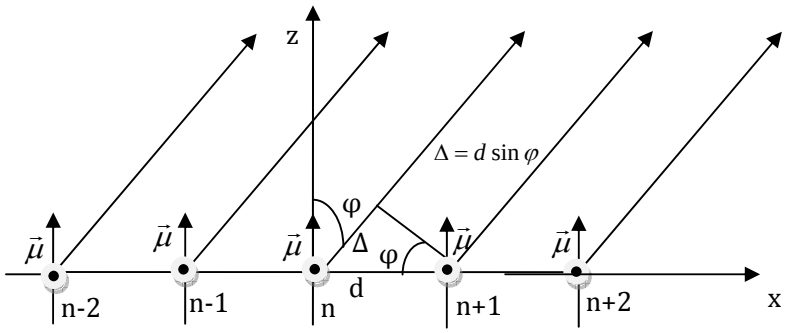

Figure 6.4: Scattering of electrons by linear chains of nanomagnets. The direction of the magnetic moment of the nanomagnets is parallel to the electrons beam velocity.

Consider the case when all path differences Δ ($\Delta = d \sin \varphi$) between the neighboring scattered beams are the same. This condition allows one to find a distance between nanomagnets when all the scattering amplitudes will be added coherently (if they will be put together by methods of focusing the electrons beams far from the chain of the nanomagnets). This condition gives the following relation for the distances between the nanomagnets.

$$d = \frac{2\pi a}{ka \sin \varphi_d}, \tag{6.3.4}$$

where a is the radius of individual nanomagnets and φ_d is the scattering angle with of practically complete polarization. Let us apply this relation to the case $ka = 0.5$ and $\varphi_d \simeq 87^0$. Substituting this parameters in (6.3.4), we get $d = 4\pi a \gg a$. The last

condition is favorable for not taking account of the multiple scattering by neighboring nanomagnets. The typical size of the nanomagnet a must satisfy inequality (6.1.13). For large nanomagnets, the magnetization vectors of the scatterers in the chain will wander and destroy constructive interference.

It is clear that the resultant scattering amplitude at the scattering φ_d is proportional to N (N is the number of the scatterers). The total scattering length corresponding by N scatterers will be proportional to $N^2\tilde{L}_{\uparrow}^{\parallel} \simeq 2.5 \times 10^{-2}N^2$. Even setting $N = 10$, we obtain considerable increment in the scattering length, which allows one to check this theory experimentally.

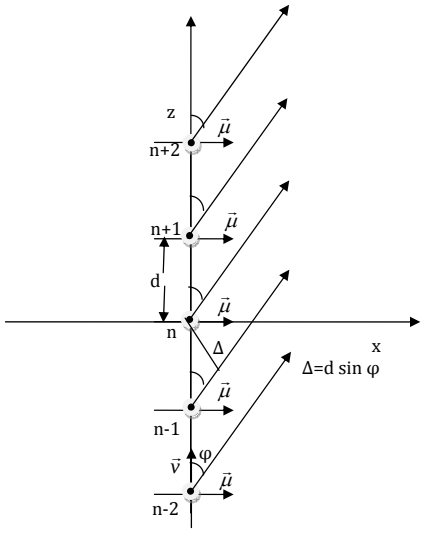

Figure 6.5: Scattering of electrons by linear chains of nanomagnets. The direction of the magnetic moment of the nanomagnets is perpendicular to the electrons beam velocity. The chains are arranged vertically.

In the above discussion, we considered the chain of scatterers with magnetic moment parallel to $z-$axis (Fig. 6.4). In the same manner, one can consider the chain of nanomagnets with the magnetic moments transverse to $z-$axis (Figs. 6.5 and 6.6).

In this case, the largest scattering length of complete polarization $\tilde{L}_{\uparrow}^{\perp} \simeq 0.034$ can be obtained for $ka = 0.5$ at $\varphi = 2$ rad (Fig. 6.2a). It is almost the same as the one obtained from the chain with $\vec{\mu}$ parallel to $z-$ axis. Here, we have two possibilities of arranging the nanomagnets.

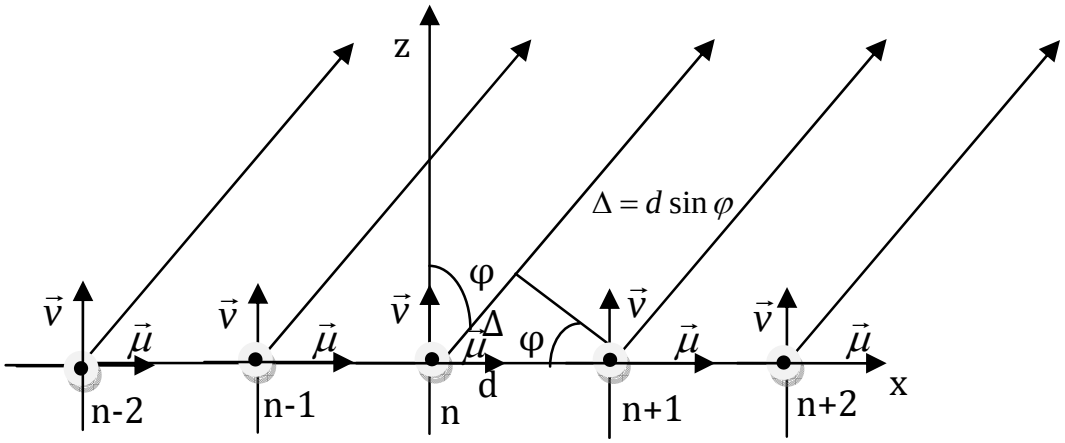

Figure 6.6: Scattering of electrons by linear chains of nanomagnets. The direction of the magnetic moment of the nanomagnets is perpendicular to the electrons beam velocity. The chains are arranged horizontally.

The first one is as shown in Fig. 6.5 and the second one is as shown in Fig. 6.6. In the first case, the chains of the nanomagnets are organized in vertical direction (along $z-$ axis) with their magnetic moments are along $x-$ axis. We keep the direction of initial beams in the $z-$ direction. For this case, the number of beams that arrive at the second scattering center are some fractions of the incident beams. If for some reasons all the initial beams arrived at the first scattering center scattered by the first scatterer, we do not have scattering processes from the rest scatterers and if some of the initial beams reach the second scattering center (the nanomagnet), the fraction of beams that probably arrive at the third and other next scattering centers are going on

decreasing. This shows that this arrangement is not good to enhance the scattering lengths.

The second arrangemnet (Fig. 6.6) gives some contribution to the scattering processes. However, the scattering angles at which we obtain complete polarization relates to back scattering and again this is not favorable. Therefore, comparing the two situations ($\vec{v} \parallel$ to $\vec{\mu}$ and $\vec{v} \perp$ to $\vec{\mu}$), we may claim that the parallel case is favorable than the perpendicular case for the enhancement of scattering lengths.

6.4 Conclusions

In this Chapter, we consider 2D scattering of unpolarized beams of electrons by periodical chains of nanomagnets. Treating the interaction between the magnetic moment of the nanomagnet and the electron as a small perturbation, we obtained the scattering amplitudes and scattering lengths.

One of the main finding of this work is that at some scattering angles it is possible to obtain practically all scattered electrons with the same orientation of their spin. Unfortunately, the scattering lengths of these processes are considerably small. To increase the corresponding scattering lengths, we proposed to use the diffraction of unpolarized electron beams from the periodical chains of nanomagnets. With this aim we studied the diffraction of electrons by a linear periodic chain of nanomagnets. In the case of convectional diffraction, any scatterer is considered as a source of spherical wave with the amplitude which does not depend on the scattering angle. In the case under consideration the scattering potential is not spherically symmetric one. Moreover, it depends on the spin variables of the electron. This results in the strong angular anisotropy of the scattering and its dependence on the spin orientation

of electrons.

By tuning the distance between the nanomagnets, it is possible to organize a diffraction maxima at the scattering angles which corresponds to the dominant spin polarization of the scattered electrons. It is shown that the resultant scattering amplitude in this case is proportional to a number of scatterers (nanomagnets) N. The resultant differential scattering length is proportional to N^2, which is typical for diffraction processes. Even for $N = 10$, the enhancement of the scattering lengths due to diffraction will be of the order of 10^2. This conclusion can be checked experimentally.

Chapter 7

Appendix

The integrals I_1 and I_2 given by (3.3.6) and (3.3.7) can be expressed in terms of the generalized hypergeometric function HPFQ

$$I_1(qa) = qa\left[-\frac{2}{3x}F_1(x,\varphi) + \frac{1}{2x}F_2(x,\varphi)\right]\Bigg|_{qa}^{\infty}, \qquad (A1)$$

$$I_2(qa) = qa\left[\frac{1}{3x}F_1(x,\varphi) - \frac{1}{2x}F_2(x,\varphi)\right]\Bigg|_{qa}^{\infty}, \qquad A2$$

where $F_1 = HPFQ[\{-\frac{1}{2}\},\{\frac{1}{2},1\},-\frac{x^2}{4}]$ and $F_2 = HPFQ[\{-\frac{1}{2}\},\{\frac{1}{2},2\},-\frac{x^2}{4}]$.
Here abbreviation HPFQ stands for the generalized hypergeometric function [*Mathematica 5*,132]. At upper limit $(A1)$ and $(A2)$ give $I_1 = -\frac{qa}{3}$ and $I_2 = 0$. With account of these result and the relation $qa = 2ka\sin\varphi/2$, we obtain

$$I_1(ka,\varphi) = -\frac{2ka}{3}\sin\frac{\varphi}{2} + \frac{2}{3}F_2(ka,\varphi) - \frac{1}{2}F_3(ka,\varphi), \qquad (A3)$$

$$I_2(ka,\varphi) = \frac{1}{2}F_3(ka,\varphi) - \frac{1}{3}F_2(ka,\varphi). \qquad (A4)$$

This allows us with usage of (3.4.7), (3.4.8), and (3.4.9) to present

$$\widetilde{L}_1 = \frac{1}{36ka}\left[-2ka\sin\frac{\varphi}{2}+2ka\sin\frac{\varphi}{2}\cos\varphi+F_1(qa)-\frac{3}{2}(ka)^2\sin^2\frac{\varphi}{2}\cos\varphi F_2(qa)\right]^2, \qquad (A5)$$

$$\widetilde{L}_2 = \widetilde{L}_1 + \frac{4}{9}ka\sin^2\frac{\varphi}{2}\cos^2\frac{\varphi}{2}\left[\frac{3}{4}\sin\frac{\varphi}{2}F_2(qa)\right]^2, \qquad (A6)$$

$$\widetilde{L}_3 = ka\Big\{ \sin\frac{\varphi}{2}\sin\varphi[\frac{1}{3} - \frac{ka}{4}\sin\frac{\varphi}{2}F_2(qa)\Big\}^2. \quad (A7)$$

Integration in (5.2.1) gives

$$\vec{f}_C(\varphi) = -\frac{2\pi m^* z e^2}{\hbar^2\epsilon\sqrt{2\pi k}}\Bigg(\frac{1}{q+q_s} - \frac{x}{q}F_1(x)\Big|_0^{qa} - \frac{q_s\pi}{2q^2}\left[\frac{xJ_1(x)Y_0(bx) - bxJ_0(x)Y_1(bx)}{1-b^2}\right]\Big|_0^{qa}$$

$$+\frac{q_s\pi}{2q^2}\int_0^{qa} xJ_0(x)H_0(bx)dx\Bigg)\left[\alpha\begin{pmatrix}1\\0\end{pmatrix} + \beta\begin{pmatrix}0\\1\end{pmatrix}\right], \quad (A8)$$

where $b = \frac{q_s}{q}$, and $F_1(x) = HPFQ[\{\frac{1}{2}\},\{1,\frac{3}{2}\},-\frac{x^2}{4}]$ is the generalized hypergeometric function PFQ, J_0 and J_1 are the zeroth and first order Bessel functions, Y_0 and Y_1 are the zeroth and first order Neumann functions. The integration in the forth term (A8) can be carried out for small value of qa with the help of $J_0 \approx 1-\frac{x^2}{4}$, $x \ll 1$. Introducing a new variable $y = bx$, we to obtain

$$\frac{q_s\pi}{2q^2}\int_0^{qa} xJ_0(x)H_0(bx)dx = \frac{q_s\pi}{2b^2q^2}\int_0^{q_sa}\big[y - \frac{y^3}{4b^2}\big]H_0(y)dy$$

$$= \frac{q_s\pi}{2b^2q^2}\left[y\ H_1(y) - \frac{y^5}{30\pi b^2} - \frac{y^2}{2b^2}H_2(y) + \frac{y^3}{4b^2}H_3(y)\right]\Big|_0^{q_sa}$$

$$= \frac{a\pi}{2}\left[H_1(q_sa) - (qa)^2\left(\frac{(q_sa)^2}{30\pi} + \frac{1}{2q_sa}H_2(q_sa) - \frac{1}{4}H_3(q_sa)\right)\right]. \quad (A9)$$

Evaluation of the second and third terms of (A5) gives

$$-a\left[F_1(qa) + \frac{q_sa\pi}{2}\left(\frac{qaJ_1(qa)Y_0(q_sa) - q_saJ_0(qa)Y_1(q_sa)}{(qa)^2-(q_sa)^2} - \frac{2}{\pi((qa)^2-(q_sa)^2)}\right)\right]. \quad (A10)$$

With the help of (A9) and (A10), the scattering amplitude of the Coulomb term can be written as

$$\vec{f}_C(\varphi) = -\sqrt{\frac{L_{0C}}{ka}}\left(\frac{1}{qa+q_sa} - F(qa,q_sa)\right)\left[\alpha\begin{pmatrix}1\\0\end{pmatrix} + \beta\begin{pmatrix}0\\1\end{pmatrix}\right]. \quad (A11)$$

where

$$F(qa,q_sa)=F_1(qa)+\frac{q_sa}{(qa)^2-(q_sa)^2}\left(\frac{\pi}{2}\big[qaJ_1(qa)Y_0(q_sa)-q_saJ_0(qa)Y_1(q_sa)\big]-1\right)$$

$$-\frac{\pi}{2}\left[H_1(q_sa)-(qa)^2\left(\frac{(q_sa)^2}{30\pi}+\frac{1}{2q_sa}H_2(q_sa)-\frac{1}{4}H_3(q_sa)\right)\right]. \qquad (A12)$$

We may note that the integration in (A11) gives finite result at $b=q_s/q=1$:

$$\int\frac{\pi q_s}{2q^2}xJ_0(x)\big[Y_0(x)-H_0(x)\big]dx=\frac{q_s}{4q^2}\left[\sqrt{\pi}MeijerG[\{\{\frac{3}{2}\},\{\frac{1}{2}\}\},\{\{1,1\},\{0,\frac{1}{2}\}\},x,\frac{1}{2}]-\right.$$

$$\left.\pi\left(-\frac{2x^3HPFQ[\{\frac{3}{2}\},\{1,\frac{5}{2}\},-\frac{x^2}{4}]}{3\pi}+x^2J_0(x)H_0(x)+J_1(x)H_1(x)\right)\right]. \qquad (A13)$$

H_n $(n=0,1,2,3)$ are the Struve functions, and $MeijerG$ is the Meijer function.

List of Publications and Report on International Conference

1. V.N. Malnev, Teshome Senbeta, Spin dependent 2D electron scattering by nanomagnets, Journal of Magnetism and Magnetic Materials 323 (2011) 1581-1587.

2. Teshome Senbeta, V. N. Malnev, 2D scattering of unpolarized beams of electrons by charged nanomagnets, Journal of Magnetism and Magnetic Materials 324 (2012) 2233-2238.

3. Teshome Senbeta, V. N. Malnev, 2D Spin-Dependent Diffraction of Electrons From Periodical Chains of Nanomagnets, Appl. Sci. 2012, 2, 220-232; doi:10.3390/app2010220.

4. Teshome Senbeta, V. N. Malnev, 2D Spin-Dependent Electron Scattering by Neutral and Charged nanomagnets, Poster presentation on The Seventh International Conference on Magnetic and Super Conducting Materials (MSM11) 10th-13th October 2011, Malaysia (Abstract Book page 169).

Bibliography

[1] Mott, N. F., The electrical conductivity of transition metals, Proc. R. Soc. London, Ser. A **153** , pp. 699-717 (1936).

[2] I. A. Cambell, A. Fert, and A. R. Pomery, Evidence for Two Current Conduction in Iron , Philosophical Magazine, Vol. **15**, pp. 977-981 (1967).

[3] Mark Johnson, *Magnetoelectronics*, First ed., Elsevier Inc. 2004.

[4] Claude Chappert, Albert Fert and Frédéric Nguyen Van Dau, The emergence of spin electronics in data storage, nature materials, Vol. **6**, pp. 813-823 (2007).

[5] A. Fert and I. A. Cambell, Two-Current Conduction in Nickel , Phys. Rev. Vol. **21**, pp. 1190-1192 (1968).

[6] M. I. D'yakonov and V. I. Perel, Possibility of Orienting Electron Spins with Current, A. F. Ioff Phydico-technical Institute, USSR Academy of Sciences, No. **11** pp. 657-660 (1971).

[7] Igor Žutić, Jaroslav Fabian, and S. Das Sarma, Spintronics: Fundamentals and application, Rev. Mod. Phys., Vol. **76**, pp. 323-410 (2004).

[8] Julliér, M, Tunneling between magnetic films; Phys. Lett. **54A**, pp. 225-226 (1975).

[9] Albert Fert, The present and the future of spintronics, Thin SoliD Films **517**, pp. 2-5 (2008).

[10] Truya Shinjo, *Nanomagnetism and Spintronics*, 2nd ed., Elsevier B.V, (2009).

[11] M. N. Baibich, J. M. Broto, A. Fert, F. Nguyen Van Dau, and F. Petroff, Giant magnetoresistance of (001)/Fe(001) Cr magnetic superlattices, Phys. Rev. Lett. **61** , pp 2472-2475 (1988).

[12] G. Bunasch, P. Grunbrg, F. Saurenbach, and W. Zinn, Enhanced magnetoresistance in layered Magnetic Structure with antiferromagnetic interlayer exchange, Phys. Rev. B **39**, pp 4828-4830 (1989).

[13] Lixian Jiang, Hiroshi Naganuma, Mikihiko Oogane, and Yasuo Ando, Large tunnel magnetoresistance of 1056% at room temperature in MgO based double barrier magnetic tunnel junction, Appl. phys. Express **2**, 083002 (2009).

[14] Valet, T. and Fert, A., Theory of the perpendicular magnetoresistance in magnetic multilayer, Phys. Rev. B **48**, pp. 7099-7113 (1993).

[15] H. Ehrenreich and F. Spaepen (Editors), Perspectives of Giant Magneto resistance, Solid state physics Vol. **56**, pp. 113-237 (Academic Press, 2001).

[16] J.M Daugton et al., Magnetic field sensor using GMR multilayer; IEET Trans. Magn. Vol. **30**, pp. 4608-4610 (1994).

[17] Gary A. Prinz, Magnetoelectronics, Science **282**, pp. 1660-1663 (1998).

[18] R. J. Soulen Jr. et al., Measuring spin polarization of ametal with supperconducting point, Science **282**, 85-88 (1998).

[19] Sadamich Maekawa and Teuya Shinjo, *Spin Dependent Transport ain Magnetic Nanostructures*, CRC Press (2002).

[20] Neil W. Ashcroft and N. David Mermim, *Solid State Physic*, Saunders College Publishing (1976).

[21] Fert, A., and Cambell, I. A., J. Phys. F: Metal Phys. **6**, pp. 849-871 (1976).

[22] Cambell, I. A., and Fert, A., *Ferromagnetic materials* (E. P. Wohlfarth, ed.), Vol. **3**, pp. 747-805 (1982).

[23] Mark Johnson, Theory of spin-dependent transport in ferromagnet-semiconductor hetrostructures, Phys. Rev. B,Vol. **58**, pp. 9635-9638 (1998).

[24] Silsbee, R. H., Novel method for the study of spin transport in conductors, Bull. Magn. Reson. **2**, pp. 284-285 (1980).

[25] S. A. Wolf, D. D. Awschalom, R. A. Buhrman, J. M. Daughton, S. von Molnár, M. L.Roukes, A. Y. Chtchelkanova, D. M. Treger, Spintronics: A Spin-based electronics vision for the future, Science **294**, pp. 1488-1495 (2001).

[26] S. Gardelist et al., Phys. Rev. B **60**, pp. 7764-7767 (1999).

[27] Johnson, M. Spin injection and detection in ferromagnetic metal/2DEG structure, Physica E **10**, 472-477 (2001).

[28] S. F. Alvarado and Ph. Renaud, Phys. Rev. Lett. **68**, pp. 1387-1390 (1992).

[29] S. K. Upadhyay et al., Appl. Phys. Lett. **74**, pp. 3881-3883 (1999).

[30] W. H. Rippard and R. A. Buhrman, Phys. Rev. Lett. **84**, pp. 971-974 (2000).

[31] Emmanuel I. Rashba, Spintronics: Sources and Challenge, Journal of Superconductivity: Incorporating Novel Magnetism, Vol. **15**, pp. 13-17 (2002).

[32] J. Wang - K. S. Chan, Spin current in two-dimensional electron gas tunnelling junction, Europhys. Lett. **75**, pp. 281-289 (2006).

[33] Noboru Sakimura, Tadahiko Sugibayashi, Takeshi Honda, Sadahiko Miura, Hideaki Numata, Hiromistu Hada, and Shuichi Tahara, A 512 kb cross-point cell MRAM, ISSCC papers 16.1 (2003).

[34] M.Bowen, M. Bibes, A. Barthélémy, J. -P. Contour, A. Anane, Y. Lemaître, and A. Fert, Nearly total spin polarization in $La_{2/3}Sr_{1/3}MnO_3$ from tunnelling experiments, Appl. Phys. Lett. **82**, pp. 233235 (2003).

[35] T. Ishikawa, T. Marukame, H. Kijima, K.-L. Matsuda, T. Uemura, M. Arita, and M. Yamamoto, Spin-dependent tunneling characteristics of fully epitaxial magnetic tunneling junctions with a full-Heusler alloy Co_2MnSi thin film and a MgO tunnel barrier, Appl. Phys. Lett. **89**, 192505 (2006).

[36] Takao Marukame, Takayuki Ishikawa, Ken-Lchi Matsuda, Tesuya Uemura, and Masafumi Yamamoto, High tunnel magnetoresistance in fully epitaxial magnetic tunnel junctions with a full-Heusler alloy $Co_2Cr0_{.6}Fe_{0.4}Al$ thin film, Appl. Phys. Lett. **88**, 262503 (2006).

[37] D. Chiba, Y. Sato, T. Kita, F. Matsukura, and H. Ohno, Current-driven magnetization reversal in a ferromagnetic semiconductor (Ga,Mn)As/GaAs/(Ga,Mn)As tunnel junction, Phys. Rev. Lett. **93**, 216602 (2004).

[38] M. Elsen, O. Boulle, J.-M. George, H. Jaffrès, R. Mattana, A. Fert, A. Lamaitre, and G. Faini, Spin transfer experiments on (Ga,Mn)As/(In,Ga)As/(Ga,Mn)As tunnel junctions, Phys. Rev. B **73**, 035303 (2006).

[39] P. LeClair, J. K. Ha, H. J. M. Swagten, J. T. Kohlhepp, C. H. van de Vin, and W. J. M. de Jonge, Large magnetoresistance using hybrid spin filter devices, Appl. Phys. Lett. **80**, pp. 625-627 (2002).

[40] M. Hehn, F. Montaigne, and A. Schuhl, Hot-electron three-terminal devices based on magnetic tunnel junction stacks, Phys. Rev. B **66**, 144411 (2002).

[41] Gen Tatara, and Hiroshi Kohno, Theory of current-driven domain wall motion: spin transfer versus momentum transfer, Phys. Rev. Lett. **92**, 086601 (2004).

[42] D. Ravelosona, D. Lacour, J. A. Katine, B. D. Terris, and C. Chappert, Nanometer scale observation of high efficiency thermally assisted current-driven domain wall depinning. Phys. Rev. Lett. **95**, 117203 (2005).

[43] M. Yamanouchi, D. Chiba, F. Matsukura, T. Dietl, and H. Ohno, Velocity of domain-wall motion induced by electrical current in the ferromagnetic semiconductor (Ga,Mn)As, Phys. Rev. Lett. **96**, 096601 (2006).

[44] R. P. Cowburn, and M. E. Welland, Room temperature magnetic quantum cellular automata, Science **287**, pp. 1466-1468 (2000).

[45] Jung-Woo Yoo, Chia-Yi Chen, H. W. Jang, C. W. Bark, V. N. Prigodin, C. B. Eom and A. J. Epstein, Spin injection/detection using an organic-based magnetic semiconductor, Nature Materials, **9**, pp. 638-642 (2010).

[46] D.L. Mills and J.A.C. Bland, *Contemporary Concepts of Condensed Matter Science Nanomagnetism: Ultrathin Films, Multilayers and Nanostructures*, Elsevier B.V. (2006).

[47] Matthias Eschrig, Spin-polarized supercurrents spintronics, Physics Today, **64**, pp. 43-49, (2011).

[48] S. F. Alvarado, Tunneling potential barrier dependence of electron spin polarization, Phys. Rve. Lett. Vol. **75**, pp. 513-516 (1995).

[49] J. M. Kikkawa and D. D. Awschalom, Resonant spin amplification, in $n-$type GaAs, Phys. Rev. Lett. Vol. **80**, pp. 4313-4316 (1998).

[50] J. M. Kikkawa and D. D. Awschalom, Lateral drag of spin coherence in gallium arsenide, Nature Vol. **397**, pp. 139-141 (1999).

[51] D. Hägele, M. Oestreich, W. W. Rühle, N. Nestle, and K. Eberl, Spin transport in GaAs, App. Phys. Lett. Vol. **73**, pp. 1580-1582 (1998).

[52] A. T. Hanbick, B. T. Jonker, G. Itskos, G. Kioseoglou, and A. Petrou, Efficient electrical spin injection from a magnetic metal/tunnel barrier contact into a semiconductor, Appl. Phys. lett. Vol. **80**, pp. 1240-1242 (2002).

[53] V. F. Motsnyi, J. De Boeck, J. Das, W. Van Roy, G. Borghs, E. Goovaerts, V. I Safarov, Electrical spin injection into a ferromagnet/tunnel barrier semiconductor heterostructure, Appl. Phys. lett. Vol. **81**, pp. 265-267 (2002).

[54] Saroj P. Dash, Sandeep Sharma, Ram S. Patel, Michel P. Jong and Ron Jansen, Electrical creation of spin polarization in silicon at room temperature, Nature Vol. **462**, pp. 491-494 (2009).

[55] Tomoyuki Sasaki, Tohru Oikawa, Toshio Suzuki, Masashi Shirashi, Yoshishige Suzuki, and Katsumich Tagami, Electrical spin injection into silicon using MgO tunnel barrier, Appl. phys. Express **2**, 053003 (2009).

[56] Junsaku Nitta, Tatsushi Akazaki, Hideak Takayanagi and Takatom Enoki, Gate control of spin-orbit interaction in an inverted $In_{0.53}Ga_{0.47}As/In_{0.52}Al_{0.48}As$ heterostructure Phys. Rev. Lett. Vol. **78**, pp. 1335-1338 (1997).

[57] G. Meir, T. Matsuyama, and U. Merkt, Field effect in $InAs$/permalloy hyprid transistors Phys. Rev. B Vol. **65**, 125327 (2002).

[58] Yuriy V. Pershin and Vladimir Privman, Spin relaxation of conduction electrons in semiconductors due to interation with nuclear spins, Nano Lett. *3*, pp. 695-700 (2003).

[59] L. I. Schiff, *Quantum Mechanics*, third ed., McGraw-Hill, 1968

[60] L. D. Landau, E.M. Lifshitz, *Quantum Mechanics: Non-Relativistic Theory*, third ed., Pergamon Press, 1977.

[61] Robert M.White, *Quantum Theory of Magnetism*, third ed., Springer-Verlag Berlin Heidelberg 2007.

[62] J. D. Jackson, *Classical Electrodynamics*, 3rd ed., Wiley, 1999.

[63] J.D. Bjorken, S.D. Drell, *Relativistic Quantum Mechanics*, McGraw-Hill, New York 1965.

[64] E. I. Rashba, Properties of semiconductors with an extremum loop I. Cyclotron and combinational resonance in a magnetic fi eld perpendicular to the plane of the loop, Sov. Phys. Solid State **2**, 1109 (1960).

[65] Yu.A. Bychkov, E.I. Rashba, Oscillatory effects and the magnetic susceptibility of carriers in inversion layers, J. Phys. C **17**, pp. 6039-6045 (1984).

[66] Branislav K. Nikolić, Spin-orbit interaction in semiconductor nanostructure, http://www.phys.udel.edu/∼ bnikolic.

[67] G. Engels, J. Lange, Th. Schäpers, and H. Lüth, Experimental and theoretical approach to spin splitting in modulation-doped $In_xGa_{1-x}As/InP$ quantum wells for B $\rightarrow$ 0, Phys. Rev. B **55**, R1958 (1997).

[68] G. Dresselhause, Spin-orbit coupling effects in zinc blende structures, Phys. Rev. **100**, pp. 580 (1955).

[69] R. Winkler, Rashba spin splitting in two-dimensional, electron and hole systems, Phys. Rev. B **62**, pp. 4245-4248 (2000).

[70] Francisco Mireles and Gorge Kirezenow, Ballistic spin-polarized transport and Rashba spin precession in semiconductor nanowires, Phys. Rev. B **64**, 024426 (2001).

[71] Takkaki Koga, Junsaku Nitta, Hideaki Takayanagi, and Supriyo Datta, Spin-filter device on the Rashba effect using a nonmagnetic resonant tunneling diode, Phys. Rev. Lett. **88**, 126601 (2002).

[72] A. G. Mal'shukov, C. S. Tang, C. S. Chu, and K. A. Chao, Spin-current generation and detection in the presence of an ac gate, Phys. Rev. B **68**, 233307 (2003).

[73] Emmanuel I. Rashba, Spin currents in thermodynamic equilibrium: The challeng of discerning transport currents,Phys. Rev. B **68**, 241315(R) (2003).

[74] W Xu, P. Vasilopoulos and X F Wang, Lifetimes of a two-dimensional electron gas in the presence of spin-orbit interaction, Semicond. Sci. Technol. **19**, pp. 224-229 (2004)

[75] Jairo Sinova, Dimitrie Culcer, Q. Niu, N. A. Sinitsyn, T. Jungwirth, and A. H. MacDonald, Universal intrinsic spin Hall effect, Phys. rev. Lett. **92**, 126603 (2004).

[76] S. D. Ganichev, V. V. Bel'kov, L. E. Golub, E. L. Ivchenko, Petra Schneider, S. Giglberger, J. Eroms, J. De Boeck, G. Borghs, W. Wegscheider, D. Weiss, W. Prettl, Experimental separation of Rashba and Dresselhaus spin splittings in semiconductor quantum wells, Phys. Rev. Lett. **92**, 256601 (2004).

[77] Yu-Xian Li, Yong Guo, Bo-Zang Li, Rasbha spin-orbit coupling effect on the noise in quasi-one-dimensional nanowires under an applied magnetic field, Phys. REv. B **72**, 075321 (2005).

[78] John Schliemann and Daniel Loss, Spin-Hall transport of heavy holes in $III-V$ semiconductor quantum wells, Phys. Rev. B **71**, 085308 (2005).

[79] John Schliemann, Daniel Loss and R. M. Weservelt, *Zitterbewegung* of electronic wave packets in $III-V$ Zinc-blende semiconductor quantum wells, Phys. Rev. Lett. **94**, 206801, (2005).

[80] Zhou Li, Zhongshui Ma, A. R. Wright, and Chao Zhang, Spin-orbit interaction enhancement polaron effect in two-dimensional semiconductor, Appl. Phys. Lett. **90**, 112103 (2007).

[81] Xi Fu, Wenhu Liao, and Guanghui Zhou, Spin accumulation in a quantum wire with Rashba spin-orbit coupling, Advances in Condensed Matter Physics **2008**, 152731 (2008).

[82] Koichiro Yaji, Yoshiyuki Ohtsubo, Shinichiro Hatta, Hiroshi Okuyama, Koji Miyamota, Taichi Okuda, Akiko Kimura, Hirofumi Namatame, Masaki Taniguchi and Tesuya Aruga, Large Rashba spin splitting of metallic surface-state band on a semiconductor surface, nature Communications, 10.1038/ncomms 1016 (2010).

[83] Semion Saikin, Min Shen, Ming-C. Cheng, and Vladimir Privman, Semiclassical Monte Carlo for in-plane transport of spin-polarized electrons in $III-V$ heterostructures, J. appl. Phys. **94**, pp. 1769-1975 (2003).

[84] A. G. Mal'shukov and K. A. Chao, Spin Hall conductivity of a disordered two-dimensional electron gas with Dresselhaus spi-orbit intercation, Phys. Rev. B **71**, 121308 (2005).

[85] Shengli Zhang, Run Liang, Erhu Zhang, Lei Zhang, and Yacho Liu, Magnetosubbands of semiconductor quantum wires with Rashba and Dresselhaus spin-orbit coupling, Phys. Rev. B **73**, 155316 (2006).

[86] C. P. Weber, J. Orenstein, B. Andrei Bernevig, Shou-Cheng Zhang, Jason Stephens, and D. D Awschalom, Nondiffusive spin dynamics in a two-dimensional electron gas, Phys. Rev. Lett. **98**, 076604 (2007).

[87] Peter Stano and Jaroslav Fabian, Control of electron spin and orbital resonances in quantum dots through spi-orbit interactions, Phys. Rev. B **77**, 045310 (2008).

[88] Torque, and convectional spin Hall currents in two-dimensional spin-orbit systems: Universal relation and hyperselection, Phys. Rev. B **79**, 125201 (2009).

[89] J. Luo, H. Munekata, F. F. Fang, and P. J. Stiles, Effects of inversion asymmetry on electron energy band structures in $GaSb/InAs/GaSb$ quantum wells, Phys. Rev. B **41**, pp. 7685-7693 (1990).

[90] J.P.Heida, B.J.van Wees, J.J.Kuippers, T.M.Klapwijk, and G.Borghs, Spin-orbit interaction in two-dimensional electron gas in a $InAs/AlSb$ quantum well with gate-controlled electron density, Phys. Rev. B **57**, pp. 11911- 11914 (1998).

[91] T. Matsuyama, R. K*ü*rsten, C. Meißner, and U. Merkt, Rashba spin splitting in inversion layers on $p-$tpye bulk InAs, Phys. Rev. B **61**, pp. 15588-15591 (2000).

[92] Y.Sato, T.Kita, S.Gozu, and S.Yamada, Large spontaneous spin splitting in gate-controlled two-dimensional electron gases at normal $In_{0.75}Ga_{0.25}As/In_{0.75}Al_{0.25}As$ heterojunctions, J. Appl. Phys. **89**, pp. 8017-8021 (2001).

[93] Drik Grundler, Large Rashba splitting in InAs quantum wells due to electron wave function pentetration into the barrier layers, Phys. Rev. Lett. **84**, pp. 6074-6077 (2000).

[94] Antonios gonis and William H. Butler, *Multiple Scattering in Solids*, Springer-Verlag New York, Inc. (2000).

[95] George B. Arfken and Hans J. Weber, *Mathematical Methods for Physicists*, Fifth ed. Harcourt/Academic Press (2001).

[96] J. J Sakurai *Modern Quntum Mechanics*, Rvised Ed. Addison-Wesley Publishing Company, Inc. (1994)

[97] Gerald D. Mahan, *Quantum Mechanics in a Nutshell*, Princeton University Press (2009).

[98] John H. Davies, *The Physics of Low-Dimensional Semiconductor: An Introduction*, Cambridge University Press, New York (1998).

[99] Ampere A. Tseng (Editor), *Tip-Based Nanofabrication Fundamentals and Applications*, Springer Science+Business Media, LLC, New York (2011).

[100] Carlo Jacoboni, *Theory of Electron Transport in Semiconductors: A Pathway from Elementary Physics to Nonequilibrium Green Functions*, Springer-Verlag, Berlin Heidelberg (2010).

[101] R. Völkl, M. Griesbeck, S. A. Tarasenko, D. Schuh, W. Wegscheinder, C. Schüller, and T. Korn, Spin depahsing and photoinduced diffusion in a high- mobility two-dimensional electron system embedded in GaAs-(Al,Ga)As quantum well grown in the (110) direction, Phys. Rev. B **83**, 241306 (2011).

[102] M. B. A. Jalil. , S. G. Tan, and T. Fujita, Spintronics in 2DEG systems, AAPPS Bulletin, Vol. **18**, pp. 9-20 (2008).

[103] Klaus D. Sattler (Editor), *Handbook of Nanophysics: Principles and Methods*, Taylor and Francis Group, LLC (2011).

[104] D. Weller et at., Thermaleffect limits in ultrahigh-density magnetic recording, Magn. IEEE Trans. **35**, pp. 4423-4439 (1999).

[105] Hori, H., Teranishi, T., Nakae, Y. et al., Anomalous magnetic polarization effect of Pd and Au nano-particles, Phys. Lett. A **263**, pp. 406-410 (1999).

[106] Vager, Z., Carmeli, I., Leitus, G., Reich, S., and Naaman, R., Surprising electronic-magnetic properties of closed packed organized organic layers, J. Phys.Chem. Sol. **65**, pp. 713-717 (2004).

[107] Garitaonandia, J. S., Insausti, M., Goikolea, E. et al., Chemically induced permanet magnetism in Au. Ag, and Cu nanoparticles: Localization of magnetism by element selective techniques, Nano. Lett. **8**, pp. 661-667 (2008).

[108] Ito, Y., Miyazaki A., Fukui F., Valiyaveettil S., Yokoyama T., and Enoki, T., Pd nanoparticle embedded with only one Co atom behaves as a single particle magnet, J. Phys. Soc. Jpn. **77** 103701 (2008).

[109] Teng, X. W., Han, W. Q., Ku. W. et al., Synthesis of ultrathin Palladium and Plantium nanowires and study of their magnetic properties, Angew. Chem. Int. Ed. **47**, pp. 2055-2058 (2008).

[110] Madhu, C., Sundaresan, A., and Rao, C. N. R., Room temperature ferromagnetism in undoped GaN and CdS semiconductor nanoparticles, Phys. Rev. B **77**, 201306 (2008).

[111] Carmeli, I., Bloom, F., Gwinn, E., et al., Molecular enhancement of ferromagnetism $GaAs/GaMnAs$ heterostructures, Appl. Phys. Lett. **89**, 112508 (2006).

[112] D. Chiba, M. Yamanouchi, F. Matsukura and H. Ohno, Electrical manupulation of Magnetization reversal in a ferromagnetic semiconductor, Science **301**, pp. 943-945 (2003).

[113] Nazmul, A.M., Sugahara, S. and Tanaka, M., Ferromagnetism and high Curie temperature in semiconductor heterostructures with Mn δ-doped $GaAs$ and p-type selective doping,Phys. Rev. B (Rapid Communications) **67**, 241308 (2003b).

[114] Nazmul, A.M., Amemiya, T., Shuto, Y., et al., High temperature ferromagnetism in $GaAs$-based heterostructures with Mn delta doping,Phys. Rev. Lett. **95**, 017201 (2005).

[115] Yayoi Takamura, Rajesh V. Chopdekar, Andreas Scholl, Andrew Doran, J. Alexander Liddle, Bruce Harteneck, and Yuri Suzuki, Tuning magnetic domain

structure in nanoscle $La_{0.7}Sr_{0.3}MnO_3$ islands, Nano Letters Vol. **6**, pp. 1287-1291 (2006).

[116] Yan Wu, Y. Matsushita, and Y. Suzuki, Nanoscale magnetic-domain structure in colossal magnetoresistance islands, Phys. Rev. B**64**, 220404(R)(2001).

[117] L. Kong, Q. Pan, B. Cui, M. Li, S. Y. Chou, Magnetotranport and domain structures in nanoscale, $NiFe/Cu/Co$ spin valve, J. Appl. Phys. Vol. **85**, pp. 5492-5494 (1999).

[118] Mathias Getzlaff, *Fundamentals of Magnetism* , Springer-Verlag Berlin Heidelberg (2008).

[119] R.P. Cowburn, D.K. Koltsov, A.O. Adeyeye et al., Single-domain circular nanomagnets, Phys. Rev. Lett. **83**, pp. 1042-1045 (1999).

[120] Masato Kotsugi, Chiharu Mitsumata, Hiroshi Maruyama, Takanori Wakita, Toshiyuki Taniuchi, Kanta Ono, Motohiro Suzuki, Naomi Kawamura, Naoki Ishimatsu, Masaharu Oshima, Yoshio Wantanabe, and Masaki Taniguchi, Novel magnetic domain structure in iron meteorite induced by the presence of $L1_0$-$FeNi$, Appl. Phys. Express **3**, 01300 (2010).

[121] M. Viret, D. Vignoles, D. Cole, J. M. D. Coey, W. Allen, D. S. Daniel, and J. F. Gregg, Phys. Rev. B **53**, 8464 (1996).

[122] G. J. Nieuwenhuys, Magnetic behavior of cobalt, iron, and manganese dissolved in palladium, Adv. Phys. Vol.**24**, pp. 515-519 (1975).

[123] Lei Liu, G. Y. Guo, C. S. Jayanthi, and S. Y. Wu, Colossal Paramagnetic moments in metallic carbon nanotori, Phys. Rev. Lett. **88**, 217206 (2002).

[124] S. B. Ogale, R. J. Chouldhary, J. P. Buban, S. E. Lofland, S. R. Shinde, S. N. Kale, V. N. Kulkarni, J. Higgins, C. Lanci, J. R. Simpson, N. D. Browning,

S. Das Sarma, H. D. Drew, R. L. Green, and T. Venkatesan, High temperature ferromagnetism with a giant magnetic moment in transport Co-doped $SnO_{2-\delta}$, Phys. Rev. Lett. **91**, 077205 (2003).

[125] Nguyen Hoa Hong, Joe Sakai, W Prellier, and Awatef Hassini, Transport Cr-doped SnO_2 thin films: ferromagnetism beyoned room temperature with a giant magnetic moment, J. Phys. Condens. Matter **17**, pp. 1697-1702 (2005).

[126] Mukul Kabir, D. G. Kanhere, and Abhijit Mookerjee, Large magnetic moments and anomalous exchange coupling in As-doped Mn clusters, Phys. Rev. B **73**, 075210 (2006).

[127] Jung, Myung-Hawa; Lee, Sung-Ik, Giant magnetic moment of oxygen-free $CuNi$ nanoparticles, Journal of Nanoscience and Nanotechnology, Vol. **9**, pp. 3201-3203 (2009).

[128] Qun Jing, Hai-bin Cao, Gui-Xian Ge, Yuan Xu Wang, Hong-Xia Yan, Zi-Ying Zhang, Yun-Hu Liu, Giant magnetic moment of the core-shell $Co_{13}@Mn_{20}$ clusters: First principles calculation, Journal of Computational Chemistry Vol. **32**, pp. 2474-2478 (2011).

[129] Yoshikazu Ito, Akira Miyazaki, Kazuyuki Takai, Vajiravelu Sivamurugan, Takashi Maeno, Takeshi Kadono, Masaaki Kitano, Yoshihiro Ogawa, Naotake Nakamura, Michikazu Hara, Suresh Valiyaveetti, and Toshiaki Enoki, Magnetic sponge prepared with an alkanedithiol-bridged network of nanomagnets, J. Am. Chem. Soc. **133**, pp. 11470-11473 (2011).

[130] Jun Wang, Pieder Beeli, Yang Ren, and Guo-meng Zhao, Giant magnetic moment enhancement of nickel nanoparticles embedded in multiwalled carbon nanotubes, Phys. Rev. B **82**, 193410 (2010).

[131] Siva Yellampalli (Editor), *Carbon Nanotubes-Polymer Nanocomposites*, InTech, (2011).

[132] Wolf Gang; *Mathematica*; Third edition, Pergamon Press (1977).

[133] John R. Taylor; *Scattering Theory: The Quantum Theory of Nonrelativistic Collisions*; Dover Publications, Inc. Mineola, New York (2000).

[134] Sebastian Loth, Kirsten von Bergmann, Markus Ternes, Alexander F. Otte, Christopher P. Lutz and Andreas J. Heinrich, Nature phys. Lett. **6** pp. 340-344 (2010).

[135] Frank Stern and W. E. Howard, Phys. Rev. **163**, pp. 816-835 (1967).

[136] J. A. Reyes and M. del Castillo-Mussot, Phys. Rev. B **56**, pp. 14893-14896 (1997).

[137] M. E. Portnoi and I. Galbraith, Solid State communications, **103**, pp. 325-329, (1997).

[138] N. Ben Brahim Aounain et al., Solid State communications, **108**, pp. 199-204, (1998).

[139] David K. Ferry, Stephen M. Goodnick, *Transport in Nanostructures*, Cambrige University Press, second edition (1997).

[140] Paul M. Fishbane, Stephen G. Gasiorowicz and Stephen T. Thornton, *Physics for Scientists and Engineers with modern physics*, Pearson Printice Hall, third edition, 2005.

[141] Max Born and Emil Wolf, *Principles of optics,* Cambridge University Press,seventh (expanded) edition, 1999.

DECLARATION

I hereby declare that this thesis is my original work and has not been presented for a degree in any other University. All sources of material used for the thesis have been duly acknowledged.

Teshome Senbeta _____

email: teshearada@yahoo.com

This thesis has been submitted for examination with my approval as University advisor.

Prof. V. N. Mal'nev _____

Addis Ababa Univers